UNIVERSITY OF ROCHESTER
LABORATORY FOR LASER ENERGETICS

Volume 90
January—March 2002
DOE/SF/19460-437

LLE Review

Quarterly Report

About the Cover:

The highlight of this issue is an article about the first cryogenic implosions of D_2-filled targets on the 60-beam OMEGA laser. This is a major milestone in the program that will eventually lead to direct-drive, high-gain implosions on the National Ignition Facility. A tremendous amount of preparatory work must be done to carry out these experiments. The targets must be filled with D_2 gas in the Fill/Transfer Station (FTS), slowly cooled to below 18.72 K, and then gently heated with an IR laser. This produces a uniform layer of D_2 ice on the inner surface of the capsule. The FTS is not connected to the OMEGA target chamber, so the target must be transported to the chamber in a 2300-kg moving cryostat transfer cart (MCTC) supported on air bearings. The upper left photo shows Senior Technical Associates Karl Lintz and Sal Scarantino beginning the transfer process by undocking the MCTC from the FTS. In the upper right photo, they carefully maneuver the MCTC through the hallway. In the experimental area (lower left photo), under the target chamber, the level of auxiliary support is evident. Umbilical cables and hoses supply electricity and compressed air to the cryostat while Technical Associates Dale Guy and James Sailer monitor the status of the instruments that keep the temperature of the target within 0.5 mK° of the triple point of D_2. Once the MCTC is positioned under the target chamber, a vacuum-to-vacuum connection must be established (lower right photo). Then the target can be lifted into the target chamber and imploded by the 60-beam OMEGA laser (center photo).

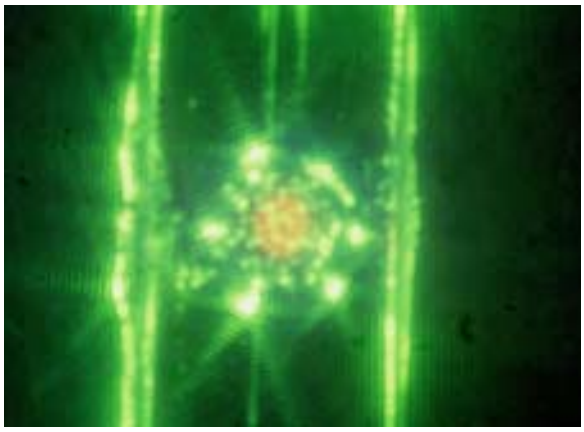

The central image on the cover is a visible light image of the imploding target on shot 27452 taken with the Kowaluk camera (see LLE Review Volume 89). The 60 bright white spots are the UV beams of OMEGA. The orange ball in the center is reflected UV light, downshifted in frequency by the expanding laser-generated plasma from the target. The intense lines on either side of the target are the berylium stalks used to stiffen the target support. The spider webs that hold the target in place show up as the fainter lines (above and below the target) glowing in the incident laser light.

This report was prepared as an account of work conducted by the Laboratory for Laser Energetics and sponsored by New York State Energy Research and Development Authority, the University of Rochester, the U.S. Department of Energy, and other agencies. Neither the above named sponsors, nor any of their employees, makes any warranty, expressed or implied, or assumes any legal liability or responsibility for the accuracy, completeness, or usefulness of any information, apparatus, product, or process disclosed, or represents that its use would not infringe privately owned rights. Reference herein to any specific commercial product, process, or service by trade name, mark, manufacturer, or otherwise, does not necessarily constitute or imply its endorsement, recommendation, or favoring by the United States Government or any agency thereof or any other sponsor. Results reported in the LLE Review should not be taken as necessarily final results as they represent active research. The views and opinions of authors expressed herein do not necessarily state or reflect those of any of the above sponsoring entities.

The work described in this volume includes current research at the Laboratory for Laser Energetics, which is supported by New York State Energy Research and Development Authority, the University of Rochester, the U.S. Department of Energy Office of Inertial Confinement Fusion under Cooperative Agreement No. DE-FC03-92SF19460, and other agencies.

Printed in the United States of America
Available from
National Technical Information Services
U.S. Department of Commerce
5285 Port Royal Road
Springfield, VA 22161

Price codes: Printed Copy A03
Microfiche A01

For questions or comments, contact William R. Donaldson, *Editor*, Laboratory for Laser Energetics, 250 East River Road, Rochester, NY 14623-1299, (716) 275-5347.

Worldwide-Web Home Page: http://www.lle.rochester.edu/

UNIVERSITY OF ROCHESTER
LABORATORY FOR LASER ENERGETICS

Volume 90
January–March 2002
DOE/SF/19460-437

LLE Review

Quarterly Report

UR LLE

Contents

In Brief iii

First Results from Cryogenic Target Implosions on OMEGA 49

Equation-of-State Measurements of Porous Materials on OMEGA: Numerical Modeling 57

Observations of Modulated Shock Waves in Solid Targets Driven by Spatially Modulated Laser Beams 68

Time-Dependent Electron Thermal Flux Inhibition in Direct-Drive Laser Implosions 73

Precision Spectral Sculpting of Broadband FM Pulses Amplified in a Narrowband Medium 79

Electric-Field-Induced Motion of Polymer Cholesteric Liquid Crystal Flakes in a Moderately Conductive Fluid 83

Femtosecond Response of a Freestanding LT-GaAs Photoconductive Switch 88

Publications and Conference Presentations

In Brief

This volume of the LLE Review, covering January–March 2002, features "First Results from Cryogenic Target Implosions on OMEGA" by C. Stoeckl *et al*. (p. 49). This article describes initial results from direct-drive spherical cryogenic target implosions on the 60-beam OMEGA laser system. These experiments are part of the scientific base leading to direct-drive ignition implosions planned for the National Ignition Facility (NIF). Results shown include neutron yield, secondary-neutron and proton yields, the time of peak neutron emission, and both time-integrated and time-resolved x-ray images of the imploding core. The experimental values are compared with 1-D numerical simulations. The target with an ice-layer nonuniformity of $\sigma_{rms} = 9\ \mu$m showed 30% of the 1-D predicted neutron yield. These initial results are encouraging for future cryogenic implosions on OMEGA and the NIF.

Additional highlights of research presented in this issue include the following:

- T. J. B. Collins and T. R. Boehly (p. 57) present a theory that models equation-of-state measurements of porous materials. Experiments have been performed on OMEGA as part of the Stockpile Stewardship Program to investigate the equation of state of carbonized resorcinol foam, a porous material. Using the impedance-matching method, the foam Hugoniot was calculated from the well-known equation of state of aluminum and from measured shock speeds over the range of 100 kbar to 2 Mbar.

- A second article by T. R. Boehly and T. J. B. Collins (p. 68) describes the perturbation of a target by nonuniformities in the drive laser. Drive lasers, with known, single-mode modulations, produce nonuniform shocks that propagate into CH targets. An optical probe beam is used to measure the arrival of these modulated shocks at various surfaces in the target. Experiments at moderate laser intensities ($\lesssim 10^{13}$ W/cm^2) exhibit behavior that is predicted by hydrocodes and simple scaling laws. This technique may be used to observe various dynamic effects in laser-produced plasmas and shock-wave propagation.

- A. Sunahara, J. A. Delettrez, C. Stoeckl, R. W. Short, and S. Skupsky (p. 73) describe the time dependence of electron thermal flux inhibition in direct-drive laser implosions. They calculate the nonlocal electron thermal conduction in direct-drive CH target implosions with square pulses by a one-dimensional Fokker–Planck solver combined with a hydrodynamic code. The results show that the electron thermal flux inhibition at the critical surface is time dependent, confirming that a larger flux limiter must be used for shorter-duration pulses. Also, the growth of the Rayleigh–Taylor instability for short-wavelength perturbations is shown to be smaller due to the longer density scale length.

- L. J. Waxer and J. H. Kelly (p. 79) have demonstrated precision spectral sculpting of broadband FM pulses amplified in a narrowband medium. Amplification of broadband frequency-modulated (FM) pulses in high-efficiency materials such as Yb^{+3}:SFAP results in significant gain narrowing, leading to reduced on-target bandwidths for beam smoothing and to FM-to-AM conversion. These effects were compensated for by applying precision spectral sculpting, with both amplitude and phase shaping, before amplifying the broadband FM pulses in narrowband gain media. The spectral sculpting, for center-line small-signal gains of 10^4, produced amplified pulses that have both sufficient bandwidths for on-target beam smoothing and temporal profiles that have no potentially damaging amplitude modulation.

- T. Z. Kosc, K. L. Marshall, S. D. Jacobs, J. C. Lambropoulos, and S. Faris (p. 83) describe electric-field-induced motion of polymer cholesteric liquid crystal flakes in a conductive fluid. Polymer cholesteric liquid crystal flakes suspended in a fluid with non-negligible conductivity can exhibit motion in the presence of an ac electric field. The platelets have a strong selective reflection, which is diminished or extinguished as the flakes move. Flake motion was seen within a specific frequency bandwidth in an electric field as low as 5 mV_{rms}/mm.

- X. Zheng, Y. Xu, R. Sobolewski, R. Adam, M. Mikulics, M. Siegel, and P. Kordos (p. 88) discuss the femtosecond response of a freestanding LT-GaAs photoconductive switch. A novel, freestanding LT-GaAs photoconductive switch has a femtosecond response time. The switch was formed by patterning a 1-mm-thick layer of a single-crystal LT-GaAs into a 5-μm by 15-μm bar The bar was separated from its GaAs substrate and placed across a gold coplanar transmission line deposited on a Si wafer. The switch was excited with 110-fs-wide optical pulses, and its photoresponse was measured with an electro-optic sampling system. Using 810-nm optical radiation, 470-fs-wide electrical transients (640-GHz bandwidth) were recorded.

William R. Donaldson
Editor

First Results from Cryogenic Target Implosions on OMEGA

Introduction

The base-line direct-drive ignition target design for the National Ignition Facility (NIF)[1] is a thick cryogenic DT-ice layer enclosed in a thin CH shell.[2,3] In direct-drive inertial confinement fusion (ICF)[4] a spherical target is illuminated by a large number of laser beams to provide a spherically symmetric implosion. Target implosions with cryogenic DT fuel are planned using the 60-beam OMEGA laser system[5] to validate the theoretically determined[3] levels of laser and target uniformity required to achieve direct-drive ignition and gain on the NIF. The OMEGA cryogenic target designs are energy scaled from the NIF ignition designs.[2,3] In particular, the OMEGA cryogenic targets, driven by an energy-scaled ignition pulse, are designed to be as "hydrodynamically equivalent" as possible to the ignition capsule designs. In this context, the constraints placed on the OMEGA cryogenic target designs include peak shell velocities, hot-spot convergence, in-flight aspect ratio, and stability properties similar to those of the NIF designs. To compare igniting and non-igniting target designs, we use the hot-spot convergence ratio, defined as the ratio of the radius containing 90% of the yield when propagating burn was deactivated compared to the initial ice–gas interface. In addition, the principle sources of nonuniformity on OMEGA, which lead to a degradation in target performance, are similar to the NIF. For direct-drive ICF these sources are single-beam nonuniformity ("laser imprint"), drive asymmetry, inner ice surface, and outer-surface roughness.

Ignition with direct-drive ICF relies on the generation of a "spark" in the compressed "hot spot" to begin the nuclear burn.[6] The hot spot is a high-temperature, low-density region surrounded by a low-temperature, high-density region into which the burn wave propagates, leading to significant energy gain. Target and laser illumination nonuniformities lead to distortions in the hot spot due to secular (linear in time) growth of low-order ($\ell \leq 10$) modes, shell breakup, and mix due to the Rayleigh–Taylor (RT)[7,8] growth of high-order ($\ell > 10$) nonuniformities. Previous cryogenic target experiments[9–13] have used ice layers that were formed only by β-layering, but not thoroughly and carefully characterized. The targets generally performed poorly (the reported neutron yields did not exceed 0.2% of the 1-D predictions[10]), and the results could not be used to validate detailed multidimensional numerical simulations because of the missing information on the inner-ice-surface nonuniformity spectrum.

This article describes first experiments with layered and characterized cryogenic targets on OMEGA. These experiments have validated the technology to fill, layer, characterize, and shoot cryogenic targets. The following sections present the OMEGA cryogenic target designs, describe the results of the characterization of the inner-ice-surface quality of the cryogenic targets, review the results from the first cryogenic D_2 campaign on OMEGA, give an outlook on future improvements, and present conclusions.

OMEGA Cryogenic Target Designs

The basis for the OMEGA cryogenic designs is the NIF direct-drive, $\alpha = 3$ ignition design, which consists of a 340-μm-thick DT-ice layer encased in a thin (3-μm) plastic capsule of 1.69-mm outer radius.[3] The laser pulse required for the ignition design is a 9.25-ns shaped pulse consisting of a 10-TW, 4.25-ns foot rising to a 450-TW peak drive for 2.5 ns. Although higher one-dimensional gains can be achieved for lower-adiabat implosions, the highest multidimensional gains for NIF energy and uniformity levels are predicted to be achieved for implosions driven on an adiabat between 3 and 4. One-dimensional hydrodynamic scaling arguments[14] have been used to design the cryogenic targets for OMEGA. It has been shown[14,15] that the energy, time, and laser power scalings are

$$\left(E \sim R^3,\ t \sim R, \text{ and } P \sim R^2\right).$$

The NIF is designed to provide 1.5 MJ of energy with the $\alpha = 3$ pulse shape, while OMEGA is capable of delivering 30 kJ. Thus, the radius of an OMEGA capsule should be approximately 0.3 times the NIF design, i.e., 0.46 mm, with a 100-μm DT-ice layer inside a 1-μm-thick plastic shell. The equivalent OMEGA $\alpha = 3$ pulse consists of a 0.75-TW foot

rising to a 33-TW peak with an overall pulse length of 2.5 ns. Figure 90.1 shows a comparison between the NIF and OMEGA targets and pulse shapes. One-dimensional hydrocode calculations predict a gain of 45 (neutron yield $Y_n = 2.5 \times 10^{19}$), a hot-spot convergence ratio of 28, and a peak fuel areal density ρR_{peak} = 1300 mg/cm^2 for the NIF ignition design. A neutron yield of $Y_n = 1.8 \times 10^{14}$, a hot-spot convergence ratio of 20, and a peak fuel areal density $\rho R_{peak} = 300$ mg/cm^2 are predicted for the scaled OMEGA cryogenic DT design.[3] The "classical" definition of convergence ratio (the ratio of the minimum to the initial fuel–shell radius) is inappropriate for cryogenic targets since the inner ice layer forms part of the hot spot; therefore we use the hot-spot convergence ratio as defined in the introduction. A detailed analysis[15] shows that the energy-scaled targets exhibit similar 1-D behavior of the shock timing and fuel adiabat as the ignition designs. The shorter density scale length of the OMEGA target leads to a lower laser energy absorption of 40% compared to 60% for the ignition design. Consequently the energy-scaled target has a slightly higher adiabat and a lower hot-spot convergence ratio of 20 compared to 28 in the ignition design.

The RT instability can degrade target performance by breaking the spherical symmetry of the implosion. The RT instability occurs twice during the implosion: at the outer ablation surface as the shell accelerates inward and at the hot spot/main fuel layer interface as the capsule decelerates at the end of the implosion. The RT instability is seeded by single-beam laser nonuniformity, drive asymmetry, feedout from the inner ice surface, and outer-surface roughness. Detailed 2-D *ORCHID* simulations[3] have established the maximum levels of these nonuniformity sources to achieve ignition and gain on the NIF.

The analysis of these results shows that, for an outer-surface roughness of <115 nm and an inner-ice-surface roughness of ≤1 μm rms, individual beam smoothing by two-color-cycle, 1-THz, 2-D SSD with polarization smoothing (PS), and an on-target power imbalance of <2% rms, a gain of 30 is predicted for the NIF (70% of 1-D). The OMEGA design has been shown[3,15] to be more sensitive to the nonuniformity seeds than the NIF. This is attributed to the smaller hot spot in the OMEGA design, which can be more easily disrupted by the penetration of the cold spikes from the main fuel layer. For the same uniformity conditions as described for the NIF, the OMEGA-scaled $\alpha = 3$ design is predicted to give 30% of 1-D yield.[15]

Target Layering and Characterization

To create a 100-μm ice layer, the ~3-μm-thick, high-strength CH shells were filled with ~1000 atm of D_2 in a permeation cell inside the Fill/Transfer Station (FTS).[16] The process of filling these capsules takes ~24 h because the gas pressure can be incremented only in very small steps (0.7 atm/min) to avoid buckling of the thin shell due to the pressure gradient between higher pressure outside and lower pressure inside the targets. The targets are cooled very slowly (~0.1 K/min) to below the triple point of D_2 (18.72 K) to avoid bursting from the higher

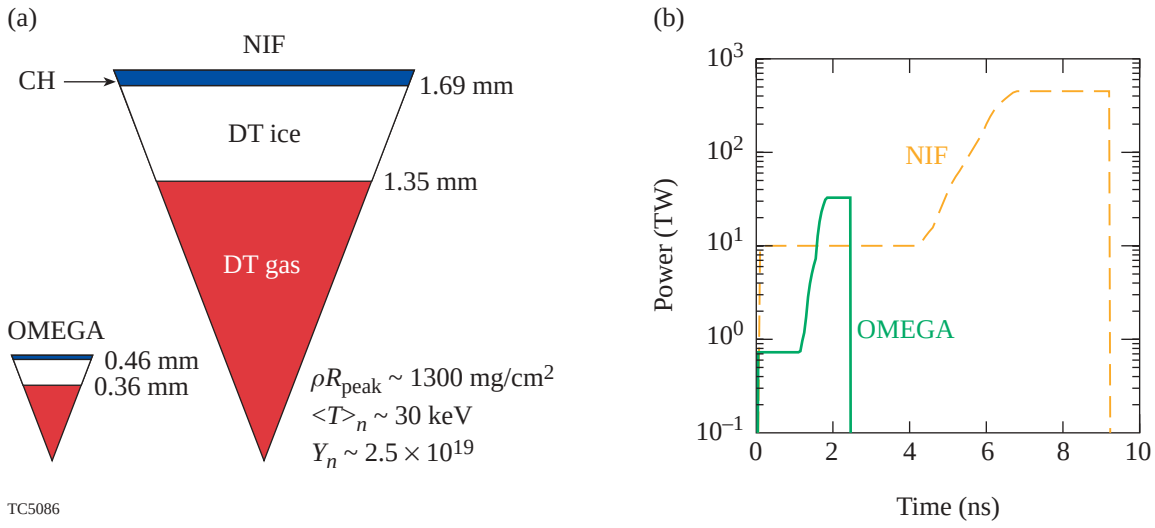

Figure 90.1
The NIF and OMEGA capsule designs (a) and pulse shapes (b). The radius of the OMEGA design is approximately 0.3 times that for the NIF. The pulse duration shrinks from 9.25 ns with a peak power of 450 TW to 2.5 ns with 32-TW peak power.

pressure of the warmer gas inside the targets. After transferring the targets from the FTS to the moving cryostat transfer cart (MCTC), the target assembly is inserted into the characterization station, where the targets are viewed using a high-magnification, high-fidelity optical system during the layering process. The layer is formed and maintained using an IR laser at 3.16-μm wavelength, which is preferentially absorbed in the D_2 ice. This creates a temperature gradient between the cooled layering sphere, which surrounds the target, and the gas/ice interface inside the target. Thicker parts of the ice layer are heated preferentially, increasing the sublimation rate in the hotter parts, while the gas preferentially refreezes at the colder parts of the ice layer. This results in a net layering effect that leads to an equal ice-layer thickness over the entire sphere. This IR layering scheme uses more than one order of magnitude more heating power than β-layering of DT-filled cryogenic targets can provide, which suggests that active layering might be necessary even for DT targets.

The inner-ice-surface nonuniformities are characterized using a shadowgraphic technique as shown in Fig 90.2. The parallel rays from a light source are refracted at the plastic shell and reflected by total internal reflection from the inner ice surface, thus forming a virtual bright ring. The bright ring in the recorded image is unrolled using the center of the shadow of the plastic shell as a reference point, providing a graph with the distance of the inner ice surface from the center of the shell as a function of angle. The difference in the measured distance of

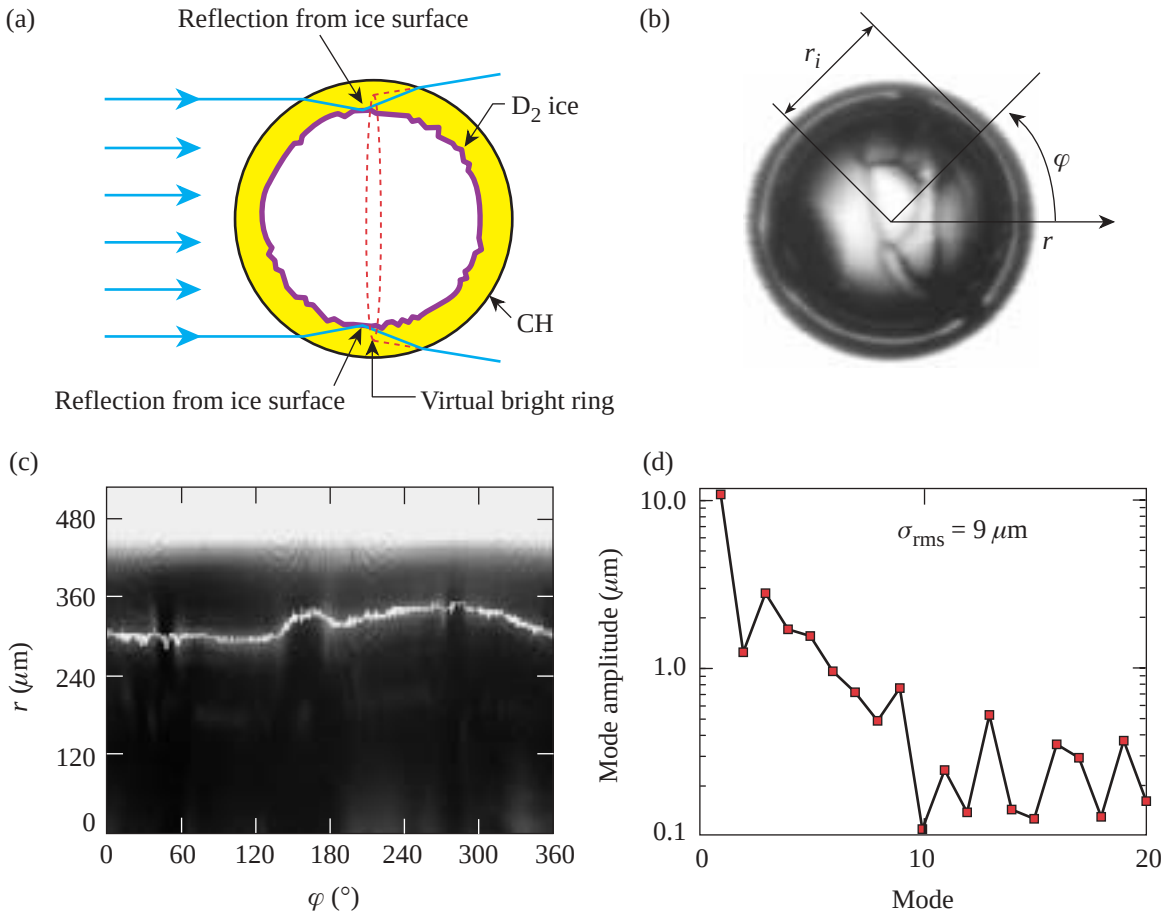

Figure 90.2
Shadowgraphic layer characterization: (a) The target is illuminated by collimated white light. (b) Internal total reflection at the ice/gas surface produces a virtual bright ring in the image. (c) The image is unrolled around its center, mapping the distance of the ice/gas interface as a function of angle around the target. (d) The difference of the measured distance from a perfect circle is decomposed into cosine mode amplitudes.

the ice surface from a perfect circle is then decomposed into cosine modes, resulting in a nonuniformity spectrum of the inner ice surface. These measurements provide only a 2-D representation of the inner-ice-surface nonuniformity along one circular cut through the sphere. Several such measurements, along different lines of sight, can be performed to fully map the 3-D nonuniformity spectrum.

Cryogenic Target Implosions

The cryogenic targets used in these first experiments were ~930-μm-diam, ~3-μm-thick shells of high-strength CH with 100-μm-thick D_2-ice layers. The targets were characterized along one line of sight and showed an inner-ice-surface roughness of $\sigma_{rms} \geq 9\ \mu$m, with the most power (~90%) in the three lowest modes. A 1-ns square pulse at ~24-kJ laser energy was used with the best single-beam smoothing available [distributed phase plates (DPP);[17] polarization smoothing (PS) with birefringent wedges;[18] 2-D, single-color-cycle, 1-THz smoothing by spectral dispersion (SSD)[19]] and optimized energy balance (<3% beam to beam).[20] The calculated time-dependent, on-target overlapped nonuniformity ($\ell = 1 \sim 500$) due to single-beam nonuniformity, assuming perfect beam-to-beam power balance for 1-THz SSD with PS, is less than 1% after 300 ps.[21] When beam overlap on target is included, the on-target nonuniformity due to beam-to-beam energy imbalance is less than 1% ($\ell \leq 12$). This level of single-beam laser nonuniformity and drive asymmetry is close to that specified above; however, the current levels of inner-ice-surface roughness ($\sigma_{rms} \geq 9\ \mu$m) significantly exceed the design goal ($\sigma_{rms} \leq 1\ \mu$m). A 1-ns square pulse was used to make the implosion less sensitive to instability growth than the $\alpha = 3$ design in Fig. 90.1. This pulse puts the target on an $\alpha = 25$ adiabat and leads to a predicted hot-spot convergence ratio of approximately 10. One-dimensional *LILAC*[22] simulations predict a neutron-averaged areal density of ~40 mg/cm^2, an ion temperature of approximately 2 keV, and a neutron yield of 1.0×10^{11}. Five target shots were successfully performed in a two-week experimental campaign. All targets showed good neutron-yield performance (up to 3.5×10^{10}), ranging from 4% to 30% of the clean yield, denoted as yield over clean (YOC), predicted by 1-D *LILAC* hydrodynamic simulations.

Table 90.I summarizes the performance measured by neutron and particle diagnostics of two target shots, 24089 and 24096, having ice-layer nonuniformities of $\sigma_{rms} = 19\ \mu$m and $\sigma_{rms} = 9\ \mu$m, respectively. The performance is compared with 1-D clean calculations. Secondary in-flight fusion reactions of the tritium (T) and helium (He^3) ions produced in the D_2 fusion reaction can be used to infer fuel areal densities.[23–26] The areal density of the hot neutron-producing core $\langle\rho R\rangle_{hot}$ ($T_i \geq 0.5$ keV) is inferred using the ratio of the secondary proton to the primary neutron, Y_{2n}/Y_n, from the in-flight fusion of He^3 (Ref. 27). Due to the very short range of He^3 in the colder fuel (<1 mg/cm^2 at $T_e < 0.5$ keV),[28] the secondary proton production is confined to the hot parts of the core, if the electron and ion temperatures are assumed to be equal. This measurement saturates at about 10 mg/cm^2 for a plasma electron temperature close to 3 keV, which is consistent with the measured neutron-averaged ion temperatures $\langle T_{ion}\rangle_n$. The inferred values of $\langle\rho R\rangle_{hot} = 5$ mg/cm^2 and $\langle\rho R\rangle_{hot} = 7$ mg/cm^2 for target shots

Table 90.I: Target performance measured by neutron and particle diagnostics and compared to 1-D clean calculations for the two best-performing target shots: 24089 and 24096.

	1-D	24089	24096
Roughness (μm)		19	9
Neutron yield	1.0×10^{11}	$(1.26\pm0.1) \times 10^{10}$	$(3.05\pm0.1) \times 10^{10}$
Yield compared to 1-D		16%	30%
$\langle T_{ion}\rangle_n$ (keV)	2.1	2.9±0.5	3.5±0.5
Bang time (ns)	1.8	1.8±0.1	1.7±0.1
Y_{2n}/Y_n	9.0×10^{-3}	$(8.0\pm0.4) \times 10^{-3}$	$(9.0\pm0.5) \times 10^{-3}$
Y_{2p}/Y_n	1.2×10^{-3}	$(0.6\pm0.1) \times 10^{-3}$	$(0.8\pm0.1) \times 10^{-3}$
$\langle\rho R\rangle_{hot}$ (mg/cm^2)	14	5±1	7±1
$\langle\rho R\rangle_{total}$ (mg/cm^2)	40	20–30–58	12–25–38

24089 and 24096, respectively, are well below the saturation level. The predicted areal density of the hot neutron-producing core $<\rho R>_{\text{hot}}$ ($T_i \geq 0.5$ keV) at peak neutron production in the 1-D clean calculations is 14 mg/cm^2. The total areal density $<\rho R>_{\text{total}}$ is measured using the downshift of the secondary proton spectrum.[27] A relatively large spread is seen in the data, recorded by five proton detectors located in different ports around the target. Table 90.I shows the minimum, average, and maximum values inferred. The predicted 1-D $<\rho R>_{\text{total}}$ is given by the neutron-averaged areal density. The measured average total areal densities are more than 60% of the 1-D clean predictions. The ratio of the secondary neutron to the primary neutron, Y_{2n}/Y_n, can also be used to infer the total areal density.[25,27] However, secondary neutron ratios are also sensitive to the temperature profile through the slowing down of the primary triton of the D_2 fusion reaction and the energy-dependent cross section of the reaction. In these experiments it is most probably saturated, given the relatively high $<\rho R>_{\text{total}}$ as inferred from the downshift of the secondary proton spectrum. In addition, secondary neutron ratios close to 1×10^{-2} are seen in this model only if all the fuel has a temperature higher than 1 keV,[25,28] which is a highly unlikely scenario in these experiments. The measured and predicted bang times are very close, indicating that the laser absorption and hydrodynamic response of the cryogenic targets are accurately modeled in the 1-D clean calculations. The experimental data show that the YOC and $<\rho R>_{\text{hot}}$ are most sensitive to the inner-ice-surface nonuniformities and improve significantly as the nonuniformity decreases. The neutron-averaged ion temperature and the bang time exhibit little sensitivity to the ice nonuniformity. Figure 90.3 shows static x-ray pinhole camera (XRPC) images and snapshots taken by an x-ray framing camera (XRFC) with an exposure time of 40 ps at peak compression compared with shadowgraphic images taken before the target shot. The XRPC images display the entire implosion from the thin plastic shell lighting up on the outside of the target at the beginning of the pulse to the formation of a core in the center of the image. A comparison of the two experiments clearly shows that shot 24096 starts with lower inner-ice-surface nonuniformities that carry over into a more integral and symmetric core. Neutron data confirm this behavior with shot 24096 achieving 30% YOC while shot 24089 had 16% YOC. This should be compared to noncryogenic implosion experiments on OMEGA that have achieved YOC of ~30% for targets with acceleration-phase-stability properties similar to the future $\alpha = 3$ cryogenic implosions described earlier.[20]

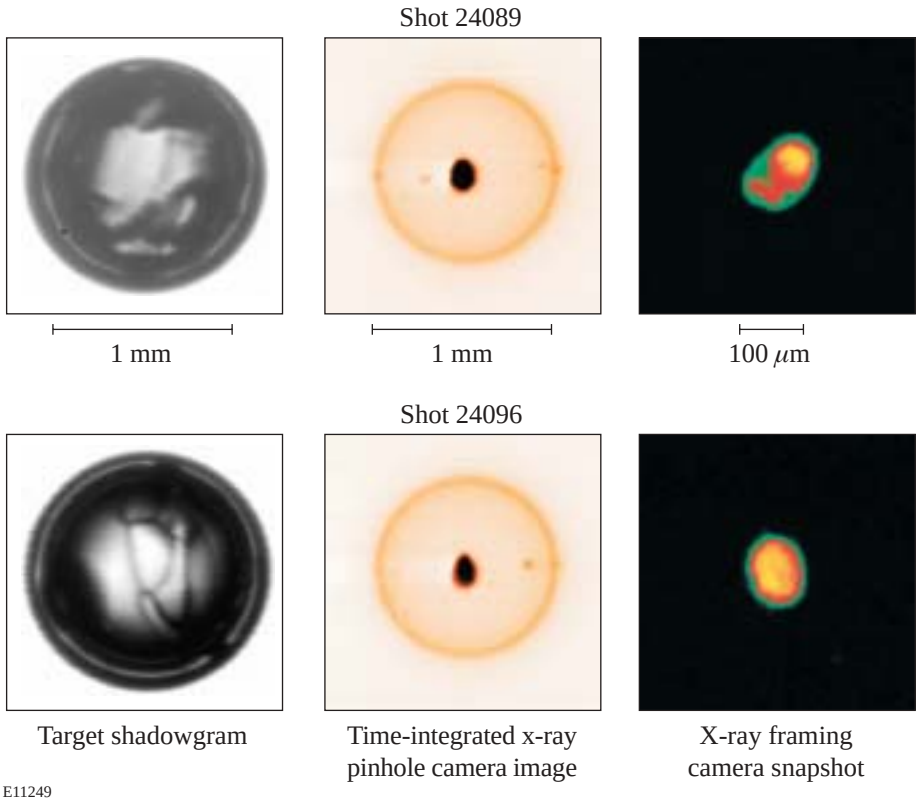

Figure 90.3
Shadowgraphic images of the targets for shots 24089 and 24096 shown in comparison with static x-ray pinhole camera (XRPC) images and x-ray framing camera (XRFC) snapshots. The XRPC images show the lighting up of the thin plastic shell on the outside of the target and the formation of a core in the center of the image. The XRFC images are recorded at peak compression with an exposure time of 40 ps. A clear correlation of the layer quality in the shadowgraphic images and the core quality in the XRPC and XRFC images can be seen.

Both the nuclear and x-ray data indicate that at the present level of inner-ice-surface nonuniformity, the target performance as measured by the YOC, the areal density of the hot neutron-producing core, and the integrity and symmetry of the x-ray core image are strongly affected by the quality of the inner ice layer. The other nonuniformity sources including laser imprint and drive asymmetry, which did not vary significantly during the experimental campaign, appear to be less important in these experiments.

Near-Term Developments

Recent layering studies have produced a much better layer quality (σ_{rms} = 3 μm), with most of the amplitude in the two lowest-order modes. Figure 90.4 shows a shadowgraphic image of such a layer, together with the mode-amplitude spectrum. If the two lowest-order modes of the inner-ice-surface nonuniformity are caused by nonuniformities in the temperature profile inside the layering sphere, they are relatively easy to improve by minor changes in the layout of the layering geometry.[29] Other sources of ice-surface nonuniformity, like enhanced thermal resistivity at the plastic/ice interface, are under active investigation. Future experiments will use lower-adiabat pulse shapes like the ramp-to-flat pulse shown in Fig. 90.5 together with targets with recently improved ice layers, to achieve higher areal densities. When the layer quality reaches the design goal of $\sigma_{rms} \le 1$ μm, low-adiabat pulses like the α = 3 pulse will be used to obtain peak areal densities of more than 200 mg/cm^2 using D_2-ice layers. Table 90.II summarizes the calculated clean 1-D performance and adiabat for the three different pulse shapes. Future cryogenic experiments using DT-ice layers, which are more massive than pure-D_2 layers, should extend the accessible parameter space to peak areal densities of ~300 mg/cm^2.

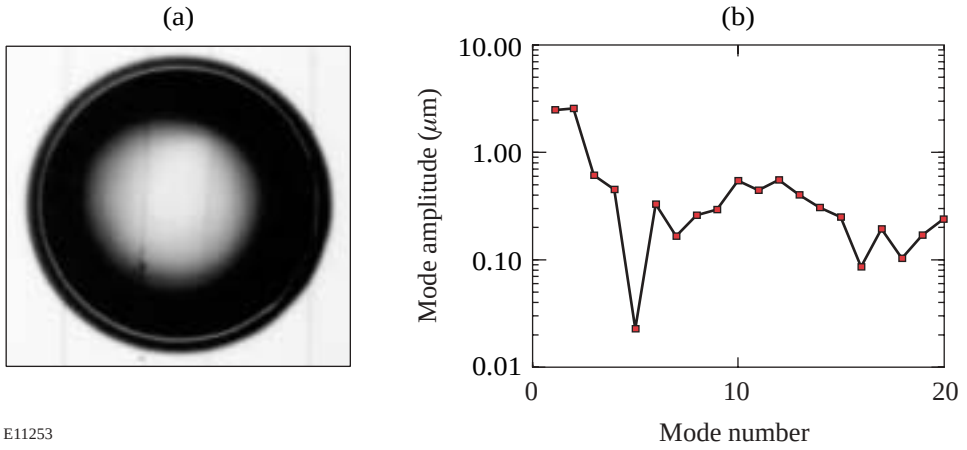

Figure 90.4
Shadowgraphic image (a) of a cryogenic target shown together with the mode-amplitude spectrum (b) of the inner-ice-surface nonuniformities and demonstrating as low as 3-μm rms ice roughness.

Table 90.II: Calculated clean 1-D performance of D_2 cryogenic target for three pulse shapes with different predicted fuel adiabats. The hot-spot convergence ratio is defined as the ratio of the radius containing 90% of the yield compared to the initial ice interface when propagating burn was deactivated.

Pulse	Adiabat	Energy (kJ)	$<\rho R>_{peak}$ (mg/cm^2)	D_2 yield	Hot-spot CR
1-ns square	27	24	43	1.0×10^{11}	10
Ramp to flat	17	18	63	1.2×10^{11}	11
α = 3	3	30	212	8.8×10^{11}	20

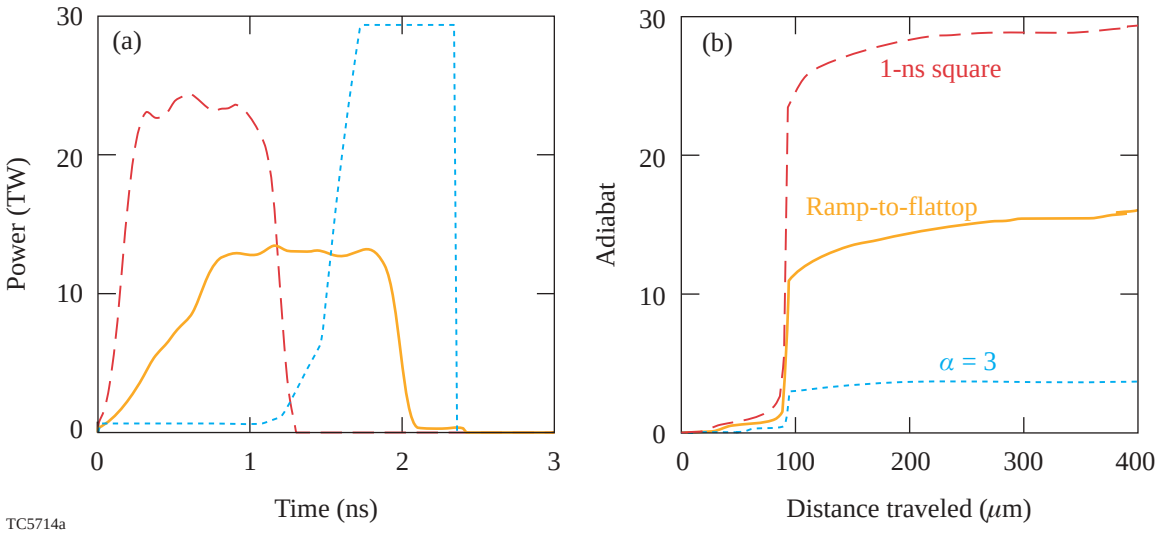

Figure 90.5
Laser power history (a) for three different OMEGA pulse shapes and (b) the corresponding fuel-adiabat trajectories.

Conclusion

The first experiments with the recently commissioned OMEGA Cryogenic Target Handling System have been described. The cryogenic target design is energy scaled from the direct-drive ignition designs for the NIF. The major goal of these experiments is to study the various sources of nonuniformity and their influence on target performance. Similar one-dimensional behavior and stability properties of the OMEGA and NIF cryogenic target designs will facilitate the extrapolation of the cryogenic target studies on OMEGA to NIF targets. In particular, NIF direct-drive ignition targets will be less sensitive to instability growth because the hot spot in the NIF design is bigger than in the OMEGA cryogenic targets. The first cryogenic targets, using 1-ns square pulses, achieved 30% of 1-D yield and more than 60% of the predicted neutron-averaged areal density with an inner-ice-surface nonuniformity of $\sigma_{rms} = 9\,\mu$m. At the present level of inner-ice-surface nonuniformity, the target performance is strongly affected by the quality of the inner ice layer. Recent improvements in the layering technique make it possible to produce much better ice layers, $\sigma_{rms} = 3\,\mu$m, with the prospect of achieving the design goal of 1 μm in the near future. Targets with improved inner-ice-surface quality will be used with lower-adiabat pulses to substantially increase the fuel areal density. In summary, these very encouraging initial results are a major step on the path leading to high-density compressed cores in direct-drive target implosions on OMEGA and to direct-drive ignition on the National Ignition Facility.

ACKNOWLEDGMENT

The authors are grateful to the staff of the Laboratory for Laser Energetics for their dedicated efforts in developing and providing the high-performance OMEGA laser system, and the tremendous amount of work done in the area of target fabrication to provide as many high-quality cryogenic targets as possible. This work was supported by the U.S. Department of Energy Office of Inertial Confinement Fusion under Cooperative Agreement No. DE-FC03-92SF19460, the University of Rochester, and the New York State Energy Research and Development Authority. The support of DOE does not constitute an endorsement by DOE of the views expressed in this article.

REFERENCES

1. J. A. Paisner, E. M. Campbell, and W. J. Hogan, Lawrence Livermore National Laboratory, Livermore, CA, UCRL-JC-117397 (1994).
2. C. P. Verdon, Bull. Am. Phys. Soc. **38**, 2010 (1993).
3. P. W. McKenty, V. N. Goncharov, R. P. J. Town, S. Skupsky, R. Betti, and R. L. McCrory, Phys. Plasmas **8**, 2315 (2001).
4. J. Nuckolls *et al.*, Nature **239**, 139 (1972).
5. T. R. Boehly, D. L. Brown, R. S. Craxton, R. L. Keck, J. P. Knauer, J. H. Kelly, T. J. Kessler, S. A. Kumpan, S. J. Loucks, S. A. Letzring, F. J. Marshall, R. L. McCrory, S. F. B. Morse, W. Seka, J. M. Soures, and C. P. Verdon, Opt. Commun. **133**, 495 (1997).
6. J. D. Lindl, *Inertial Confinement Fusion: The Quest for Ignition and Energy Gain Using Indirect Drive* (Springer-Verlag, New York, 1998), Chap. 6, pp. 61–82.
7. Lord Rayleigh, Proc. London Math Soc. **XIV**, 170 (1883).

8. G. Taylor, Proc. R. Soc. London Ser. A **201**, 192 (1950).

9. T. M. Henderson and R. R. Johnson, Appl. Phys. Lett. **31**, 18 (1977).

10. F. J. Marshall, S. A. Letzring, C. P. Verdon, S. Skupsky, R. L. Keck, J. P. Knauer, R. L. Kremens, D. K. Bradley, T. Kessler, J. Delettrez, H. Kim, J. M. Soures, and R. L. McCrory, Phys. Rev. A **40**, 2547 (1989).

11. R. R. Johnson *et al.*, Phys. Rev. A **41**, 1058 (1990).

12. Y. Kitagawa *et al.*, Phys. Rev. Lett. **75**, 3130 (1995).

13. K. A. Tanaka *et al.* Phys. Plasmas **2**, 2495 (1995).

14. K. A. Brueckner and S. Jorna, Rev. Mod. Phys. **46**, 325 (1974).

15. Laboratory for Laser Energetics LLE Review **82**, 49, NTIS document No. DOE/SF/19460-344 (2000). Copies may be obtained from the National Technical Information Service, Springfield, VA 22161.

16. Laboratory for Laser Energetics LLE Review **81**, 6, NTIS document No. DOE/SF/19460-335 (1999). Copies may be obtained from the National Technical Information Service, Springfield, VA 22161.

17. T. J. Kessler, Y. Lin, J. J. Armstrong, and B. Velazquez, in *Laser Coherence Control: Technology and Applications*, edited by H. T. Powell and T. J. Kessler (SPIE, Bellingham, WA, 1993), Vol. 1870, pp. 95–104.

18. T. R. Boehly, V. A. Smalyuk, D. D. Meyerhofer, J. P. Knauer, D. K. Bradley, R. S. Craxton, M. J. Guardalben, S. Skupsky, and T. J. Kessler, J. Appl. Phys. **85**, 3444 (1999).

19. S. Skupsky, R. W. Short, T. Kessler, R. S. Craxton, S. Letzring, and J. M. Soures, J. Appl. Phys. **66**, 3456 (1989).

20. D. D. Meyerhofer, J. A. Delettrez, R. Epstein, V. Yu. Glebov, V. N. Goncharov, R. L. Keck, R. L. McCrory, P. W. McKenty, F. J. Marshall, P. B. Radha, S. P. Regan, S. Roberts, W. Seka, S. Skupsky, V. A. Smalyuk, C. Sorce, C. Stoeckl, J. M. Soures, R. P. J. Town, B. Yaakobi, J. D. Zuegel, J. Frenje, C. K. Li, R. D. Petrasso, D. G. Hicks, F. H. Séguin, K. Fletcher, S. Padalino, M. R. Freeman, N. Izumi, R. Lerche, T. W. Phillips, and T. C. Sangster, Phys. Plasmas **8**, 2251 (2001).

21. S. Skupsky and R. S. Craxton, Phys. Plasmas **6**, 2157 (1999).

22. M. C. Richardson, P. W. McKenty, F. J. Marshall, C. P. Verdon, J. M. Soures, R. L. McCrory, O. Barnouin, R. S. Craxton, J. Delettrez, R. L. Hutchison, P. A. Jaanimagi, R. Keck, T. Kessler, H. Kim, S. A. Letzring, D. M. Roback, W. Seka, S. Skupsky, B. Yaakobi, S. M. Lane, and S. Prussin, in *Laser Interaction and Related Plasma Phenomena*, edited by H. Hora and G. H. Miley (Plenum Publishing, New York, 1986), Vol. 7, pp. 421–448.

23. T. E. Blue *et al.*, J. Appl. Phys. **54**, 615 (1983).

24. H. Azechi *et al.*, Appl. Phys. Lett. **49**, 555 (1986).

25. H. Azechi, M. D. Cable, and R. O. Stapf, Laser Part. Beams **9**, 119 (1991).

26. M. D. Cable and S. P. Hatchett, J. Appl. Phys. **62**, 2233 (1987).

27. Laboratory for Laser Energetics LLE Review **83**, 130, NTIS document No. DOE/SF/19460-357 (2000). Copies may be obtained from the National Technical Information Service, Springfield, VA 22161.

28. F. H. Séguin, C. K. Li, D. G. Hicks, J. A. Frenje, K. M. Green, R. D. Petrasso, J. M. Soures, D. D. Meyerhofer, V. Yu. Glebov, C. Stoeckl, P. B. Radha, S. Roberts, C. Sorce, T. C. Sangster, M. D. Cable, S. Padalino, and K. Fletcher, Phys. Plasmas **9**, 2725 (2002).

29. E. L. Alfonso, I. Anteby, and D. R. Harding, Fusion Technol. **38**, 149 (2000).

Equation-of-State Measurements of Porous Materials on OMEGA: Numerical Modeling

Introduction

The equation of state (EOS) of materials at high densities and pressures is of wide interest to inertial confinement fusion (ICF), planetary physics, and astrophysics. The EOS at these conditions often involves a mixture of atomic, ionic, and molecular species, making *ab initio* theoretical modeling prohibitive. Experiments to constrain EOS models have been performed using static methods such as diamond-anvil cells[1] and at higher pressures using dynamic methods, such as shocks generated by light-gas guns,[2] lasers,[3] and even nuclear explosions.[4,5] Of these methods, laser-driven shocks currently provide the best method available for not only accessing the high pressures of interest, but performing accurate measurements necessary to determine the EOS.

The Hugoniot of a material is the set of thermodynamic states, e.g., pressure and density, that can be reached after the propagation of shock waves of various strengths through the material. The measurement of a Hugoniot represents only a finite number of points along a single line through pressure–density space. While this by no means uniquely determines the EOS, it may constrain it. If the experimental data are determined to a great enough precision, they may even (as is hoped for in the impedance-matching measurements of deuterium) rule out competing EOS models.[6] Even though Hugoniot data may not constrain all regions of the EOS, the principal and secondary Hugoniots are of primary interest in applications relevant to ICF, since the gain of target designs is sensitive to the timing of two shocks for most direct-drive designs and as many as four shocks for indirect-drive designs.

Foams play a key role in the so-called above-ground experiments of the Stockpile Stewardship Program (SSP).[7] In support of the SSP, a series of experiments designed to study the EOS of foams began in the past year at LLE. In addition, high-gain, direct-drive ICF target designs have been proposed that use foams, making their properties of interest in ICF as well. For instance, in the designs of Colombant *et al*.,[8] foam is used as ablator material, in conjunction with an outer layer of a high-atomic-number material such as Au. In these designs, the foam is preheated by radiation from the outer layer and has substantially higher ablation velocities, resulting in a more stable outer surface. In other "wetted-foam" designs,[9] the higher atomic number of the foam results in greater absorption and increased laser energy coupled into the target, allowing more fuel to be used, producing higher gain. The models of both Colombant[8] and Skupsky[9] use foam to increase the target performance, in contrast to earlier foam designs, which proposed the use of foam only as a matrix to contain liquid DT or as a means to reduce imprint.[10,11] Direct-drive ICF target designs usually use a pulse that drives two main shocks into the target. The performance of these targets depends in part on the timing of these shocks, making determination of the wetted-foam EOS essential.

Several laser-driven shock experiments have been performed to determine the Hugoniot of foams of various densities and constituent materials. Benuzzi *et al*.[12] and Batani *et al*.[13] determined the shock speed and post-shock pressure as a function of initial foam average density for values from 5 to over 1000 mg/cc, for TMPT [trimethylol propane triacrylate ($C_{15}H_{20}O_6$)]. Koenig *et al*.[14] subsequently determined the pressure as a function of density for a range of initial TMPT foam densities, comparing their results to a Hugoniot calculated with the *SESAME* EOS, and inferring the amount of preheat necessary for agreement. The experiments performed at LLE complement these by focusing on carbonized resorcinol aerogel foam (CRF), a carbonized derivative of resorcinol formadlehyde (RF).[15] Aerogels are generally of interest because of their ultrafine cell and pore sizes (smaller than 1000 Å; by comparison, TMPT has pore sizes ~1 μm). Also, the carbonized derivative CRF has the benefit of greater material strength. CRF is being studied specifically because of its use in the Stockpile Stewardship Program. Unlike RF, CRF is optically opaque, potentially complicating the characterization that is necessary for application in ICF wetted-foam targets. For this reason, RF, TMPT, CH, and other foams similar to TMPT (such as divinyl benzene and ethyleneglycol dimethacrylate) are of potential interest for ICF target designs.

Because of their porosity, shocked foams exhibit behaviors not found in continuous materials: For example, if the porosity is large enough, it is possible for the shocked foam to have a lower density than that of its composite material. Probing the properties of shocked foams provides the potential for greater understanding of the structural physics of porous materials.

This article describes ongoing efforts at LLE to investigate the properties of CRF at high pressures and densities, focusing on the theoretical design of the experiments. In the following section the method used to determine the Hugoniot of foam samples is described as well as the resulting sensitivity to experimental uncertainty. Following that, the procedure used to calculate the Hugoniot is presented. The simulations used to design the experiments are then described, as well as the requirements placed on the target and pulse for a high-accuracy Hugoniot measurement experiment. These are followed by a discussion of the results.

The Impedance-Matching Method

When a sound wave encounters an interface between two materials, the strength and properties of the reflected and transmitted waves are determined by the *acoustic impedance* ρc, where ρ is the density and c the sound speed, in the two materials: if the acoustic impedance is continuous across the interface, the wave travels from one material to the other without changing speed; otherwise a wave is reflected as well as transmitted. As a sound wave is essentially a weak shock wave traveling at the sound speed, the behavior for a strong shock is similar: The acoustic impedance is replaced by the product of the density with the shock speed, ρU_S. If the shock encounters an increase in this quantity at a material interface between two materials, a shock is reflected back into the first material as well as transmitted into the second; otherwise a shock is transmitted and a rarefaction wave reflected. (A rarefaction wave is a propagating region that grows in time, in which the density and pressure drop as the material is accelerated.)

The *impedance-matching method*[16] uses the interaction of a shock wave with an interface between materials of different "hardness" (ρU_S) to determine a material's Hugoniot using the EOS of a reference material. A shock is sent through a layer of material of known EOS into a layer of the material under study (e.g., foam) in contact with the known material. Al is used as a reference material since it has been well characterized in previous studies at the pressures of interest here.[17] In these experiments the shock is generated by laser-driven ablation. The Rankine–Hugoniot (RH) jump equations for pressure and density provide two equations for the post-shock conditions (pressure p and density ρ) in the foam in terms of the known initial conditions (pressure p_0 and density ρ_0), the shock speed U_S, and the post-shock particle speed U_p. These conditions are applied across the shock front in both the Al and the foam, giving four equations in eight unknowns. Assuming that no gap forms between the Al and the foam, the pressure and the post-shock speed are continuous across that interface, providing an additional two constraints. Thus, measurement of the shock speeds in the two materials is sufficient to fully describe the system. (The shock speed is assumed to be equal to the average shock speed.) Measurement of the shock-breakout times from the Al and foam using the VISAR interferometer[18] allows determination of the average shock speed in each layer. The particle speed in the foam is inferred from the measured average shock speed in the Al, combined with knowledge of the Al EOS. This process is described in detail in the next section.

The reason the impedance-matching method was chosen for these experiments can be seen by examination of alternate methods. Other methods that have been used to determine a material's Hugoniot include the following: (1) The symmetric method, involving colliding two planar samples, where both the sample speed before contact and the resulting shock speed are measured. This method has the advantage of not relying upon knowledge of the EOS of a standard material. It requires, however, that the material speed be measured, for instance with side-on radiography. It also requires that the sample withstand being driven by the laser without bowing or loss of structural integrity. (2) The reshock method, which is similar to the impedance-matching method, except that the shock is sent first through the unknown sample, and subsequently into the material of known EOS. As in impedance matching, measurement of the shock speeds in both materials allows determination of the shocked state of the material of unknown EOS, given knowledge of the EOS of the standard. Because the former is shocked twice, this method allows access to higher pressures than the impedance-matching method. Computation of the Hugoniot, however, is less accurate. (3) A modification of the impedance-matching method has been suggested[19] in which a foot pulse is used to raise the entire target to a higher initial pressure (given by the ablation pressure) after which the intensity is increased and a main shock is launched and tracked using side-on x-ray radiography. This method allows access to still higher pressures but also requires that the laser pulse be sufficiently long for pressure equilibrium to be reached, which may be prohibitively long. (These methods and other methods

for experimentally ascertaining EOS properties without determining the Hugoniot are discussed in Refs. 16 and 20.)

In addition to the standard impedance-matching method, the experiments on OMEGA will explore the *direct* method, in which both the shock speed and the (post-shock) particle speed are measured using side-on radiography (e.g., see Ref. 21). This method replaces the error introduced by using a known EOS to determine the particle speed with the uncertainty, which may be lower, of determining the interface position from side-on radiography.

Calculation of the Hugoniot and Sensitivity to Measurement Uncertainty

As mentioned above, the Hugoniot of the foam is calculated using the known Hugoniot and isentrope of the reference material. For the data shown here, a quotidian-equation-of-state (QEOS)[22] table for Al was used.[23] In principle, any reference EOS may be used to determine the conditions (pressure, density, fluid speed) in the foam after the passage of the primary shock. When the primary shock enters the foam from the Al (which has a higher acoustic impedance), a rarefaction wave (RW) is sent back into the Al. This RW has the effect of equalizing the pressure and velocity in the Al and foam. This is shown schematically in Fig. 90.6, which contain plots of the pressure and density near the Al/foam interface (the dashed line in Fig. 90.6) before [(a) and (b)] and after [(c) and (d)] the shock has passed from the Al into the foam. Assuming there are no gaps between the Al and the foam, the velocity and pressure on either side of the interface (that is, regions *i* and *ii*) must be equal. Thus, the post-shock pressure and velocity in the foam are equal to the values in the Al after the passage of the RW. In Fig. 90.6(c) and 90.6(d) this is shown by the continuity of the pressure across the interface. Since the EOS of the Al is known, these conditions (in region *ii*) may be used to determine the conditions in the Al before the RW, but after the passage of the primary shock (i.e., region *iii*).

This process is shown graphically in Fig. 90.7. The RH jump conditions for mass, pressure, and energy are given by, respectively,

$$\rho\left(U_s - U_p\right) = \rho_0\left(U_s - U_0\right),$$

$$p - p_0 = \rho_0\left(U_s - U_0\right)\left(U_p - U_0\right),$$

$$E - E_0 = \frac{1}{2}\left(p + p_0\right)\left(V_0 - V\right),$$

where ρ is the density, p is the pressure, E is the internal energy, $V = 1/\rho$, zero subscripts refer to pre-shock values, U_s is the shock speed, and U_p is the post-shock speed.[16] The Al standard EOS is used in a form tabulated by isotherms. The states that lie on the Hugoniot may be determined for a given isotherm using the RH equation for energy. For the strong shocks considered here, the initial pressure and energy are much smaller than their post-shock values and may be taken to be zero. Combining the RH equations for mass and momentum, and setting $U_0 \rightarrow 0$ (as is the case in the experiment), the shock speed is given along the Hugoniot by

$$U_s^2 = \frac{p - p_0}{\rho - \rho_0} \times \frac{\rho}{\rho_0}.$$

The point along the Hugoniot (the solid line in Fig. 90.7) corresponding to the state of the Al just after the passage of the primary shock is that for which U_s is given by the measured shock speed U_{Al}.

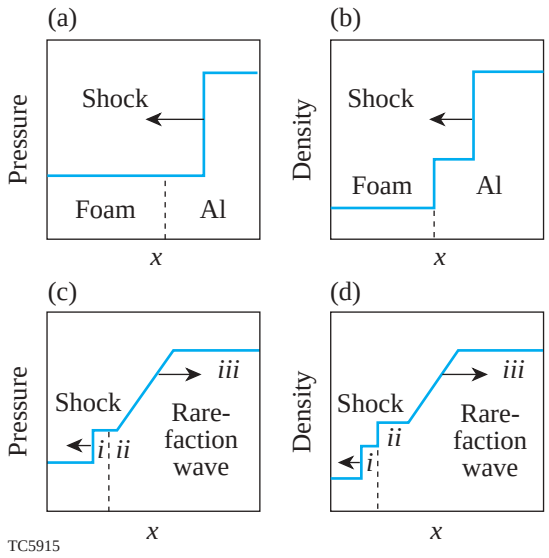

Figure 90.6
A schematic representation of the pressure and density near the Al/foam interface (represented by a dashed line) before [(a) and (b)] and after [(c) and (d)] passage of the shock from the foam into the Al. When the shock passes into the foam, a rarefaction wave is sent back into the Al, equalizing the pressure and velocity in the two materials. Notice that while the density changes across the interface, the pressure is continuous.

Assuming radiative losses are insignificant, the RH equations are satisfied, and the states reached by the RW lie along the release isentrope (the dashed line in Fig. 90.7) intersecting the shocked Al state determined above. The release isentrope may be calculated simply by finding, for each isotherm, the states for which the entropy is unchanged. The entropy change is given in terms of temperature and density changes by

$$ds = c_v \frac{dT}{T} - \left.\frac{dp}{dT}\right|_\rho \frac{d\rho}{\rho^2}$$

(see, e.g., Ref. 24). The particle speed along the release isentrope is computed using the relation (see, e.g., Ref. 20)

$$U_p = \int_{\rho_0}^{\rho} c_s(\rho)\, d\ln\rho = -\int_{V_0}^{V} \left(-\frac{\partial p}{\partial V}\right)_s^{1/2} dV.$$

The final state along the isentrope reached by the RW is that intersected by the Rayleigh line given by the RH momentum equation in the foam (again, where $U_0 = 0$), $p = \rho_0 U_{\text{foam}} U_p$.

Finally, once the post-shock pressure and particle speed in the foam are calculated, the post-shock foam density may be found from the RH mass equation

$$\rho_{\text{foam}} = \rho_0 U_{\text{foam}} \Big/ \left(U_{\text{foam}} - U_p\right).$$

Uncertainty in the calculated Hugoniot is due to both the uncertainty in the measurement of the shock speeds and the calculation of the post-shock pressure and density in the foam. The final uncertainty δP in the pressure, for instance, given the measured uncertainties δU_{Al} and δU_{foam} in the shock speeds, is given by

$$\delta P = \sqrt{\left(\frac{\partial P}{\partial U_{\text{Al}}}\delta U_{\text{Al}}\right)^2 + \left(\frac{\partial P}{\partial U_{\text{foam}}}\delta U_{\text{foam}}\right)^2},$$

and likewise for the uncertainty δU_p in the foam post-shock particle speed. The necessary partial derivatives are calculated numerically by calculating $\Delta P\left(\Delta U_{\text{Al}}, \Delta U_{\text{foam}}\right)$, in the limit that $\Delta U_{\text{Al}} \to 0$ or $\Delta U_{\text{foam}} \to 0$. The values of the calculated partial derivatives are required to converge in these limits in order to calculate the final uncertainty. The uncertainty $\delta\rho$ in the density is given by the chain rule:

$$\delta\rho_{\text{foam}} = \frac{\partial \rho_{\text{foam}}}{\partial U_p}\delta U_p = \frac{\rho_0 U_{\text{foam}}}{\left(U_{\text{foam}} - U_p\right)^2}\,\delta U_p.$$

As can be seen from this expression, the closer the shock speed is to the particle speed in the foam, the more uncertain the determination of the foam post-shock density. For example, consider an experiment with shock speeds of 28 μm/ns in the Al and 40 μm/ns in the foam. The corresponding post-shock

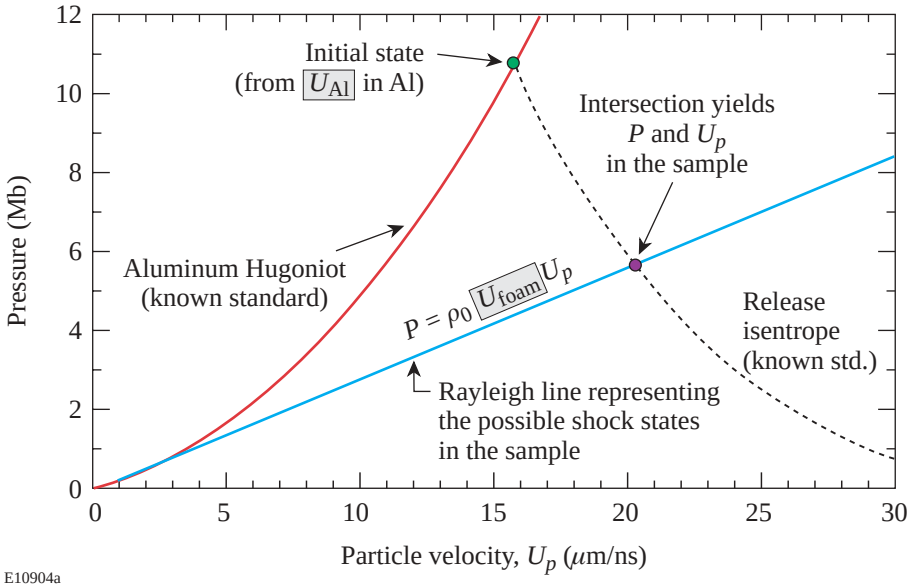

E10904a

Figure 90.7
A graphical representation of the process used to determine the foam Hugoniot from the measured shock speeds.

conditions in the foam are ρ = 0.59 g/cc and p = 1.3 Mbar. To achieve an uncertainty of even 0.1 g/cc (17%) in the calculated density, the measured uncertainty in the shock speeds (assuming they are equal) must be less than ~2%. The corresponding uncertainty in the pressure is ~13%.

The preceding procedure to determine the Hugoniot may be performed, for purposes of estimation, entirely analytically if a linear relationship is assumed between the shock and particle speeds in the Al, $U_{\mathrm{Al}} \approx C + sU_p$ (see, e.g., Ref. 20). For the Al *SESAME* table[25] these constants are given approximately by $C \sim 5.35$ km/s, $s \sim 1.34$ for shock speeds between 10 and 30 km/s. In this case the uncertainties may also be estimated analytically.[26,27]

Target Design

As described above, only *average* shock speeds are measured experimentally. To accurately determine the Hugoniot, the target and pulse must be designed so that the shock is steady. The primary shock will remain steady in the Al and CRF only if it is not overtaken by secondary rarefaction waves and shocks generated by the passage of the primary shock between different material layers.

At least three other factors constrain the design of the target: First, the uncertainty in the measured average shock speed is less for a thicker layer, since it is based on a determination of the breakout time of the shock. Second, at the end of the laser pulse a rarefaction wave (RW) is sent into the target. It can be shown[28] that the RW always moves faster than the primary shock because the post-shock fluid speed plus the sound speed in the post-shock material is greater than the shock speed. The duration of the pulse must be sufficient so that the RW does not reach the primary shock before it breaks out of the target. (For a single-layer target, the RW catches the primary shock at about a time equal to twice the pulse duration.[29]) Third, the ablator layer(s) must be of a sufficient optical thickness to prevent radiation from the corona from preheating the sample layers. Preheat not only changes the initial conditions seen by the shock but nonuniformly alters the temperature and density, affecting shock steadiness. The effects of radiative preheat are discussed further in the next section. (For a further discussion of preheat effects see Ref. 30.)

Figure 90.8 shows a space–time diagram from a *LILAC* simulation[31] of a sample target. (All *LILAC* simulations described here use the *SESAME* EOS.[32]) A schematic of the target is shown in Fig. 90.9. The 1-D simulation represents a slice parallel to the x axis, which cuts through the thin side of the Al step and the foam. The locations of the shocks and RW's in Fig. 90.8 are determined from the local variations in inverse pressure scale length $\left|L^{-1}\right| \equiv \left|\partial \ln p/\partial x\right|$ (in $\mu\mathrm{m}^{-1}$), where p is the pressure and x is the distance into the target. For clarity in identification of shocks and RW's, the target in this simulation is driven by a steady 3.5-ns , 200-TW/cm^2 laser pulse. The RW launched from the ablation surface at the end of the laser pulse may be seen in the neighborhood of 3.6 ns, 100 μm. Note that the reflected RW from the Al/CRF interface results in a second, inward-traveling shock when it reaches the ablation surface.

To predict shock steadiness and compare the results of simulations with experimentally measured shock speeds, the shock position and velocity must be determined from *LILAC* simulations. The former is found by determining the location of the local maxima of L^{-1}. These correspond to abrupt changes in the pressure, due to both shocks and material interfaces. Some of these maxima may be ruled out by requiring that $L > 0$. Two additional criteria aid in locating the shock: First, since the global maximum of L^{-1} is often the rear surface (farthest from the laser) of the foam, the local maximum closest to the front (or laser side), in most targets, corresponds to the shock. Second, the shock may also be identified as the maximum nearest to a local maximum in the derivative dT_e/dt of the electron temperature T_e with respect to time t, allowing the shock position to be unambiguously identified numerically.

Once the cell containing the position of the shock is determined as a function of time, the shock speed is computed: the location of the shock within a cell is approximated by fitting a parabola to $L^{-1}(x)$, using the value of L^{-1} in the cell, combined with $\partial L^{-1}/\partial x$ in the two neighboring cells. Due to the finite time resolution of the simulation, the shock velocity determined by differentiating the shock position is noisy. The noise has a time scale comparable to $\Delta z/U_s$ and, by choosing grid spacing Δz, can be made much smaller than the time scale for physical changes in U_s (due to, for instance, secondary shocks and rarefaction waves, and temperature and density gradients due to preheat). This noise is then removed by performing a linear regression at each time using n previous and subsequent values of the velocity. This least-squares fit acts as a low-pass filter, removing fluctuations in the shock speed having frequencies higher than $f \sim (2n\Delta t)^{-1}$, where Δt is the time interval for simulation output. (Note that Δt is typically much larger than the simulation time step.) As a result, the time interval for simulation output must be chosen to ensure that no hydrodynamic behavior of interest is removed during the smoothing process. A plot of the shock speed versus time for a typical target is shown in Fig. 90.10.

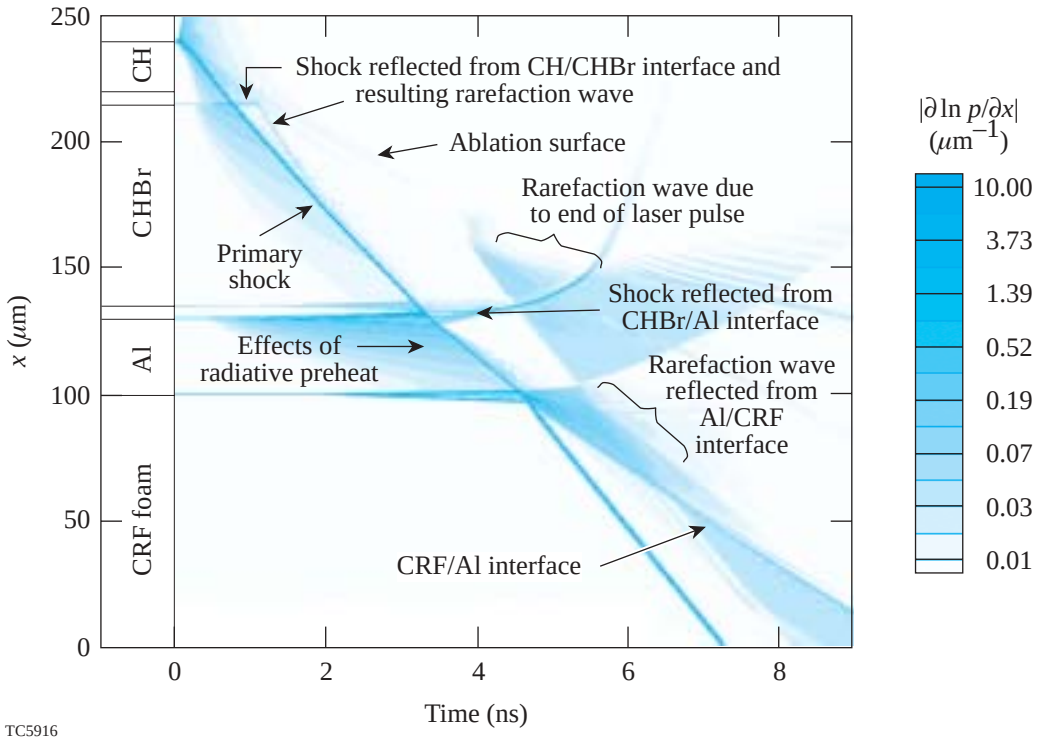

Figure 90.8
A space–time diagram from a *LILAC* simulation of a standard target. The location of the shocks and rarefaction waves (RW's) are determined from the local variations in inverse pressure scale length $\left|\partial \ln p/\partial x\right|$ (in μm^{-1}), where p is the pressure and x is the distance into the target. Note the RW's and secondary shocks that are generated when the primary shock reaches each material interface.

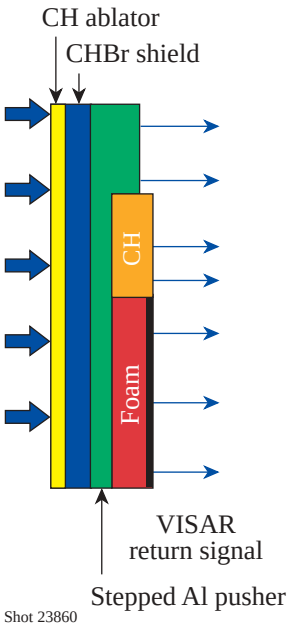

Figure 90.9
The structure of a standard target used in the EOS experiments on OMEGA. The target consists of a CH ablator, a CHBr radiation shield, a stepped Al layer, and a foam layer. Some of the targets also have a "witness plate" of, for instance, plastic, which is transparent to the VISAR laser.

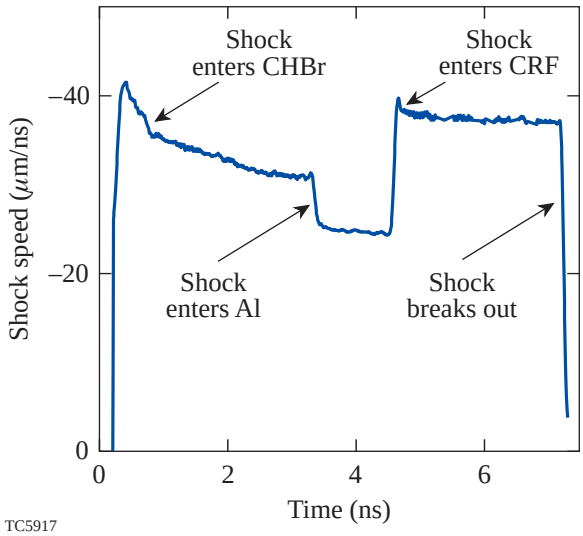

Figure 90.10
The primary shock speed as calculated from the *LILAC* simulation corresponding to Fig. 90.6. The rapid drop in the calculated shock speed at 7.2 ns corresponds to the breakout of the shock from the CRF. In this and other shock plots in this article, oscillations with periods of tens of picoseconds are due to numerical noise.

The targets used in these experiments initially consisted of a 20-μm-thick CH ablator, a 30-μm-thick Al layer (and 100 μm on the thick side of the Al step), and a 100-μm-thick foam layer. The resulting shock speed was found to be less steady than desired. Following Glendinning *et al.*,[33] an 80-μm-thick brominated-plastic layer was added after the CH ablator to serve as a radiation shield to prevent preheat. Radiative preheat causes a continuous change in the pre-shock temperature, density, and pressure. The speed of the primary shock changes as a result of the varying pre-shock conditions. In Fig. 90.11 a comparison of the computed shock speeds shows the improved shock steadiness when the CHBr radiation preheat shield is used. The steadiness of the shock may be measured by the standard deviation of the shock speed. (The steadiness σ is then given by a time-weighted average of the steadiness in the Al and the foam.) Without the CHBr preheat shield, $\sigma \sim 1.75$ μm/ns, and with the shield, $\sigma \sim 0.37$ μm/ns.

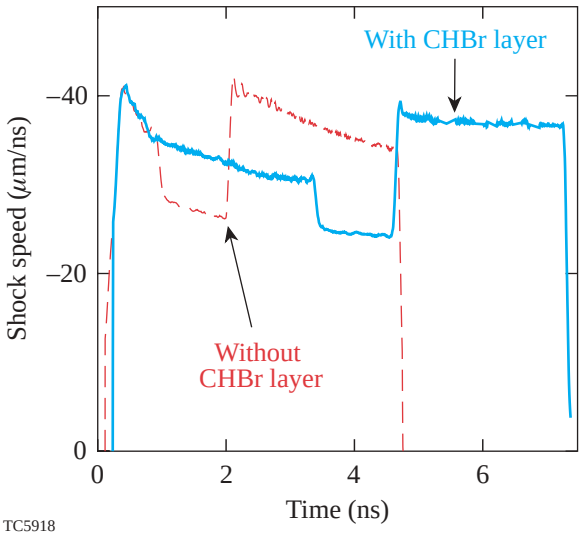

Figure 90.11
The shock speed for targets with (solid) and without (dashed) an 80-μm CHBr preheat shield, showing its effectiveness at reducing radiative preheat and the resulting increase in shock steadiness.

In addition to affecting shock steadiness, even a small amount of preheat may alter the Hugoniot for moderate and low pressures. Figure 90.12 shows the Hugoniot for CRF as calculated from QEOS, assuming 0.0252-eV (room temperature), 0.4-eV, and 1-eV initial temperatures. The room-temperature curve show a well-documented feature of porous materials, namely a Hugoniot that curves to lower densities for higher shock pressures. This behavior occurs because, for strong shocks in this regime, the thermal pressures produced in crushing the foam can become very large, resulting in lower densities. Note that while the final density ρ is lower than that of the constituent ($\rho_c \sim 1$ g/cc for a CH foam, for instance), it is still higher than the average initial foam density ρ_f, so that $\rho_f < \rho < \rho_c$. This anomalous behavior is described in Ref. 16 and has been observed in other materials as well.[5] This anomalous behavior is not seen in the 0.4-eV and 1-eV curves, indicating that at small preheat values the foam begins to behave more like a continuous solid. Impedance-matching experiments by Koening *et al.*[14] also found that agreement between the experimental and theoretical EOS's could be obtained only by assuming a small amount of preheat.

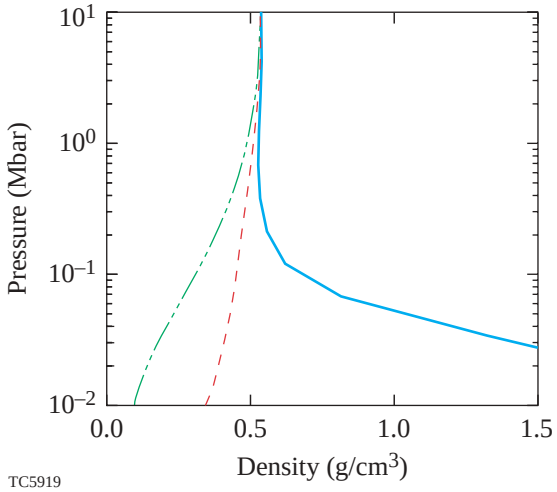

Figure 90.12
The Hugoniot calculated from the QEOS, for a room-temperature CRF foam (solid), a 0.4-eV foam (dashed), and a 1-eV foam (dashed–dotted). Notice that the Hugoniots for the heated foams do not show the anomalous behavior of decreasing density with increasing pressure.

Because the ablation pressure scales with the laser intensity as $p \propto I^{\alpha}$, where $\alpha \approx 2/3$ (Ref. 34) and because the pressure is proportional to the square of the shock speed for strong shocks, a temporal intensity perturbation would be expected to result in a shock speed perturbation of $\delta U/U_0 \approx (1/3)\delta I/I_0$. However, the laser drive is coupled to the post-shock target material through the conduction zone. As a result, the system behaves like a driven, damped harmonic oscillator, and perturbations in the drive of sufficiently high frequency have no significant effect on the primary shock. This may be seen in the shock speeds from simulations of a typical target in which 10%

amplitude modulations with 250-ps and 1-ns periods are imposed on a flattop pulse (see Fig. 90.13). (These pulses include a 100- to 200-ps rise and fall taken from a typical measured pulse.) These periods were chosen as characteristic of the time scales for variations observed in typical shots on OMEGA. The amplitude modulations launch a sequence of shocks (alternated with rarefaction waves) into the target, causing jumps in the shock speed when they catch up to the primary shock. For a 20-TW/cm^2 pulse, which produces a 440-kbar shock in the foam, the 1-ns modulation results in $\sigma \sim 3.7\%$, while the 0.25-ns modulation perturbs the shock speed in the foam by only $\sigma \sim 1\%$.

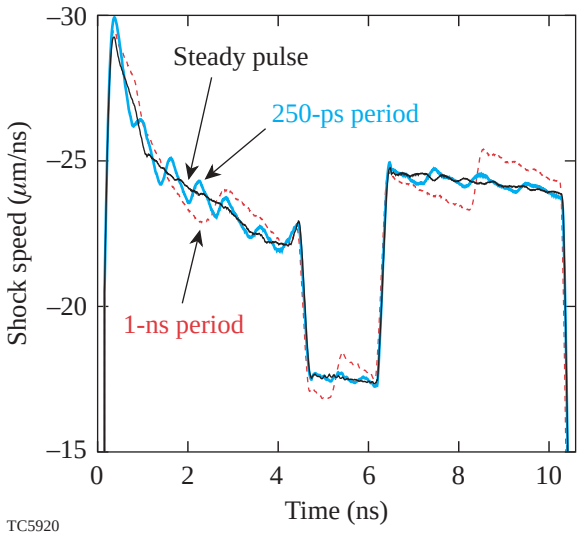

Figure 90.13
Shock speed for three simulations: one with a perfectly flat pulse (thick solid) and two with 10%-amplitude-modulated pulses with periods of 250 ps (thin solid) and 1 ns (dashed). All three pulses have a realistic 100- to 200-ps rise and fall taken from a typical measured pulse. Pressure modulations from the modulated pulse steepen into distinct shocks by the time they reach the primary shock, resulting in abrupt jumps in shock speed, as at 8 ns.

The σ for a range of perturbation periods and amplitudes is shown in Fig. 90.14. These data were computed using an array of *LILAC* simulations, with periods of 250 ps, 0.5 ns, …, 3.5 ns; amplitudes of 5% (1 TW/cm^2), 10%, 15%, 20%; and compared to a simulation with a flattop pulse.

Because the shock speed as a function of time in the Al and foam is not steady, it is possible (though unlikely) for a perturbed pulse to result in decreased standard deviation of the shock speed about the mean. For this reason, we have also computed the standard deviation σ_f not about the mean, but with respect to the shock speed of a flattop pulse (see Fig. 90.15).

For comparison, the discrete Fourier transforms of 32 pulses, with a range of average intensities from 4 TW/cm^2 to almost 100 TW/cm^2, from two experimental campaigns performed on OMEGA in October and November 2001, were computed (see Fig. 90.16). The contour lines associated with an average spectrum (heavy solid curves) as well as a best and worst (dashed curves) (using linear interpolation for non-integral mode numbers) for this set of shots are shown in Figs. 90.14 and 90.15. These figures show that for a typical OMEGA pulse, the unsteadiness of the shock may be expected, from 1-D simulations, to be below 1.5%.

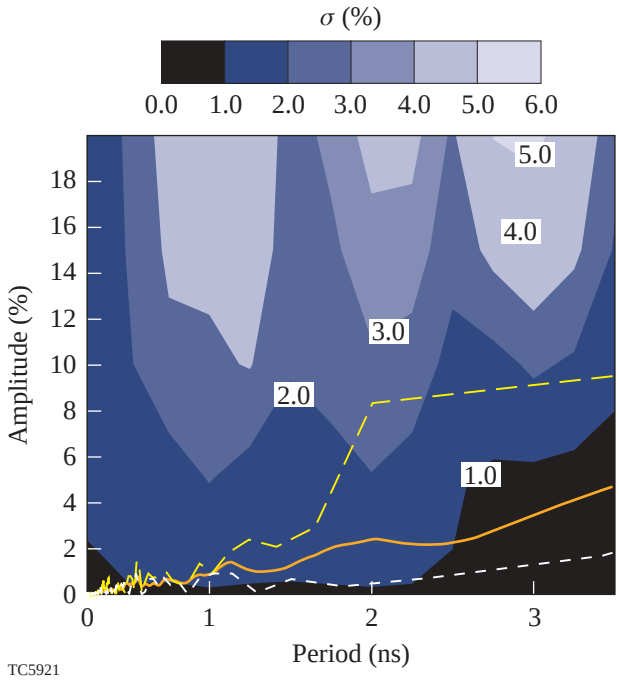

Figure 90.14
The standard deviation σ about the mean of the shock speed, during the shock transit through the Al and foam. The steadiness is shown as a fraction (in %) of the mean shock speed. For comparison, the average discrete Fourier transform of 32 shots from two EOS experiments is also shown (solid), as well as a best and worst spectrum (dashed). The sharpness of the contour lines reflects the finite number of simulations used. Note that because the period of the perturbations can be comparable to the hydrodynamic time scale, the phase of the perturbations can be important for larger amplitudes, creating the local extrema in σ [and in σ_f in Fig. 90.15 (see below)].

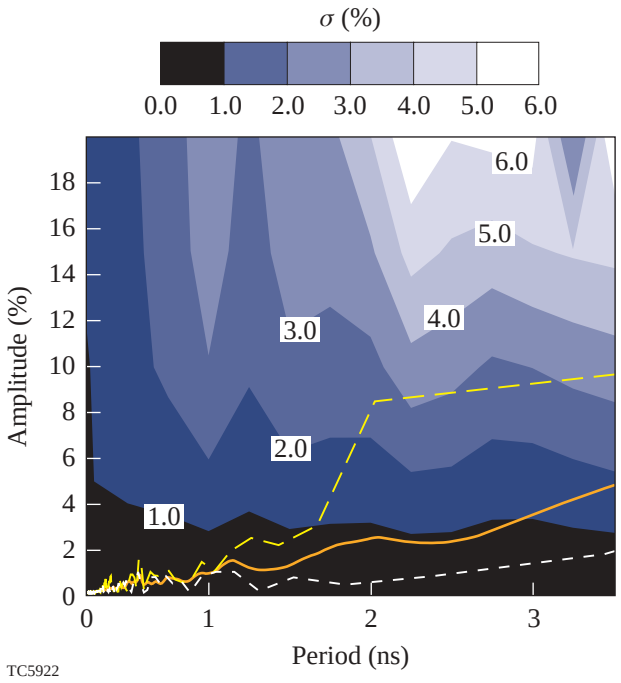

Figure 90.15
The standard deviation, as in Fig. 90.14, but computed with respect to the shock speed for a steady pulse, rather than with respect to the mean.

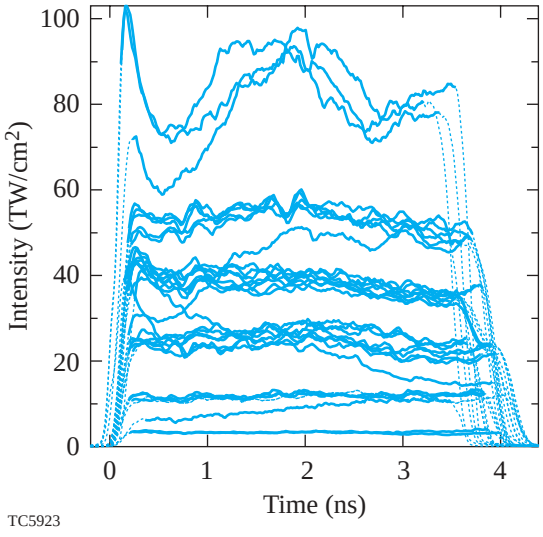

Figure 90.16
The pulses used in the comparisons shown in Figs. 90.14 and 90.15. Before computing the Fourier transforms, the rise and fall of the pulses were removed (dotted).

The preceding conclusion is based on the assumption that, since the amplitudes of the modulations are small, the modes remain linear. An additional simulation that was performed using an average pulse shape (of the normalized measured pulses) resulted in a pulse unsteadiness σ of 1.44%, to be compared to the 0.95% of the perfectly flattop pulse. This supports the conclusion that the typical pulse steadiness on OMEGA will in general, for this intensity, result in shock steadiness of less than ~1.5%.

Due to 2-D effects, such as shock curvature and transverse radiative transport,[35] defocusing of the beam by the corona,[33] and lateral plasma flow,[36] 1-D simulations systematically overestimate the shock speed. Fortunately, determining the foam Hugoniot requires only the EOS of Al, along with the measured shock speeds, and does not depend on precise agreement between the simulated and measured shock-breakout times. A comparison of experimental results with 1-D simulated shock speeds, in which the intensity was reduced to account for 2-D effects, is shown in Fig. 90.17. For this shot (27174) a 20% reduction was needed. In general, a sufficient margin is built into the 1-D target designs to allow for the systematic decrease in shock speed due to 2-D effects.

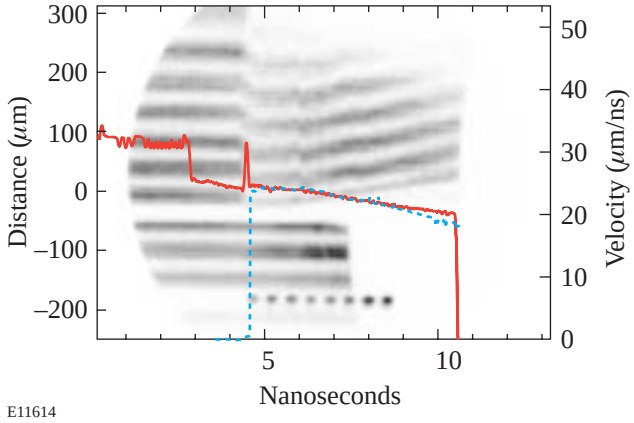

Figure 90.17
A comparison of the measured (dashed) and simulated (solid) shock speeds for shot 27174. To model 2-D effects, the intensity of the measured pulse was uniformly decreased by 20%. This target consisted of 20 μm CH, 5 μm glue (modeled by CH), 80 μm CHBr, 5 μm glue, 40 μm Al, and 140 μm quartz. The transparent quartz layer was used to determine shock speed as a function of time, for comparison with simulation. Because the density of quartz is close to that of Al, it also provides an indication of the typical shock speeds in the thick portion of the Al step. The measured shock speed was determined from the motion of the ASBO/VISAR fringes, which are also shown. The simulation and experiment were synchronized to the time of shock breakout into the quartz.

Discussion and Conclusions

A description of the theoretical tools used in the design of targets has been presented here, including the constraints presented by the requirement of minimal radiation preheat and shock steadiness. Even a small amount (0.4 eV) of preheat can alter the Hugoniot at pressures of less than 1 Mbar for 100-mg/cc CRF foam, potentially constraining the amount of allowable preheat. It has also been shown that the pulse steadiness of typical pulses on OMEGA is sufficient to ensure, on average, shock steadiness of less than 1.5% (for a typical 20-TW/cm^2, 3.5-ns pulse). If the measured shock speeds have an error of 1.5%, the resulting uncertainty in the density and pressure will be ~6.6% and ~2.4%, respectively, for a shock generated by laser illumination of this intensity. While this result does not rule out the effects of pulse steadiness, it suggests that other aspects of the experiment should be improved as well. Future experiments will also focus on the use of the "direct method," in order to reduce the uncertainty in the computed density by providing a direct measure of target compression.

ACKNOWLEDGMENT

This work was supported by the U.S. Department of Energy Office of Inertial Confinement Fusion under Cooperative Agreement No. DE-FC03-92SF19460, the University of Rochester, and the New York State Energy Research and Development Authority. The support of DOE does not constitute an endorsement by DOE of the views expressed in this article.

REFERENCES

1. R. J. Hemley and H. K. Mao, Phys. Rev. Lett. **61**, 857 (1988).
2. A. H. Jones, W. M. Isbell, and C. J. Maiden, J. Appl. Phys. **37**, 3493 (1966).
3. C. G. M. van Kessel and R. Sigel, Phys. Rev. Lett. **33**, 1020 (1974).
4. L. V. Al'tshuler *et al.*, Sov. Phys.-JETP **34**, 606 (1958).
5. R. F. Trunin, *Shock Compression of Condensed Materials* (Cambridge University Press, Cambridge, England, 1998).
6. G. W. Collins *et al.*, Science **281**, 1178 (1998).
7. R. Jeanloz, Phys. Today **53**, 44 (2000); *High-Energy-Density Physics Study Report*, National Nuclear Security Administration, U.S. Department of Energy, Washington, DC (6 April 2001).
8. D. G. Colombant *et al.*, Phys. Plasmas **7**, 2046 (2000).
9. S. Skupsky, R. Betti, T. J. B. Collins, V. N. Goncharov, D. R. Harding, R. L. McCrory, P. W. McKenty, D. D. Meyerhofer, and R. P. J. Town, "High-Gain, Direct-Drive Target Designs for the National Ignition Facility," to be published in the *Proceedings of the 2nd International Conference on Inertial Fusion Sciences and Applications*.
10. L. M. Hair *et al.*, J. Vac. Sci. Technol. A **6**, 2559 (1988).
11. M. Desselberger *et al.*, Phys. Rev. Lett. **74**, 2961 (1995).
12. A. Benuzzi *et al.*, Phys. Plasmas **5**, 2827 (1998).
13. D. Batani *et al.*, Plasma Phys. Control. Fusion **40**, 1567 (1998).
14. M. Koenig *et al.*, Phys. Plasmas **6**, 3296 (1999).
15. R. W. Pekala and F-M. Kong, Lawrence Livermore National Laboratory, Livermore, CA, UCRL-99846 (1988).
16. Ya. B. Zel'dovich and Yu. P. Raizer, in *Physics of Shock Waves and High-Temperature Hydrodynamic Phenomena*, edited by W. D. Hayes and R. F. Probstein (Academic Press, New York, 1966).
17. J. H. Campbell *et al.*, Laser Part. Beams **15**, 607 (1997).
18. L. M. Barker and R. E. Hollenbach, J. Appl. Phys. **43**, 4669 (1972).
19. J. W. Bates and A. N. Mostovych, Bull. Am. Phys. Soc. **46**, 43 (2001).
20. G. R. Gathers, *Selected Topics in Shock Wave Physics and Equation of State Modeling* (World Scientific, Singapore, 1994).
21. R. Cauble *et al.*, Phys. Plasmas **4**, 1857 (1997).
22. R. M. More *et al.*, Phys. Fluids **31**, 3059 (1988).
23. D. A. Young, Lawrence Livermore National Laboratory, private communication (2001).
24. F. Reif, *Fundamentals of Statistical and Thermal Physics* (McGraw-Hill, New York, 1965).
25. S. P. Marsh, ed. *LASL Shock Hugoniot Data*, Los Alamos Series on Dynamic Material Properties (University of California Press, Berkeley, CA, 1980).
26. N. C. Holmes, Rev. Sci. Instrum. **62**, 1990 (1991).
27. A. C. Mitchell and W. J. Nellis, J. Appl. Phys. **52**, 3363 (1981).
28. R. Courant and K. O. Friedrichs, *Supersonic Flow and Shock Waves*, Pure and Applied Mathematics, v. 1 (Interscience, New York, 1948), p. 141.
29. R. J. Trainor and Y. T. Lee, Phys. Fluids **25**, 1898 (1982).

30. J. J. Honrubia *et al.*, J. Quant. Spectrosc. Radiat. Transf. **61**, 647 (1999).

31. M. C. Richardson, P. W. McKenty, F. J. Marshall, C. P. Verdon, J. M. Soures, R. L. McCrory, O. Barnouin, R. S. Craxton, J. Delettrez, R. L. Hutchison, P. A. Jaanimagi, R. Keck, T. Kessler, H. Kim, S. A. Letzring, D. M. Roback, W. Seka, S. Skupsky, B. Yaakobi, S. M. Lane, and S. Prussin, in *Laser Interaction and Related Plasma Phenomena*, edited by H. Hora and G. H. Miley (Plenum Publishing, New York, 1986), Vol. 7, pp. 421–448.

32. S. P. Lyon and J. D. Johnson, Los Alamos National Laboratory, Los Alamos, CA, Report LA-UR-92-3407 (1992).

33. S. G. Glendinning, D. K. Bradley, R. C. Cauble, M. J. Edwards, H. Louis, J. C. Moreno, S. J. Moon, B. A. Remington, E. J. Turano, T. R. Boehly, R. S. Craxton, and R. Town, Bull. Am. Phys. Soc. **45**, 199 (2000).

34. R. E. Kidder, Nucl. Fusion **8**, 3 (1968).

35. D. Braun *et al.*, Bull. Am. Phys. Soc. **46**, 44 (2001).

36. M. Temporal *et al.*, Il Nuovo Cimento **19D**, 1839 (1997).

Observations of Modulated Shock Waves in Solid Targets Driven by Spatially Modulated Laser Beams

Introduction

Shock waves produced by laser-driven ablation are an important part of studies of inertial confinement fusion (ICF),[1,2] the equation of state of materials (EOS),[3–5] laboratory astrophysics,[6,7] and other high-energy-density sciences. In ICF, nonuniformities in the drive laser can produce nonuniform shocks that create mass perturbations in the target.[2] These perturbations can be amplified by the Rayleigh–Taylor (RT)[1] instability to a sufficiently large enough level to disrupt the implosion and reduce its performance. The propagation of these modulated shocks is determined by the physics of the laser-interaction region and stabilization processes;[8,9] hence, their measurement provides information about the intervening processes. Modulations in drive intensity can also be used to verify the scaling of shock strength (velocity) with drive intensity to better understand coupling efficiency and its scaling with intensity.

This article reports on novel experiments in which targets are driven with a laser beam having a single-mode, spatial-intensity modulation. The resultant ablation-pressure modulations produce shocks with spatially varying strengths (and velocities). The arrival times of the shock at various surfaces in the target are used to infer differences in the shock velocities and therefore the pressures produced by the modulated drive intensity. By placing an embedded layer within the target, the shock arrival at two surfaces is measured, thereby providing an added opportunity to observe the evolution of the modulated shock as it traverses the target. This evolution can be used to study dynamic effects in laser-produced plasmas, namely stabilization by dynamic overpressure.[9]

Experimental Results

In these experiments, 20-μm-thick CH (ρ = 0.92 g/cm^2) targets were irradiated with 351-nm laser light at average intensities of 6×10^{12} W/cm^2. A 0.5-μm-thick Al layer was embedded at the center (10 μm deep) of the target. This layer provided an intermediate surface where the shock arrival was detected. Modulations in drive intensity of ~5:1 produced ~3:1 modulations in shock pressure. Hydrodynamic simulation of these experiments is in good agreement with the average shock speeds, their modulations, and the resultant breakout times.

These experiments were conducted on the OMEGA[10] laser using a single drive beam having a distributed phase plate (DPP)[11] that produces a modulated intensity pattern at its focal spot. The phase plate was designed and fabricated to produce a one-dimensional irradiance distribution on a flat target placed in the quasi far field of the OMEGA laser beam. One-quarter of the Talbot cycle (the transition from only phase modulation to only intensity modulation) was used to achieve a sinusoidal irradiance distribution, with flat phase, from a sinusoidal phase distribution, with flat irradiance, in the near field of the laser. Photolithographic and ion-etching techniques were used to place a surface relief in fused silica.[11] As the laser beam traverses the etched-glass plate, it acquires the needed phase distribution from the etched pattern to produce a sinusoidal intensity distribution at the focal plane. The focusing lens was positioned to obtain a spatial wavelength of 60 μm at the target plane.

This beam was incident on the target at an angle of 23°. The modulations were oriented so that obliquity distortions were negligible in the modulation direction. The arrival of the shock front at the rear and embedded surfaces was detected using the active-shock-breakout (ASBO) diagnostic.[12] It uses a 532-nm (doubled Nd:YAG) probe laser directed onto the back of the experimental targets to detect shock velocity or breakout times.

Figure 90.18 shows the experimental arrangement with the UV drive laser incident from the left onto the front of the target and the ASBO probe laser incident from the right, probing the rear side of the target. The ASBO diagnostic normally uses the time-resolved displacement of VISAR (velocity interferometer system for any reflector) fringes[12,13] to detect shock velocity. In the case of opaque materials, the ASBO probe beam does not detect the shock wave within the material but records the disruption of the rear-surface reflectivity produced there by the arrival of the shock. (The release of the rear surface

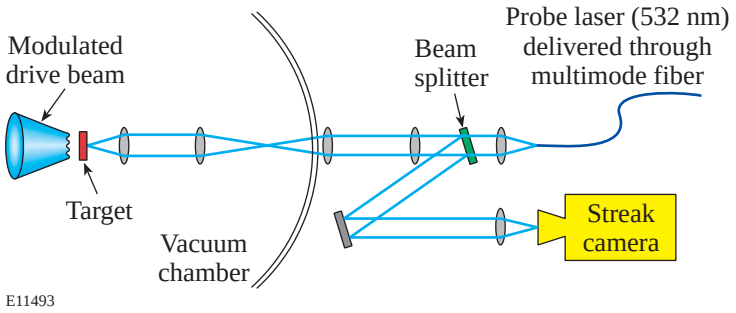

Figure 90.18
The experimental arrangement in the OMEGA target chamber. The UV drive laser is incident from the left, and the green probe beam is incident from the right. The incident beam has a DPP that produces sinusoidal intensity modulations at the focal plane. The reflected probe beam is directed to an optical streak camera.

produces an expanding plume of material that quickly absorbs the laser energy.) The shock speeds are deduced from the known material thickness and the shock transit time as measured by this breakout.

Figure 90.19(a) shows an optical image of the drive-laser intensity distribution obtained with a charge-coupled-device (CCD) camera placed at an equivalent target plane[14] for the OMEGA laser. The distributed phase plate described above produced the modulations in the laser focal spot. The focal position was chosen to produce modulations with a wavelength of ~60 μm; the resultant spot was about 800 μm in diameter.

Figure 90.19(b) is a plot of the intensity distribution in the vertical direction along the center of the image. The intensity modulations range between 5:1 and 3:1, depending on which area of the focal spot is analyzed. This variation occurs because the nonuniformities in phase and irradiance of the laser beam are comparable to those that produce the sinusoidal pattern. (These effects can be compensated for in future designs.) The absolute values for the on-target intensity were obtained by normalizing the total distribution of intensities to the incident laser power for shot 24569.

Figure 90.20 is a pinhole-camera image of the x rays emitted from an Au target irradiated by this beam [Fig. 90.19(a)] at an average intensity of ~10^{14} W/cm^2. This intensity is higher than that used to drive the targets but is used to produce sufficient x rays for imaging purposes. At this intensity the x rays are predominately from *n*-shell Au emission. The lower apparent modulation amplitude results from the nonlinear conversion of the UV to x-ray energy.

The opaque layer (0.5 μm of Al) embedded in the target provides an internal surface at which the shock arrival is detected. The depth of that imbedded layer was 10 μm from the irradiated surface; another 10 μm of CH was coated on the rear side. The heat front did not penetrate the front 10 μm of CH to the Al layer while the laser was on.

Figure 90.21 shows the time-resolved ASBO data for two shots, depicting the signal reflected from targets irradiated by the intensity distribution shown in Fig. 90.19. (The series of

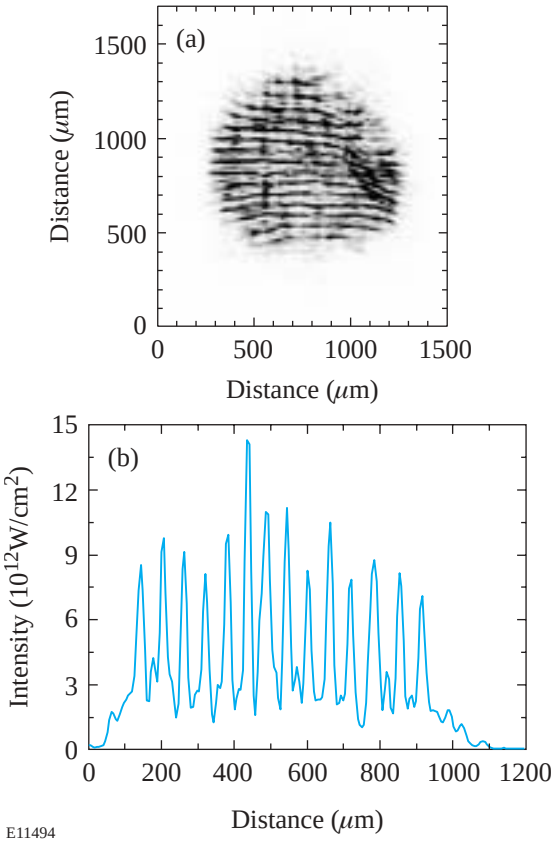

Figure 90.19
(a) An optical image at an equivalent target plane for the OMEGA laser. These modulations in drive intensity are created by a DPP placed in the beam and are used to create modulated shocks in the target. (b) A lineout of intensity along the centerline of the image.

dots across the bottom of the figures are temporal fiducial pulses, each separated by 0.548 ns.) For these experiments, one leg of the VISAR interferometer was blocked, producing a simple probe beam, giving a continuous spatial record of the shock-breakout time. The ASBO probe beam penetrates the rear portion of the target (10 μm of transparent CH) and reflects off the embedded Al layer. This reflection is seen as the dark portion of the image that extends from less than –1 to ~1 ns. (The horizontal streaks seen in these signals are due to the spatial speckle of the probe laser.) The drive laser began at 0 ns. At about +1 ns, the shock arrives at the Al layer and changes the layer's reflectivity, signaling the arrival of the shock at that surface. At that point, the signal to ASBO decreases but does not completely disappear. This reduction in signal results from either reduced reflectivity of the Al or reduced transmissivity of the rear CH section. Both are caused by the shock's arrival at the Al layer. The contour of change in reflectivity (dark to light transition) is modulated at the same spatial frequency as the incident laser modulations. The earlier occurrences of this transition represent the arrival of faster portions of the shock (shorter transit times) and later occurrences the slower portions (longer transit times). The lighter region persists until about 1.5 to 2 ns, then it disappears completely. This total loss of signal occurs when the shock arrives at the rear surface and that surface unloads, no longer reflecting the probe laser. Note that the extinction time of this light area is also modulated and it is in phase with the dark-to-light transition at ~1 ns. These transitions in target reflectivity mark the arrival of the shock front at each surface and can therefore be used to infer shock velocities and modulations in those velocities.

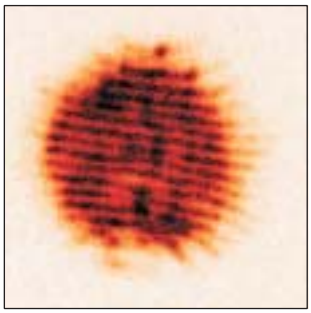
E11495

Figure 90.20
An x-ray pinhole-camera image of the x rays emitted from a Au target irradiated by the beam shown in Fig. 90.19(a).

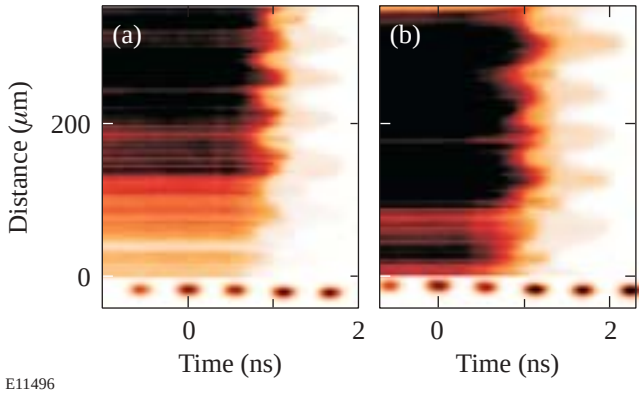

E11496

Figure 90.21
Streak records of probe beam reflection from (a) shot 24566 and (b) shot 24569. The dark signal from approximately –1 ns to +1 ns is the probe beam reflection off the unshocked Al layer within the target. The transition to the lighter area occurs when the shock arrives at the Al layer, reducing its reflectivity. The cessation of that light area (later in time) is caused by the arrival of the shock at the rear surface. The modulations in each of these transition regions result from different arrival times of the modulated shock in the target.

Analysis

Figure 90.22 shows a plot (solid curves) of the shock arrival times (at the Al layer and the rear surface) as a function of space as deduced from Fig. 90.21(b). Using these data and the thickness of the intervening target material, the shock speed as a function of space can be inferred. In the lower curve, the earliest times (corresponding to intensity peaks) occur at ~0.97 ns, and the latest times (intensity troughs) occur at ~1.15 ns. The respective times for the upper curves are 1.47 ns and 1.95 ns, where $t = 0$ is the start of the laser pulse. Each of these values represents the average of three peaks or troughs. (The trend to later times at the right end of these plots likely results from the finite size of the laser spot. Its edges have slightly lower intensity and hence produce slower shocks that arrive at the surfaces later in time.) Using the 10-μm distance for transit times at the peak and trough of the modulated shock, we find that the minimum shock speed is 12.5 μm/ns and the maximum is 20 μm/ns. The errors in velocity are expected to be $\lesssim$5% and arise mainly from uncertainties in target thickness ($\pm$0.1 μm) and determination of shock arrival time (~ $\pm$10 ps). Using the Hugoniot data for CH from *SESAME* tables,[15] these shock velocities correspond to pressures of 2.85 and 0.97 Mb, respectively. In a similar shot with an identical target, the

shock speeds were slightly higher but the modulations of similar size. Table 90.III lists the results for the two shots. The breakout times (t_P and t_T for peaks and troughs) at either 10 μm or 20 μm in the target were averaged over three spatial periods. V_- is the shock velocity given by the distance (10 μm) divided by the difference between later breakout times (troughs of shock); V_+ is the velocity associated with the earlier breakout times (peaks of shock). The pressures P_- and P_+ are inferred from the shock velocities V_- and V_+ using the *SESAME* equation-of-state tables. I_+/I_- is the ratio of intensity calculated from the pressure ratio P_+/P_- using the intensity scaling for pressure as given below.

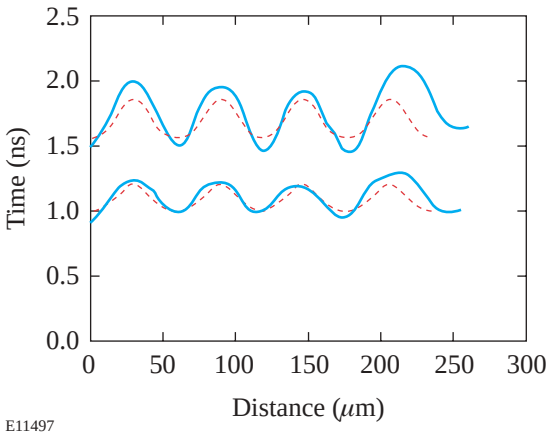

Figure 90.22
The shock arrival times versus space for shot 24566 [Fig. 90.21(b)]. The upper curve represents the contour of the shock arrival time at the rear surface; the lower curve for the arrival at the Al layer embedded at 10 μm. The dashed lines are the simulated arrival times of the shock at those surfaces.

The dependence of pressure on intensity has been established by considerable ICF research as $P(\text{Mbar}) = 40\,(I/\lambda)^{2/3}$ (Refs. 16–18), where λ is the laser wavelength in μm and I is laser intensity in 10^{15} W/cm^2. It is expected that for the intensities in these experiments, plasma instabilities are not important and this scaling law should be valid. At 6×10^{12} W/cm^2, the pressure should be ~2.7 Mb; a factor-of-5 reduction in intensity should produce a 0.9-Mb shock. These numbers are in good agreement with the observed pressure changes as inferred from the modulations in shock velocity, as shown in Table 90.III. Note that the pressure modulations are similar for the two shots, despite the differences in absolute pressure. This is because the sinusoidal intensity distribution was the same for both shots. The absolute pressure is different because the laser power (pulse shape and laser energy) was different (by a factor of ~5) for the two shots: 6×10^{12} W/cm^2 and 1.5×10^{12} W/cm^2.

Figure 90.23 shows a contour plot depicting density from a 2-D hydrodynamic simulation of this experiment using the computer code *ORCHID*.[19] The laser is incident from the left, and the shock (propagating to the right) can be seen as the first contour. A portion of the embedded AL layer (indicated in the figure) has been displaced by the shock. The laser intensity was 6×10^{12} W/cm^2 (average) in a sinusoidal intensity distribution with 60-μm wavelength and intensity modulation (peak-to-

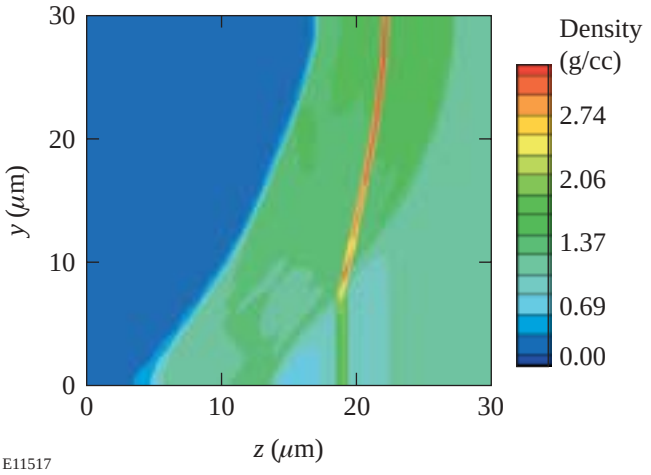

Figure 90.23
Density contours (at 1.39 ns) in a 2-D hydrocode (*ORCHID*) simulation of these experiments with an embedded Al layer as shown. The modulated laser (1/2 cycle of the sinusoidal modulation is shown) is incident from the left. The curved shock propagates to the right.

Table 90.III: Experimental results.

		Trough		Peak		Velocity		Pressure		Modulation	
Shot #	(W/cm^2)	t_{T20}	t_{T10}	t_{P20}	t_{P10}	V_-	V_+	P_-	P_+	P_+/P_-	I_+/I_-
24566	6×10^{12}	1.62	1.06	1.15	0.813	17.8	29.6	2.18	6.45	2.96	5.09
24569	1.4×10^{12}	1.95	1.15	1.47	0.973	12.5	20.1	0.97	2.85	2.94	5.04

valley) of 5:1. The predicted arrival time of the shock at the embedded layer and the rear surface is shown as dashed curves in Fig. 90.22.

Conclusion

These experiments have demonstrated a technique for observing modulated shocks in solid targets. Modulations in the drive intensity produce shocks with spatially varying speeds. The arrival of these shocks at surfaces of the target was detected with an optical probe beam. The transit times of the shocks through the targets provide the velocities at various points along the shock front and detect the modulations in shock velocity. These velocities were used to infer the resultant pressure modulations produced by modulations in drive intensity. The experimental results are consistent with established models for the intensity scaling of ablation pressure. The 2-D hydrocode *ORCHID* modeled the observed breakout times and modulations accurately. This technique will be useful for studying dynamic overpressure where ablation dynamics may alter the amplitude of shock modulations as it propagates through a target. In addition, these results confirm established scaling laws for ablation pressure with drive intensity.

ACKNOWLEDGMENT

This work was supported by the U.S. Department of Energy Office of Inertial Confinement Fusion under Cooperative Agreement No. DE-FC03-92SF19460, the University of Rochester, and the New York State Energy Research and Development Authority. The support of DOE does not constitute an endorsement by DOE of the views expressed in this article.

REFERENCES

1. J. D. Lindl, Phys. Plasmas **2**, 3933 (1995).
2. S. E. Bodner, D. G. Colombant, J. H. Gardner, R. H. Lehmberg, S. P. Obenschain, L. Phillips, A. J. Schmitt, J. D. Sethian, R. L. McCrory, W. Seka, C. P. Verdon, J. P. Knauer, B. B. Afeyan, and H. T. Powell, Phys. Plasmas **5**, 1901 (1998).
3. G. W. Collins *et al.*, Science **281**, 1178 (1998).
4. R. Cauble *et al.*, Phys. Plasmas **4**, 1857 (1997).
5. G. W. Collins *et al.*, Phys. Plasmas **5**, 1864 (1998).
6. B. A. Remington *et al.*, Science **284**, 1488 (1999).
7. B. A. Remington *et al.*, Phys. Plasmas **7**, 1641 (2000).
8. V. N. Goncharov, "Self-Consistent Stability Analysis of Ablation Fronts in Inertial Confinement Fusion," Ph.D. thesis, University of Rochester, 1998.
9. V. N. Goncharov, S. Skupsky, T. R. Boehly, J. P. Knauer, P. McKenty, V. A. Smalyuk, R. P. J. Town, O. V. Gotchev, R. Betti, and D. D. Meyerhofer, Phys. Plasmas **7**, 2062 (2000).
10. T. R. Boehly, D. L. Brown, R. S. Craxton, R. L. Keck, J. P. Knauer, J. H. Kelly, T. J. Kessler, S. A. Kumpan, S. J. Loucks, S. A. Letzring, F. J. Marshall, R. L. McCrory, S. F. B. Morse, W. Seka, J. M. Soures, and C. P. Verdon, Opt. Commun. **133**, 495 (1997).
11. T. J. Kessler, Y. Lin, J. J. Armstrong, and B. Velazquez, in *Laser Coherence Control: Technology and Applications*, edited by H. T. Powell and T. J. Kessler (SPIE, Bellingham, WA, 1993), Vol. 1870, pp. 95–104.
12. P. M. Celliers *et al.*, Appl. Phys. Lett. **73**, 1320 (1998).
13. L. M. Barker and R. E. Hollenbach, J. Appl. Phys. **43**, 4669 (1972).
14. S. P. Regan, J. A. Marozas, J. H. Kelly, T. R. Boehly, W. R. Donaldson, P. A. Jaanimagi, R. L. Keck, T. J. Kessler, D. D. Meyerhofer, W. Seka, S. Skupsky, and V. A. Smalyuk, J. Opt. Soc. Am. B **17**, 1483 (2000).
15. B. I. Bennett *et al.*, Los Alamos National Laboratory, Report LA-7130 (1978).
16. C. E. Max, *Physics of Laser Fusion, Vol. I*, Lawrence Livermore National Laboratory, Livermore, CA, UCRL-53107, Rev. 1 (1982).
17. W. M. Manheimer, D. G. Colombant, and J. H. Gardner, Phys. Fluids **25**, 1644 (1982).
18. S. M. Pollaine and J. D. Lindl, Nucl. Fusion **26**, 1719 (1986).
19. R. L. McCrory and C. P. Verdon, in *Inertial Confinement Fusion*, edited by A. Caruso and E. Sindoni (Editrice Compositori, Bologna, Italy, 1989), pp. 83–124.

Time-Dependent Electron Thermal Flux Inhibition in Direct-Drive Laser Implosions

Electron thermal conduction plays an important role in inertial confinement fusion (ICF):[1] it transports the laser energy absorbed near the critical surface into the overdense region and therefore directly affects the ablation process, the laser absorption, and implosion dynamics. The flux-limited Spitzer–Härm (SH) model[2] has been widely used to calculate the electron thermal conduction. In this model, the flux limiter f (typical value is 0.06)[3] is introduced to limit the SH electron thermal flux[4] and is given by

$$q_e = \min\left(fq_{\mathrm{FS}}, q_{\mathrm{SH}}\right), \tag{1}$$

where q_e is the electron thermal flux, q_{FS} is the free-streaming thermal flux defined as $q_{\mathrm{FS}} = n_e T_e \left(T_e/m_e\right)^{1/2}$, n_e is the electron number density, T_e is the electron temperature in energy units, m_e is the electron mass, and f is the flux limiter, respectively; q_{SH} is the SH electron thermal flux.[4] Because the flux limiter is empirically determined from the comparison between the numerical simulations and the experimental results,[5] it depends on the experimental conditions and the experimental uncertainties.

More-general approaches to calculating the electron thermal transport include a Monte Carlo method[6] and solving the Fokker–Planck (FP) equation. Many authors have reported that nonlocal electron thermal conduction is important, leading to a flux inhibition in laser-produced plasmas.[7–12] This article shows that the flux inhibition is time dependent for square pulses, which affects CH target implosions.

When the mean free path of the electrons is greater than the typical temperature and gradient scale lengths in the plasma, the transport is nonlocal. To calculate the nonlocal thermal conduction and to study its effect on the target implosions, a FP code was developed and combined with a one-dimensional hydrodynamic code (*LILAC*[13]). In our code, the electron velocity distribution function is expanded up to the $\ell = 3$ mode by Legendre polynomials of the direction cosines of the velocity vectors:[14]

Zeroth order:

$$\frac{\partial f_0}{\partial t} + \frac{1}{3}\left\{\frac{v}{\eta x^2}\frac{\partial}{\partial x}\left(x^2 f_1\right) - \frac{a_x}{v^2}\frac{\partial}{\partial v}\left(v^2 f_1\right)\right\}$$

$$- \frac{2}{15v^2}\frac{\partial U}{\partial x}\frac{\partial}{\partial v}\left(v^3 f_2\right) = C_{\mathrm{ee}} + S_0\,; \tag{2}$$

First order:

$$\frac{\partial f_1}{\partial t} + v\frac{\partial f_0}{\partial x} - a_x\frac{\partial f_0}{\partial v}$$

$$+ \frac{2}{5}\left\{\frac{v}{x^2}\frac{\partial}{\partial x}\left(x^2 f_2\right) - \frac{a_x}{v^3}\frac{\partial}{\partial v}\left(v^3 f_2\right)\right\}$$

$$- \frac{\partial U}{\partial x}\cdot f_1 - \left\{\frac{2}{5}\frac{\partial U}{\partial x} + \frac{1}{5x^2}\frac{\partial}{\partial x}\left(x^2 U\right)\right\} v^2\frac{\partial}{\partial v}\left(\frac{f_1}{v}\right)$$

$$= -\nu_{\mathrm{ei}} f_1\,; \tag{3}$$

Second order:

$$\frac{\partial f_2}{\partial t}+v\frac{\partial f_1}{\partial x}-\frac{v}{3x^2}\frac{\partial}{\partial x}\left(x^2 f_1\right)-\frac{2}{3}a_x v\frac{\partial}{\partial v}\left(\frac{f_1}{v}\right)$$

$$+\frac{3}{7}\left\{v\frac{\partial f_3}{\partial x}-\frac{a_x}{v^4}\frac{\partial}{\partial v}\left(v^4 f_3\right)\right\}+\frac{1}{7}\left\{\frac{2}{x^2}\frac{\partial\left(x^2U\right)}{\partial x}-4\frac{\partial U}{\partial x}\right\}f_2$$

$$-\left\{\frac{\partial U}{\partial x}-\frac{1}{3x^2}\frac{\partial\left(x^2U\right)}{\partial x}\right\}v\frac{\partial f_0}{\partial x}$$

$$-\frac{1}{21}\left\{8\frac{\partial U}{\partial x}+\frac{3}{x^2}\frac{\partial\left(x^2U\right)}{\partial x}\right\}v\frac{\partial f_2}{\partial v}$$

$$=-3\nu_{ei}f_2; \qquad (4)$$

Third order:

$$\frac{\partial f_3}{\partial t}+\frac{3}{5}\left\{v\frac{\partial f_2}{\partial x}-a_x v^2\frac{\partial}{\partial v}\left(\frac{f_2}{v^2}\right)\right\}=-6\nu_{ei}f_3; \qquad (5)$$

where f_0, f_1, f_2, and f_3 are the $\ell = 0$ (isotropic part), 1, 2, and 3 modes of the distribution function, respectively. For the closure of these coupled equations, we use the simplified f_3 equation without the correction terms for hydrodynamic motion and nonplanar geometry; f_3 is reset to 0 at the beginning of every time step because $f_3 << f_2$ but $\Delta f_3 \neq 0$.

In the above equations, C_{ee} is the electron–electron collision operator,[15] which is determined from the interaction of f_0 with itself only; ν_{ei} is the electron–ion collision frequency[12] given by

$$\nu_{ei}=\phi 4\pi n_e Z^* e^4 \ln\Lambda/m_e^2 v^3,$$

which effectively includes the corrections of higher-order terms neglected in the electron–electron collision operator,

$$\phi=\left(Z^*+4.2\right)/\left(Z^*+0.24\right).$$

The effective charge Z^* is defined by $Z^*=\langle Z^2\rangle/\langle Z\rangle$, where $\langle Z^2\rangle, \langle Z\rangle$ are the square of the charge and charge averaged over the ion species, respectively; e is the electron charge; $\ln\Lambda$ is the Coulomb logarithm,[16] and U is the ion velocity. The acceleration term is defined as $a_x = eE_x/m_e$, where the electric field E_x is obtained from the current-free condition $j = 4\pi e/3\int_0^\infty dv v^3 f_1 = 0$. S_0 is a source term that accounts for the change in the Maxwell distribution function

$$f_M = n_e\left(m_e/2\pi T_e\right)^{3/2}\exp\left(-m_e v^2/2T_e\right),$$

i.e., $S_0 = \delta(f_M)$, due to changes in the electron density and temperature from ionization, radiation transport, laser absorption, and PdV work calculated by the hydrodynamic code before the FP calculation. The friction term η limits the temperature change due to the thermal conduction according to the real gas heat capacity per electron c_{ve}. For a real gas, η is given by $\eta = 2c_{ve}/3$, where c_{ve} is obtained from the hydrodynamic code. After the FP calculation, the effective electron temperature, defined as $T_{eff} = 2\pi/m_e\int_0^\infty f_0 v^4 dv$, is returned to the hydrodynamic code. This is equivalent to solving the electron energy equation in the hydrodynamic equations.

We simulated the implosion of a polystyrene CH shell of 900-μm diameter and 20-μm thickness filled with 15 atm of D_2 gas. The 0.35-μm-wavelength laser pulse was a 1-ns-duration square starting at t = 200 ps with a rise time (0 to maximum) of 200 ps and a constant power of 25 TW from 0.4 ns to 1.4 ns. The irradiation intensity on the target was 9×10^{14} W/cm^2. Figure 90.24(a) shows the laser profile and the calculated electron thermal flux at the critical surface,

$$q_{FP} = 2\pi m_e/3\int_0^\infty v^5 f_1 dv,$$

normalized by the free-streaming thermal flux at the critical surface, q_{FS}. The ratio q_{FP}/q_{FS} can be defined as the flux-inhibition factor f if q_{FP} is assumed to be q_e, the "actual" flux when $fq_{FS} \le q_{SH}$ in Eq. (1). We observe that f increases until 400 ps and then decreases with time. This shows the time dependence of the flux-inhibition factor in an ICF implosion. This time dependence of the flux inhibition is explained by the properties of the SH model and the nonlocal nature of the transport.

For the first explanation, we consider the time dependence of the relation between q_{FS} and q_{SH}, described by the SH model. At the critical surface q_{FS} is a function of the electron

temperature only, and q_{SH} is written in terms of λ_0/L_T and the free-streaming flux as $q_{SH} = 16\sqrt{2}\,\pi^{-1/2}(\lambda_0/L_T)\,q_{FS}$, where λ_0 is the electron mean free path for 90° collision scattering[5] given by

$$\lambda_0 = v_{th}^4 \Big/ \left[4\phi\pi n_e Z^* \left(e^2/m_e\right)^2 \ln\Lambda \right],$$

where v_{th} is the thermal velocity defined by $v_{th} = \left(2T_e/m_e\right)^{1/2}$. L_T is the temperature gradient scale length defined as $T_e/\left(\partial T_e/\partial x\right)$. Figure 90.24(b) shows λ_0/L_T and electron thermal fluxes q_{FS}, q_{SH}, and q_{FP} at the critical surface. λ_0/L_T increases during the rise time of the laser pulse when T_e increases rapidly. It then decreases as L_T increases faster than λ_0 after 400 ps, at which time the constant laser pulse starts. Also, q_{FS} increases gradually with time in Fig. 90.24(b) as the electron temperature increases gradually. This leads to q_{SH} being almost constant after 400 ps since the increase in q_{FS} and the decrease in λ_0/L_T cancel each other in contributing to q_{SH}.

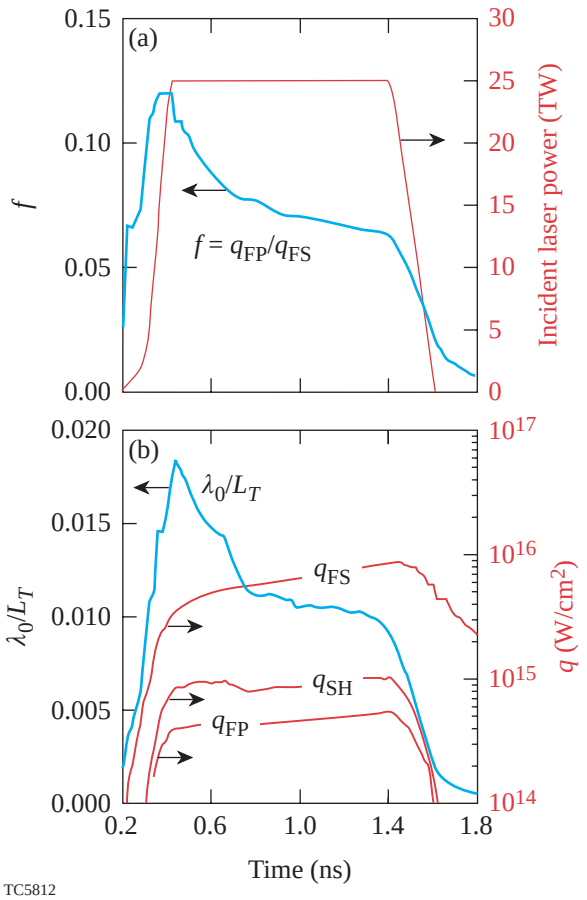

Figure 90.24
(a) Ratio of the q_{FP} and q_{FS} measured at the critical surface; (b) ratio of λ_0 and L_T. q_{FS} and q_{SH} are calculated from the n_e and T_e obtained by FP calculation.

The relation between q_{SH} and q_{FP} is determined by the nonlocal transport. As seen in Fig. 90.24(b), the FP flux has a trend similar to that of the SH flux: the ratio q_{FP}/q_{SH} stays between 0.5 and 0.6 during the constant laser power. Yet, during that time, because λ_0/L_T decreases with time, we would expect the flux to be less constrained. The fact that the ratio q_{FP}/q_{SH} stays constant indicates that flux inhibition from the SH flux due to the nonlocality of the electron transport increases with time.

From the time development of the flux-inhibition factor f and the absorbed laser power I_A, the absorbed laser power–averaged flux-inhibition factor, $\langle f \rangle = \int f I_A dt / \int I_A\, dt$, is estimated to be 0.075 for the sharp-cutoff flux-limited SH formula of Eq. (1). We also calculated $\langle f \rangle$ with the harmonic mean flux-limited SH model, which is given by

$$q_e^{-1} = \left(f q_{FS}\right)^{-1} + q_{SH}^{-1}.$$

For this model, $\langle f \rangle$ is 0.15.

The validity of our Fokker–Planck calculation is checked by comparing the calculated neutron burn history with both experimental results and results of the flux-limited SH model. The experiments were performed on the 60-beam OMEGA laser system[17] with the best smoothing conditions.[18] The neutron burn history was measured with the neutron temporal detector, which has a temporal accuracy of ±50 ps.[19] All the calculations were carried out with the real laser pulse and target conditions. In Fig. 90.25(a), we show three neutron rates calculated by FP and by SH with flux limiters of 0.07 and 0.06. These results are for 15-atm-D_2 gas pressure and 20-μm shell thickness irradiated by a 1-ns-duration square pulse. The results of both FP and SH with a flux limiter of 0.07 show good agreement with the experimental result. The results shown in Fig. 90.25(b) for a fuel gas pressure of 3 atm also agree well with the experimental result for a flux limiter of 0.07. The difference in amplitude between the theoretical and experimental observed rate of neutron production or the reduced burn history is believed to be caused by the shell–fuel mix during the deceleration phase due to the Rayleigh–Taylor (RT) instability.[18] Results in Figs. 90.25(a) and 90.25(b) are consistent with the previous results shown in Fig. 90.24(a), where FP calculation gives $\langle f \rangle$ of 0.075. In Fig. 90.25(c), we show the

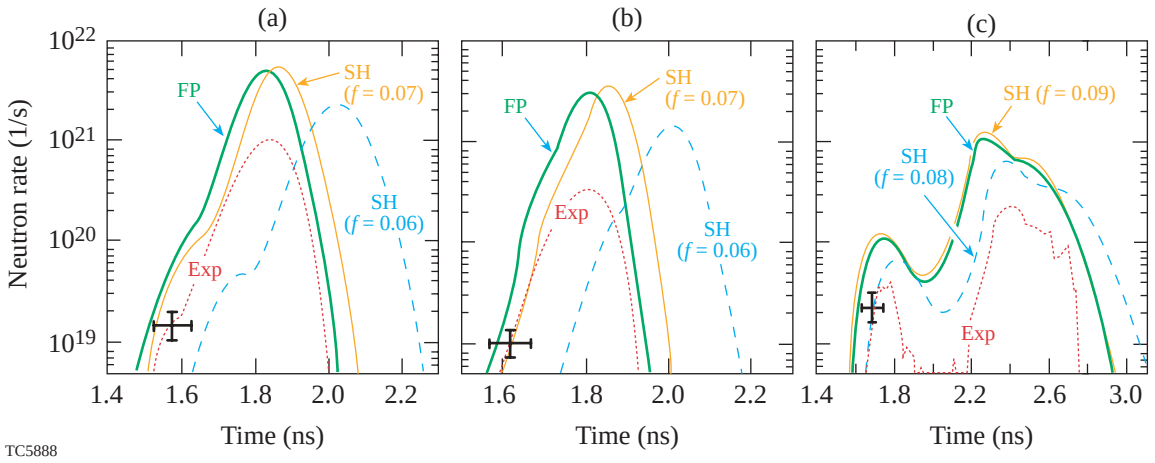

Figure 90.25
Comparison of the calculated neutron rate with results from the experiment for FP and SH with a flux limiter of 0.07 and 0.06: (a) 15 atm of D_2 fuel gas and 1-ns square pulse; (b) 3 atm of D_2 fuel and 1-ns square pulse; (c) 20 atm of DT fuel and 0.4-ns square pulse.

neutron rate for the case of a 0.4-ns square pulse (20 atm of DT in a similar target). In this case, the FP bang time agrees with that of the flux-limited SH for a flux limiter of 0.09. The experimental bang time is between SH with a flux limiter of 0.08 and FP. This indicates that a larger flux limiter is needed for short-pulse cases. In this case, $\langle f \rangle$ was found to be 0.087, which is larger than 0.075 for the 1-ns square pulse. This is consistent with the fact that a large flux-inhibition factor is needed to match the flux-limited SH flux to FP early in the pulse, as shown in Fig. 90.24(a). For all the cases shown in Figs. 90.25(a)–90.25(c), FP gives neutron temporal profiles about 50 ps ahead of these experiments. This discrepancy is within the experimental error bar. A stricter treatment of S_0 and η in Eq. (2) might reduce this discrepancy.

Next, we show the effects of the time dependence of the flux-inhibition factor on the absorption and the stability of the shell during the implosion. Due to the larger flux-inhibition factor early in the pulse, FP gives a larger thermal flux than SH with a flux limiter of 0.07, as shown in Fig. 90.24(a), resulting in a larger electron-density scale length, $L_n = n_e/(\partial n_e/\partial x)$, at the critical surface as seen in Fig. 90.26, where we also show that FP and SH with f = 0.07 give almost the same electron temperature T_e at the critical surface. The larger density scale length of FP at the critical surface early in the pulse gives rise to a larger absorption fraction by inverse bremsstrahlung than in the SH case as shown in Fig. 90.27, where we plot the temporal evolution of the laser absorption calculated by FP and by SH with flux limiters of 0.07 and 0.06. The laser absorption for FP is larger early in the pulse, while later in the pulse, FP gives a lower laser absorption than SH with a flux limiter f of 0.07. The total absorption fraction is 0.83 for FP and 0.76 and 0.68 for SH with f of 0.07 and 0.06, respectively. FP gives a larger laser absorption fraction than that of the SH with 0.07 and 0.06 by about 7% and 15%, respectively.

The effect of the FP transport on the growth of the RT instability during the acceleration phase was investigated using the Betti–Goncharov formula.[20] In the acceleration

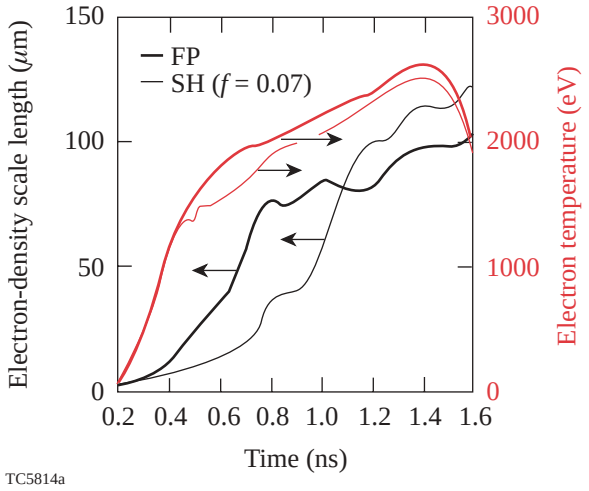

Figure 90.26
L_n and T_e for FP and SH with a flux limiter of 0.07, measured at the critical surface.

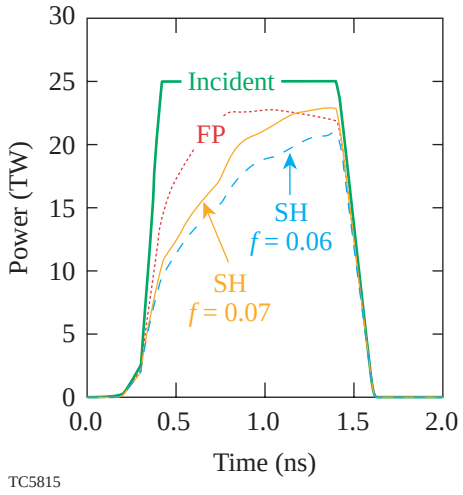

Figure 90.27
The absorbed laser power for FP and SH with flux-limiter values of 0.07 and 0.06. For reference, the incident power is also shown.

phase, the averaged ablation density $\langle \rho_a \rangle$ and the averaged mass ablation rate $\langle \dot{m} \rangle$ are 3.3 g/cm^3 and 1.35×10^6 g/cm^2 s for FP and 3.9 g/cm^3 and 1.53×10^6 g/cm^2 s for SH with a flux limiter of 0.07, respectively. Here, FP gives $\langle \rho_a \rangle$ and $\langle \dot{m} \rangle$ about 15% lower than that for SH. The averaged minimum density-gradient scale length $\langle L_m \rangle$ is 1.47 μm for FP and 1.06 μm for SH. This larger $\langle L_m \rangle$ in FP leads to stabilization of the growth of the RT instability of short-wavelength perturbations during the acceleration phase. The obtained α and β in the Betti–Goncharov formula[20] are 0.90 and 1.5, which are almost the same for both FP and SH.

Conclusion

Flux inhibition for square-pulse CH implosions has been shown to be time dependent. The thermal flux at the critical surface early in the pulse in the FP simulation is larger than in the flux-limited SH with a flux limiter equivalent to the averaged value calculated from the FP calculation. This was confirmed by comparing the neutron burn history from FP simulations with the experimental measurements for different fuel gas pressure and laser pulse durations. A larger flux limiter is required in simulations of implosions driven by shorter-duration pulses. The increase in the density scale length at the critical surface increases the laser absorption. The longer scale length at the ablation region also leads to a slight stabilization of the Rayleigh–Taylor growth by short-wavelength perturbations.

ACKNOWLEDGMENT

One of the authors gratefully thanks Dr. R. P. J. Town, Dr. P. W. McKenty, Dr. V. A. Goncharov, the OMEGA experiments staff of the University of Rochester's Laboratory for Laser Energetics, Prof. H. Takabe and Prof. K. Nishihara of Osaka University. This work was supported by the U.S. Department of Energy Office of Inertial Confinement Fusion under Cooperative Agreement No. DE-FC03-92SF19460, and the New York State Energy Research and Development Authority. The work was also supported by the Japan Society for Promotion of Science.

REFERENCES

1. J. Nuckolls *et al.*, Nature **239**, 139 (1972).
2. R. C. Malone, R. L. McCrory, and R. L. Morse, Phys. Rev. Lett. **34**, 721 (1975).
3. R. L. McCrory, J. M. Soures, C. P. Verdon, P. Audebert, D. Bradley, J. Delettrez, R. Hutchison, S. D. Jacobs, P. Jaanimagi, R. Keck, H. Kim, T. Kessler, J. Knauer, R. Kremens, S. Letzring, F. Marshall, P. McKenty, M. C. Richardson, A. Simon, R. Short, S. Skupsky, and B. Yaakobi, in *High Intensity Laser-Matter Interactions*, edited by E. M. Campbell and H. Baldis (SPIE, Bellingham, WA, 1988), Vol. 913, pp. 40–58.
4. L. Spitzer, Jr. and R. Härm, Phys. Rev. **89**, 977 (1953).
5. D. Shvarts, J. Delettrez, R. L. McCrory, and C. P. Verdon, Phys. Rev. Lett. **47**, 247 (1981).
6. R. J. Mason, Phys. Rev. Lett. **47**, 652 (1981).
7. A. R. Bell, R. G. Evans, and D. J. Nicholas, Phys. Rev. Lett. **46**, 243 (1981).
8. J. P. Matte and J. Virmont, Phys. Rev. Lett. **49**, 1936 (1982).
9. J. R. Albritton, Phys. Rev. Lett. **50**, 2078 (1983).
10. J. P. Matte, T. W. Johnston, J. Delettrez, and R. L. McCrory, Phys. Rev. Lett. **53**, 1461 (1984).
11. A. Nishiguchi *et al.*, Phys. Fluids B **4**, 417 (1992).
12. E. M. Epperlein, Laser Part. Beams **12**, 257 (1994).
13. M. C. Richardson, P. W. McKenty, F. J. Marshall, C. P. Verdon, J. M. Soures, R. L. McCrory, O. Barnouin, R. S. Craxton, J. Delettrez, R. L. Hutchison, P. A. Jaanimagi, R. Keck, T. Kessler, H. Kim, S. A. Letzring, D. M. Roback, W. Seka, S. Skupsky, B. Yaakobi, S. M. Lane, and S. Prussin, in *Laser Interaction and Related Plasma Phenomena*, edited by H. Hora and G. H. Miley (Plenum Publishing, New York, 1986), Vol. 7, pp. 421–448.
14. I. P. Shkarofsky, T. W. Johnston, and M. P. Bachynski, *The Particles Kinetics of The Plasmas* (Addison-Wesley, Reading, MA, 1966).
15. E. M. Epperlein, J. Comput. Phys. **112**, 291 (1994).
16. S. Skupsky, Phys. Rev. A **36**, 5701 (1987).

17. T. R. Boehly, D. L. Brown, R. S. Craxton, R. L. Keck, J. P. Knauer, J. H. Kelly, T. J. Kessler, S. A. Kumpan, S. J. Loucks, S. A. Letzring, F. J. Marshall, R. L. McCrory, S. F. B. Morse, W. Seka, J. M. Soures, and C. P. Verdon, Opt. Commun. **133**, 495 (1997).

18. D. D. Meyerhofer, J. A. Delettrez, R. Epstein, V. Yu. Glebov, V. N. Goncharov, R. L. Keck, R. L. McCrory, P. W. McKenty, F. J. Marshall, P. B. Radha, S. P. Regan, S. Roberts, W. Seka, S. Skupsky, V. A. Smalyuk, C. Sorce, C. Stoeckl, J. M. Soures, R. P. J. Town, B. Yaakobi, J. D. Zuegel, J. Frenje, C. K. Li, R. D. Petrasso, D. G. Hicks, F. H. Séguin, K. Fletcher, S. Padalino, M. R. Freeman, N. Izumi, R. Lerche, T. W. Phillips, and T. C. Sangster, Phys. Plasmas **8**, 2251 (2001).

19. R. A. Lerche, D. W. Phillion, and G. L. Tietbohl, Rev. Sci. Instrum. **66**, 933 (1995).

20. R. Betti, V. N. Goncharov, R. L. McCrory, and C. P. Verdon, Phys. Plasmas **5**, 1446 (1998).

Precision Spectral Sculpting of Broadband FM Pulses Amplified in a Narrowband Medium

Solid-state laser systems envisioned for inertial fusion energy (IFE) applications will require both high efficiency and high single-beam, on-target uniformity. High efficiency is achieved by diode pumping, and on-target uniformity is achieved by beam-smoothing techniques. One of the most-promising gain media for these high-efficiency lasers is ytterbium-doped strontium fluorapatite (Yb^{+3}:SFAP).[1] While this material is ideal for efficient diode pumping, its gain bandwidth is relatively narrow. This has implications for the amount of on-target beam smoothing that can be achieved with techniques such as smoothing by spectral dispersion (SSD),[2] which requires bandwidths of the order of 1 THz in the ultraviolet[3] or roughly 0.333 THz (330 GHz) in the infrared part of the system.[4] Since this bandwidth is comparable to the gain bandwidth of Yb^{+3}:SFAP, significant gain narrowing can be expected in the laser system.

Gain narrowing in this case does more than limit the amount of on-target bandwidth available for beam smoothing. The technique of SSD impresses frequency-modulated (FM) bandwidth on the laser and disperses it with gratings in order to smooth speckle on target. Gain narrowing modifies this FM spectrum, leading to amplitude modulation (AM) or FM-to-AM conversion in the temporal profile of the pulse. The AM occurs primarily at the high-peak-power output of the laser system, significantly increasing the risk of laser damage.

In this article, the application of spectral sculpting to FM pulses is presented. Specifically, spectral sculpting is used to precompensate the effects of gain narrowing in narrowband solid-state amplifiers. The technique of spectral sculpting has previously been used to compensate the effects of gain narrowing in ultrafast amplifiers by spectrally shaping the input pulse prior to amplification[5] or by the use of an intra-amplifier spectral filter.[6] In these examples, the primary goal was to increase the width of the amplified output spectrum. For FM pulses, however, any modification to the original spectrum leads to AM; thus the effects of gain narrowing must be *precisely* compensated to ensure that the amplified output spectrum matches exactly the original, unamplified FM spectrum. We experimentally demonstrate complete gain-narrowing compensation for small-signal, center-line gains of the order of 10^4 and FM bandwidths that are comparable to the linewidth of the amplifying medium.

The concept of spectral sculpting is illustrated in Fig. 90.28. The spectrum of an FM pulse and its corresponding smooth temporal profile are shown in Fig. 90.28(a). As illustrated in Fig. 90.28(b), a spectral mask that attenuates the line-center sidebands, which experience high gain, and wholly transmits the distant low-gain sidebands is applied to the pulse at the input to the laser system. After spectral sculpting, this low-energy input pulse no longer has a purely FM spectrum and is thus heavily amplitude modulated [Fig. 90.28(b)]. As the pulse is amplified through the system, the sculpted spectrum evolves toward a purely FM spectrum. At the output of the

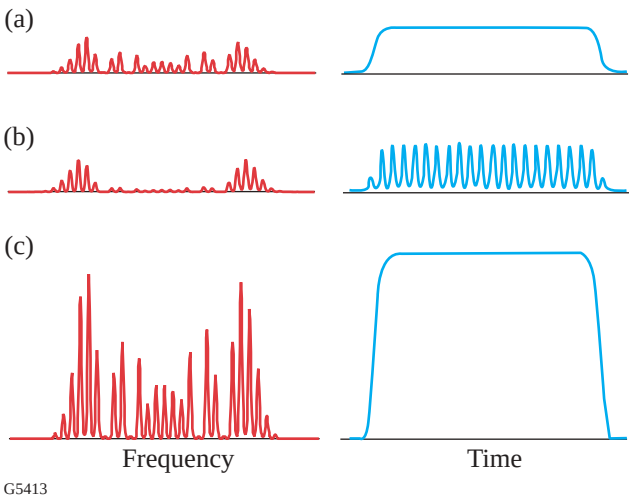

Figure 90.28
(a) Unamplified FM spectrum and associated smooth temporal profile. (b) Sculpted, unamplified FM spectrum. The associated temporal profile shows significant AM. (c) Sculpted, amplified FM spectrum. The amplified output has the original FM spectrum and a smooth temporal profile.

system, precisely where the energy, fluence, and concomitant damage risk are highest, the purely FM spectrum is recovered, with no AM [shown in Fig. 90.28(c)].

A schematic of the experimental setup is shown in Fig. 90.29. The FM bandwidth was generated by double passing a monochromatic, temporally shaped pulse through a $LiNbO_3$ phase modulator.[7] This pulse then entered the spectral sculptor. After sculpting, the pulse was injected into a narrowband, cavity-dumped, multipass Nd:YLF amplifier. Nd:YLF's narrower gain transition serves as a surrogate for the Yb^{+3}:SFAP with a proportional reduction in input bandwidth. The total number of round-trips through the cavity, and thus the overall gain experienced by the pulse, was adjustable. After amplification, the spectral profile of the sculpted, amplified pulse was measured with a custom-built spectrometer with a resolution of ~0.1 Å. To assess the magnitude of post-amplification AM, the temporal profile of these pulses was characterized with an LLE-built streak camera with a 15- to 20-ps temporal resolution.

The design of the spectral sculptor is based on a configuration known as a *zero-dispersion pulse compressor with a pulse-shaping mask*.[8] In this configuration, the sidebands of the FM-modulated incident pulse are first angularly dispersed by a gold-coated diffraction grating. A lens then transforms the angular dispersion of the sidebands into a spatially separated array of individual sidebands located at the back focal (Fourier) plane of the lens. A mask, placed in this plane, performs the actual sculpting. The second half of the sculptor is a mirror image of the first part, producing a spectrally sculpted pulse whose individual FM sidebands are overlapped in space.

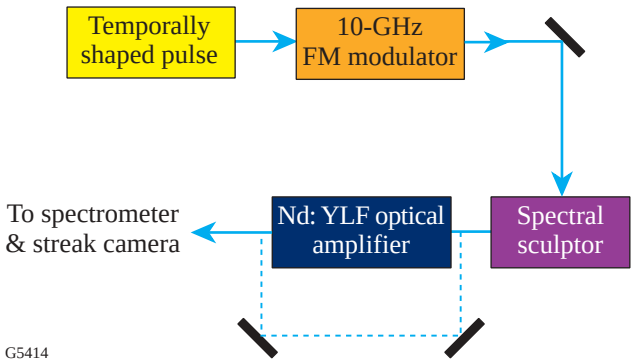

Figure 90.29
Schematic of the spectral sculpting setup.

The specific layout of a particular Fourier-plane mask dictates the optical design of the sculptor. Many types of both fixed and programmable masks might be used to shape the spectrum of a pulse.[9] The programmable mask used here (from Cambridge Research Inc.) is based on the liquid-crystal-modulator (LCM) light valve developed by Wefers and Nelson.[10] The discrete nature of the FM spectrum is ideally suited to this pixelated light valve, and thus our sculptor was designed so that the spatial separation between each sideband in the Fourier plane matched exactly the LCM pixel separation. For a grating groove density of 1740 grooves/mm, a center wavelength of 1.053 μm, an FM sideband spectral separation of 10.384 GHz, and a LCM pixel separation of 100 μm, the required focal length of the lenses was 775 mm. Since the required focal length was so long, each lens in the sculptor was replaced with a three-lens, telephoto system (designed by D. Weiner), resulting in a 60% reduction in the overall length of the sculptor.

The LCM light valve provides control of both the transmission and relative optical phase of each FM sideband. This is done by applying a computer-controlled voltage to each of two liquid crystal layers in each LCM pixel. The sculpting mask can thus be tailored to compensate a variety of conditions in the amplifier. An algorithm was developed that adjusts the transmission of each LCM pixel until the power spectrum of the amplified, sculpted pulse matches a given, desired reference spectrum.

The reference spectrum, which is the original pure FM spectrum generated by the phase modulator, was measured by sending the output of the sculptor, with the transmission of each LCM pixel set to 100%, directly to the spectrometer (see the dashed line in Fig. 90.29). Once the reference spectrum was taken, the unsculpted pulse was then amplified in the Nd:YLF amplifier and sent into the spectrometer. The power spectrum of the amplified pulse is given by

$$\left|E_{\text{amp}}(\nu)\right|^2 = \left|E_{\text{in}}(\nu)\, g(\nu)\right|^2, \tag{1}$$

where $\left|E_{\text{in}}(\nu)\right|^2$ is the spectrum of the unamplified, unsculpted pulse (the reference spectrum) and $\left|g(\nu)\right|^2$ is the gain spectrum of the Nd:YLF amplifier. Given this measurement of the amplified power spectrum, a compensating mask function $M(\nu)$ was then calculated and sent to the LCM. When the LCM is used only as a transmission mask, this mask function can be expressed as

$$M(\nu) = \frac{\left|E_{\text{in}}(\nu)\right|^2}{\left|E_{\text{amp}}(\nu)\right|^2} = \frac{1}{\left|g(\nu)\right|^2}. \quad (2)$$

The now-sculpted pulse was amplified, and the resulting spectrum was again measured and compared to the reference spectrum. This procedure was repeated until the amplified, sculpted spectrum matched the original reference spectrum $\left|E_{\text{in}}(\nu)\right|^2$. This comparison of spectra was accomplished by calculating the relative difference in energy between corresponding sidebands in the reference and amplified spectra. When the rms average difference among all of the sidebands was less than 4%, the spectra were considered to be equivalent and the sculpting procedure ended.

Figure 90.30(a) shows the measured reference FM spectrum, containing ~29 sidebands with a bandwidth of ~220 GHz. Since the spectral width of the Nd:YLF gain curve is approximately two-thirds the width of that of Yb^{+3}:SFAP, we used an FM bandwidth that was two-thirds of that required for a Yb^{+3}:SFAP-based IFE laser system using SSD for beam smoothing. The pulse temporal profile corresponding to the reference spectrum in Fig. 90.30(a), as measured with the streak camera, is shown in Fig. 90.30(b). Without precompensation, as shown in Fig. 90.30(c), the amplified (gross small-signal, center-line gain ~9100) FM pulse spectrum is significantly narrowed. The temporal profile of this gain-narrowed, amplified FM pulse shows nearly 100% AM [Fig. 90.30(d)]. Due to the fact that gain narrowing leads to a symmetric distortion of the original FM spectrum, the predominant frequency of the AM is ~20 GHz, which is twice the phase-modulation frequency.

Beginning with the unsculpted, amplified spectrum in Fig. 90.30(c), the sculpting algorithm iterated, as described above, until the sculpted, amplified spectrum matched the reference spectrum. For gains of $\sim 10^4$, four to five iterations were typically required. The resulting amplified and sculpted spectrum is shown in Fig. 90.30(e). This power spectrum shows that precompensating the effects of gain narrowing produces an amplified spectrum that matches the original unamplified FM power spectrum, thus providing the necessary bandwidth for on-target smoothing. As discussed above, the sculpting technique must also produce amplified pulses with a minimum amount of AM. As can be seen in Fig. 90.30(f), the applied spectral sculpting mask used to generate the spectrum in Fig. 90.30(e) has significantly reduced the AM at the amplifier output; however, some residual 20-GHz AM remains.

To better understand the source of this residual AM, a model that uses the experimentally measured power spectra to calculate the expected temporal pulse profile was developed. These simulations showed that the relative amplitude errors in the sidebands (which were typically of the order of a few percent) were not sufficient to cause the observed residual AM. It was thus concluded that the sculpting algorithm successfully produced the correct amplified FM power spectrum, and that the residual AM was not caused by errors in the sculpted amplitudes of the individual amplified sidebands.

The simulations described above were then expanded to include the effects of errors in the phase relationship among the sidebands that comprise the amplified FM spectra. Two primary sources of phase error in the experiment were material

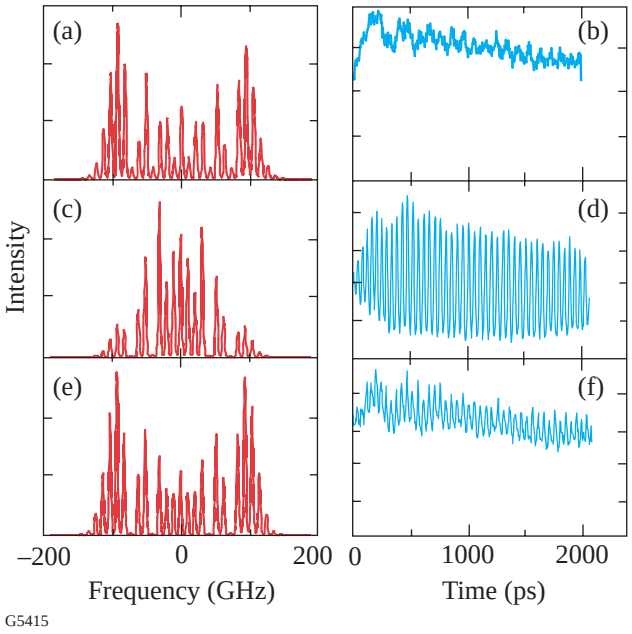

Figure 90.30
(a) Unamplified FM pulse spectrum (reference spectrum); (b) streak camera measurement of the temporal profile of the pulse whose spectrum is shown in (a); (c) gain-narrowed, amplified FM spectrum; (d) temporal profile corresponding to the gain-narrowed spectrum shown in (c); (e) amplified, sculpted FM spectrum; (f) temporal profile corresponding to the amplified, sculpted spectrum shown in (e).

dispersion and imaging errors in the sculptor. These sources primarily produce a spectral phase whose magnitude varies as the square of the frequency difference among the sidebands. Introducing this quadratic spectral phase dependence into our simulations produced FM pulses with amplitude modulation at the fundamental modulation frequency (i.e., 10 GHz). While a small amount of 10-GHz modulation can be observed in our data, the primary residual modulation frequency was 20 GHz.

Another source of spectral phase error in this setup is that associated with the narrowband Nd:YLF gain transition. Assuming that the gain profile of Nd:YLF is Lorentzian in shape, the spectral phase associated with this transition can be expressed as[11]

$$f(w) = \frac{G_{\mathrm{dB}}(w_c)}{8.68} \frac{2(w - w_c)/\Delta w}{1 + \left[2(w - w_c)/\Delta w\right]^2}, \qquad (3)$$

where $G_{\mathrm{dB}}(w_c)$ is the center-line gain in decibels, w_c is the center frequency of the Nd:YLF transition, and Δw is its spectral FWHM. Simulations showed that the addition of a phase function of this form to an FM spectrum, using parameters that matched our experimental conditions, produced 20-GHz temporal modulation with an amplitude similar to that observed in the data.

Using our LCM sculptor, the amplitude mask used to produce the FM spectrum in Fig. 90.30(e) was combined with a phase mask whose functional form is the inverse of the function described by Eq. (3), with the overall gain, transition center frequency, and transition width being adjustable parameters. These parameters were iterated to minimize the amplitude modulation in the streak camera measurements. The resulting experimental temporal profile is shown in Fig. 90.31. Comparing this figure with Fig. 90.30(f), it is clear that by using phase compensation in addition to amplitude shaping, the residual AM in the amplified temporal pulse can be completely eliminated.

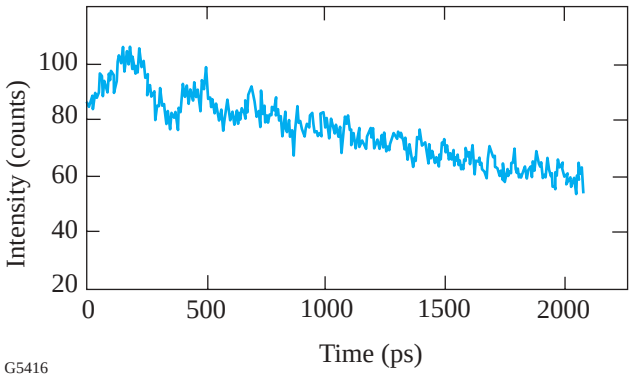

Figure 90.31
Temporal profile of an amplified FM pulse whose spectrum was both phase sculpted and amplitude sculpted.

Conclusion

This article has presented what is believed to be the first demonstration of spectral sculpting applied to the amplification of broadband FM pulses in a narrowband gain medium. Because of FM-to-AM conversion, spectral sculpting for these pulses requires both precision amplitude and phase compensation of narrowband gain effects. Spectral sculpting for narrowband, center-line small-signal gains of 10^4 has been demonstrated, producing amplified pulses that have both sufficient bandwidth for on-target beam smoothing and temporal profiles with no potentially damaging AM.

ACKNOWLEDGMENT

This work was supported by the U.S. Department of Energy Office of Inertial Confinement Fusion under Cooperative Agreement No. DE-FC03-92SF19460, the University of Rochester, and the New York State Energy Research and Development Authority. The support of DOE does not constitute an endorsement by DOE of the views expressed in this article.

REFERENCES

1. C. D. Marshall *et al.*, IEEE J. Quantum Electron. **32**, 650 (1996).
2. S. Skupsky, R. W. Short, T. Kessler, R. S. Craxton, S. Letzring, and J. M. Soures, J. Appl. Phys. **66**, 3456 (1989).
3. J. E. Rothenberg *et al.*, presented at the 1999 Fusion Summer Study Workshop, Snowmass, CO, 12–23 July 1999.
4. D. Eimerl *et al.*, Opt. Lett. **22**, 1208 (1997).
5. F. Verluise *et al.*, Opt. Lett. **25**, 575 (2000).
6. C. P. J. Barty *et al.*, Opt. Lett. **21**, 219 (1996).
7. Laboratory for Laser Energetics LLE Review **78**, 53, NTIS document No. DOE/SF/19460-295 (1999). Copies may be obtained from the National Technical Information Service, Springfield, VA 22161.
8. A. M. Weiner, J. P. Heritage, and E. M. Kirschner, J. Opt. Soc. Am. B **5**, 1563 (1988).
9. A. M. Weiner, Rev. Sci. Instrum. **71**, 1929 (2000).
10. M. M. Wefers and K. A. Nelson, Opt. Lett. **20**, 1047 (1995).
11. A. E. Siegman, *Lasers* (University Science Books, Mill Valley, CA, 1986), p. 283.

Electric-Field-Induced Motion of Polymer Cholesteric Liquid Crystal Flakes in a Moderately Conductive Fluid

Polymer cholesteric liquid crystals (pCLC's) are commonly limited to passive applications as thin films reflecting a specific wavelength and polarization of light due to their inherent selective reflection properties. Some pCLC's in the state above their glass transition temperature can be used for active applications, but due to their high viscosity, switching times are long compared to low-molar-mass liquid crystals with a similar structural composition. New possibilities for pCLC applications emerged in 1994 when Faris proposed fracturing pCLC films with Grandjean texture (the helical axis of the molecular structure is normal to the film surface) into tiny particles called "flakes."[1] Initial research on pCLC flakes, performed by Korenic *et al.*, focused on cyclic polysiloxanes[2] exhibiting selective reflection in the visible. The flaking process was refined, and passive optical effects were studied. By characterizing the selective reflection effect for both films and flakes, Korenic showed that bulk properties were preserved. Colorimetry of pCLC flakes in various drying binders (e.g., glues and adhesives) leads to the development of new paint and pigment concepts for potential applications in both the decorative arts and document security.[3,4] Optimization of the vivid selective reflection effect for passive applications was found to depend on particle concentration, the use of a restricted particle size range (e.g., ~90 to 180 μm), and immersion in a drying binder with comparable refractive index (~1.6).

The use of an electric field to control the motion of particles has been investigated for decades. The prospect of electrophoretic image displays[5] replacing cathode ray tubes was very realistic in the early 1970s until liquid crystal displays took the lead in development. Particle displays remained a novelty until recent advances involving particle encapsulation and the novel concept of a mechanically flexible display that emerged from work with polymer-dispersed liquid crystal technology in the 1980s.[6] An electrophoretic display based on the encapsulation of hundreds of micron-sized charged particles that migrate back and forth inside a 50- to 200-μm capsule is being developed by E-Ink®.[7] A second leading particle display technology, Gyricon®,[8] relies on individually encapsulated bichromal, 25- to 200-μm spheres with oppositely charged hemispheres that rotate with the application of a suitable electric field. Response times for these technologies, currently ~200 to 300 ms, are judged to be sufficient for applications such as electronic books, commercial advertising signs, or personal data assistants (PDA's). Achieving color with these technologies is complex and requires the addition of color filters or the development of multichromal spheres,[9] respectively. A new concept that involves ~10-μm birefringent polymer nematic liquid crystal spheres[10] may also have applications in particle display technology. These spheres were shown to reorient within 100 to 200 μs in an electric field due to the negative dielectric anisotropy of the polymer nematic material. Crossed polarizers would be necessary to observe optical effects.

Here we report an extension of the pCLC flake technology from entirely passive optical applications to an investigation of motion in an electric field.[11,12] Commercial polycyclosiloxane flakes,[13] typically 6 μm thick, with an arbitrary shape and a selective reflection peak at λ_0 = 520 nm (green) were sieved and dried[2] to obtain batches with sizes between 20 and 50 μm [Fig. 90.32(a)]. The pCLC flakes were suspended in propylene carbonate (PC) (Aldrich, 99.7% HPLC grade), a host fluid that is transparent, chemically compatible with the pCLC material, of a comparable density, and has a non-negligible conductivity of ~5×10^{-6} siemens/cm (Table 90.IV). Test cells were constructed using pairs of 25 × 25 × 3-mm indium tin oxide (ITO)-coated glass substrates.[14] A mixture of 41±3-μm-diam soda lime glass spheres (Duke Scientific Corp.) dispersed in a UV-curing epoxy (Masterbond UV 15-7TK1A) was applied in four corners of one substrate to set the cell gap. Cells were then filled by capillary action and sealed with epoxy (Devcon 5-Min®). Basic observations were made using a polarizing microscope (Leitz Orthoplan). A digital camera (Panasonic Digital 5100) with a timer was used to record flake motion with a time resolution of 100 ms. Data on flake motion occurring on a sub-second timescale was obtained by detecting the light reflected from the rotating flake surface using a photomultiplier tube (PMT) (Hamamatsu R905) coupled to the microscope ocular by means of a fiber optic mounted in a precision fiber coupler (Newport Corp.). The PMT signal was displayed

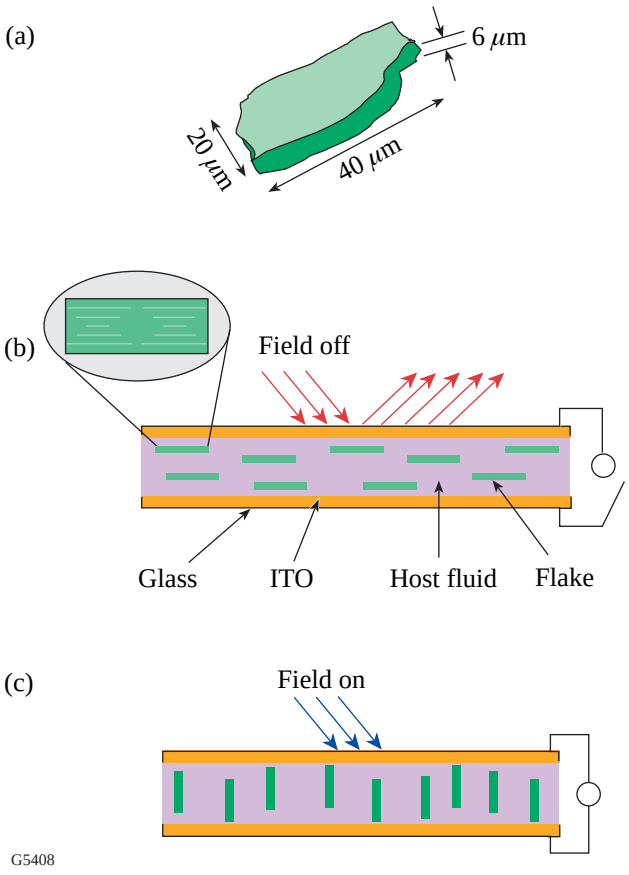

on one channel of an oscilloscope (HP 54520A) and directly compared with the field applied to the cell displayed on the second channel. A function generator (Stanford Research Systems DS345) provided the sinusoidal driving voltage for ac fields. Flake motion was observed as a function of the waveform's magnitude and frequency. Rotational behavior was easily detected under near-normal illumination through a 10× objective (N.A. = 0.2). Brightly reflecting flakes lying in the plane defined by the substrates [Fig. 90.32(b)] darkened substantially after reorienting [Fig. 90.32(c)].

Experiments concentrated on investigating ac sine wave–driven devices. Using the polarizing microscope and the digital camera to track flake motion, we found that pCLC flakes responded to electric fields by rotating approximately

Figure 90.32
Dimensions of a typical irregularly shaped pCLC flake are depicted in (a). Flakes lie approximately parallel to cell substrates when no electric field is applied (b) and appear green due to selective reflection caused by the helical molecular structure of cholesteric liquid crystals, as depicted by the enlarged flake. Flakes reorient with one long axis parallel to the applied field (c). They appear dark since light is no longer reflected off their flat surfaces.

Table 90.IV: Properties of CLC520 flakes and host fluid.

Property at 20°C	Wacker polysiloxanes CLC520	Propylene Carbonate[(d)]
Index of refraction @ 589 nm	1.573* (Ref. 4)	1.422[(c)]
Dielectric permittivity @ 1 kHz	~ 3[(a)]	69[(d)]
dc conductivity (S/cm)	–	$\sim 5 \times 10^{-6}$
Dynamic viscosity (Pa·s)	Solid	2.9×10^{-3}[(c)]
Density (g/cm^3)	~1.1[(b)]	1.189[(c)]

All materials were used as received without further processing.
*Average index of refraction.
[(a)]Measured with an impedance meter (253 Electro Scientific Instruments)
[(b)]Measured by a water displacement technique
[(c)]Sigma-Aldrich-Fluka Catalog (2000)
[(d)]High Purity Solvent Guide, Baxter Diagnostics Inc., Burdick & Jackson Division (1990)

90° about one axis, typically the longest one [Fig. 90.32(c)]. Flake motion was seen in electric fields as low as 5 $mV_{rms}/\mu m$ (0.21 V_{rms}) within a specific frequency bandwidth defined as the range where the flake response time increased by a factor of 3 from the fastest response detected. In a typical set of data for one flake (shown in Fig. 90.33) the flake's fastest response at 5 $mV_{rms}/\mu m$ required 47 s at 130 Hz. The frequency bandwidth extended from 45 Hz to 500 Hz for this very low magnitude field. As the magnitude of the driving field increased to 30 $mV_{rms}/\mu m$, the frequency range for motion broadened to extend from approximately 25 Hz to 1000 Hz. This sixfold increase in voltage greatly reduced the reorientation time for the flake to less than 1 s. Many other flakes were seen to behave in a similar manner.

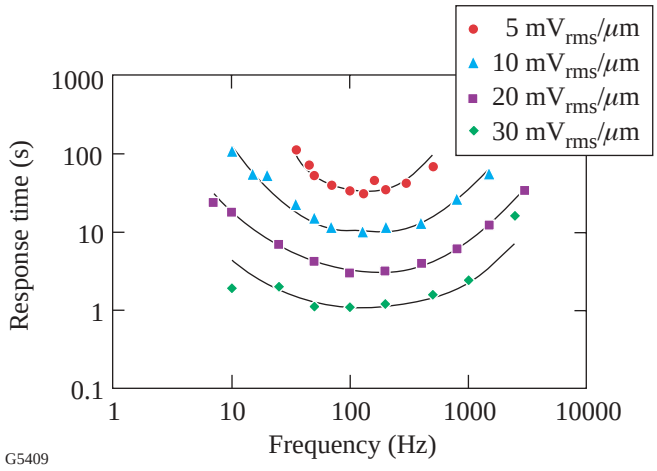

Figure 90.33
The characteristic time response of a representative pCLC flake as a function of frequency at specific electric field values. Lines are drawn to guide the eye. Similar behavior was observed for dozens of flakes.

The reorientation times of flakes in the field of view imaged onto the digital camera (2 mm × 1 mm) were examined as a function of incremental voltage increases of a 50-Hz electric field. Attention was directed to two types of flakes: (1) "small" flakes with the largest dimension of the order of 25 μm (typically square or triangular) and (2) "large" flakes with a 35- to 50-μm dimension that tended to be rectangular. The small flake's response curve in Fig. 90.34 shows an inverse quadratic dependence on the field ($R^2 \approx 0.98$); however, for fields larger than approximately 30 $mV_{rms}/\mu m$ (1.3 V_{rms}) the large flakes consistently reoriented more quickly than the small flakes. Inertial terms are small enough to be neglected in this system, so it is possible that at higher voltages these flakes carried a proportionally larger induced dipole moment due to their size and (typically) rectangular shape, thereby causing these flakes to reorient more quickly than smaller flakes.

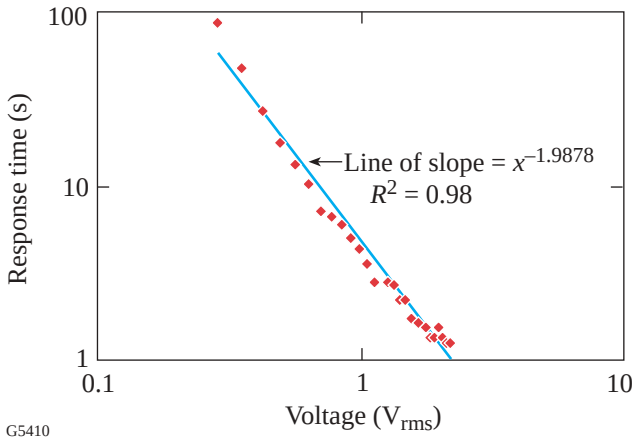

Figure 90.34
The average response time of several flakes has an inverse quadratic dependence on the applied voltage. The standard deviation of 10% is of the order of the size of the data points.

Using the signal from the PMT to detect light reflected from a single typical flake, we found that the actual time necessary for a flake to rotate was less than the reorientation time measured with the digital camera through the microscope eyepiece (Fig. 90.35). In the presence of a 40-$mV_{rms}/\mu m$ (1.7 V_{rms}, 100 Hz) field there was a delay time D_t of 420 ms for the flake to initiate movement after the field was first applied. The flake then completed the full reorientation, as determined by its reflectivity shifting from a maximum to a minimum value, with a fall time R_t of 560 ms. The total reorientation time was therefore just under 1 s. (Here we define the reorientation time of a flake as the sum of the D_t and the R_t). We attribute D_t to the time necessary for an insulating pCLC flake to acquire a dipole moment.

The motion of pCLC flakes was not bistable, but this system showed "memory" or hysteresis. Flakes relaxed to their initial position in the plane of the cell several minutes after the driving field was turned off. There was also a gradual, approximately linear increase in response time for suspended flakes in the PC host for over 48 h.

Electrophoresis can be discounted as a possible mechanism because pCLC flakes are not charged initially, but acquire an

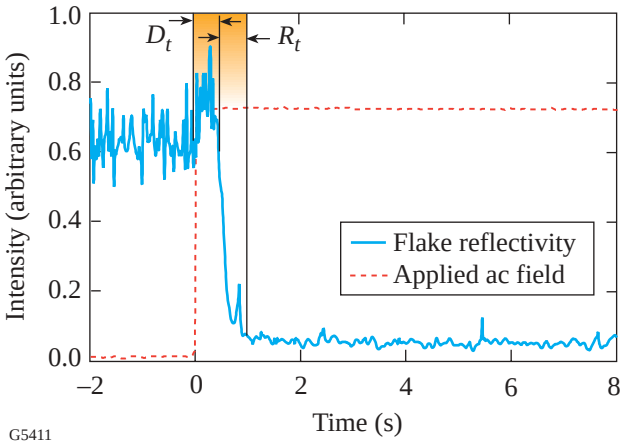

Figure 90.35
Flake motion in a 40-$mV_{rms}/\mu m$ (1.72-V_{rms}) field at 100 Hz was studied with a PMT detecting light reflected from the flake surface. Initially, the flake reflected brightly but little light was detected upon reorientation. The resulting contrast ratio, with no attempt to eliminate light from other flakes and sources of scatter, was approximately 15:1.

induced polarization that is presumed to come from migrating charges. Since the electric fields applied to test cells were uniform to within ±3%, dielectrophoresis, which requires an electric field gradient, can also be eliminated as a possible effect contributing to flake motion. The mechanism leading to flake reorientation in host fluids with non-negligible conductivity is most likely the orientational effect described by Jones.[15] This effect is caused by an induced dipole, with a quadratic dependence on the electric field, brought about by the difference in the conductivity and dielectric constant between the flake and the host fluid. The response time for flake motion is determined by solving the equation of motion for the system, which includes the torques due to the induced dipole and the viscous retardation, while the moment of inertia is neglected. Calculations show that the flake response time will have an inverse quadratic dependence on the electric field, as was experimentally observed. A closed-form solution in two dimensions was obtained, and time response calculations corresponded well with the experimental observations in Fig. 90.33. A numerical solution, based on Okagawa's work,[16] was found for flake motion in three dimensions.

Summary

In summary, we have observed the reorientation of pCLC flakes suspended in propylene carbonate, a moderately conductive host fluid. Flakes align with one axis parallel to the electric field. Motion has been observed in applied fields as low as 5 $mV_{rms}/\mu m$. Reorientation time decreased, while the frequency range for motion increased with the applied voltage. We have observed 90° flake rotation in times R_t as short as hundreds of milliseconds. We envision much faster response times in device geometries where the flake rotation is restricted to a few degrees. The response time, which has a inverse quadratic dependence on the applied field, is also dependent upon flake shape and size as well as various material characteristics. Though flake motion is not bistable, it has a memory effect that needs to be explored further. Controlling flake orientation can lead to both commercial and scientific applications. Display applications with the capability for color are envisioned, as well as optical filters, polarizers, and spatial light modulators.

ACKNOWLEDGMENT

The authors would like to acknowledge Reveo Inc., of Hawthorne, NY; the Center for Electronic Imaging Systems; and the Laboratory for Laser Energetics at the University of Rochester for continuing support. This work was also supported by the U.S. Department of Energy Office of Inertial Confinement Fusion under Cooperative Agreement No. DE-FC03-92SF19460, the University of Rochester, and the New York State Energy Research and Development Authority. The support of DOE does not constitute an endorsement by DOE of the views expressed in this article. Thanks to Prof. T. Jones of the University of Rochester for helpful discussions and to Mr. Brett Klehn and Mr. Kenneth Podolak for help in the laboratory. Finally we thank Dr. L. Li of Kent Optronics, Inc., 275 Martinel Road, Kent, OH 44240 for initially conceiving this idea and for helping in the initial stages of research.

REFERENCES

1. S. M. Faris, U.S. Patent No. 5,364,557 (15 November 1994).
2. E. M. Korenic, S. D. Jacobs, S. M. Faris, and L. Li, Mol. Cryst. Liq. Cryst. **317**, 197 (1998).
3. R. L. van Renesse, in *Optical Document Security*, edited by R. L. van Renesse (Artech House, Boston, 1994), Chap. 13, pp. 263–280.
4. E. M. Korenic, "Colorimetry of Cholesteric Liquid Crystals (Polysiloxane, Polarizing Paints)," Ph.D. thesis, University of Rochester, 1997.
5. I. Ota, J. Ohnishi, and M. Yoshiyama, Proc. IEEE **61**, 832 (1973).
6. J. L. Fergason, in *1985 SID International Symposium, Digest of Technical Papers*, edited by J. Morreale (Pallisades Inst. Res. Services, New York, 1985), pp. 68–70.
7. B. Comiskey *et al.*, Nature **394**, 253 (1998).
8. N. K. Sheridon *et al.*, J. Soc. Inf. Disp. **7**, 141 (1999).
9. N. K. Sheridon and G. G. Robertson, U.S. Patent No. 5,767,826 (16 June 1998).

10. D. R. Cairns, M. Sibulkin, and G. P. Crawford, Appl. Phys. Lett. **78**, 2643 (2001).

11. L. Li, Reveo, Inc., private communication (1998).

12. K. L. Marshall, T. Z. Kosc, S. D. Jacobs, S. M. Faris, and L. Li, World Patent No. WO 01/88607 A1 (22 November 2001); T. Z. Kosc, K. L. Marshall, S. D. Jacobs, and B. Klehn, presented at the Novel Optical Materials and Applications Meeting, Cetraro, Italy, 20–27 May 2001.

13. Wacker-Chemie, Consortium für Electrochemische Industrie GmbH, Zielstattstrasse 20, D-81379 München, Germany.

14. Thin Film Devices, Inc., Anaheim, CA 92807. The ITO is sputter coated 750 Å thick onto a soda lime float glass substrate with a rms surface roughness of 3 to 4 Å (Zygo NewView™ 5000, 20× Mirau, areal over 250 μm × 350 μm; Zygo Corporation, Middlefield, CT 06455). It has a resistivity of 100 Ω/sq and <88% transmission in the visible.

15. T. B. Jones, *Electromechanics of Particles* (Cambridge University Press, New York, 1995).

16. A. Okagawa, R. G. Cox, and S. G. Mason, J. Colloid Interface Sci. **47**, 536 (1974).

Femtosecond Response of a Freestanding LT-GaAs Photoconductive Switch

The use of semiconductor photoconductive devices to generate picosecond and subpicosecond electrical signals has been the subject of intense research for the last two decades, primarily motivated by the fast-growing demand for ultrafast, integrated optoelectronic photoswitches and photodetectors. Photoconductive devices based on ion-implanted InP,[1,2] ion-implanted silicon-on-sapphire,[3] amorphous silicon, low-temperature-grown GaAs (LT-GaAs),[4–7] as well as metal-semiconductor-metal diodes,[8] have been studied thoroughly. Unfortunately, due to either their nonstandard active material or the need for nanolithography, it is difficult to integrate any of the above devices into advanced optoelectronic systems or high-performance digital electronics circuits (conventional or superconducting) fabricated on Si substrates. The existing semiconductor photoswitches usually require hybrid integration, which drastically reduces their intrinsic multigigahertz bandwidth.

This article reports on a new method of making a freestanding LT-GaAs photoconductive switch that can be placed at virtually any point on any circuit containing a coplanar strip (CPS) transmission structure. Our device is characterized by <0.5-ps response time and ~23-V/W responsivity (typical for Si or GaAs photodetectors) for 810-nm radiation.

The fabricating process of freestanding LT-GaAs photoconductive devices is described in detail elsewhere.[9] Briefly, 1-μm-thick LT-GaAs films were grown by molecular beam epitaxy on semi-insulating GaAs substrates covered with a layer of AlAs, at a temperature range of 200°C to 250°C and at a growth rate of 1 μm/h.[10] The 0.5-μm-thick AlAs etch-stop interlayer was grown first to enable the separation of the LT-GaAs film from the substrate. After the growth, wafers with LT-GaAs layers were annealed *in situ* at 600°C for 10 min under local As overpressure.

The multiple-step process was used to lift and transfer the LT-GaAs layer from the GaAs substrate.[9–11] First, LT-GaAs was covered with a photoresist, and the photoswitch structures, approximately 5 μm wide and 15 μm long, were defined by photolithography. Next, the wafer was placed into the diluted HF solution ($HF:H_2O = 1:9$) for selective AlAs etching, which led to separation of the LT-GaAs film from the substrate. The separated LT-GaAs switch was then placed gently on a predetermined spot on the Si substrate. Special care was taken to ensure that the contacting surfaces were exceptionally clean so the LT-GaAs would adhere to the Si through molecular bonding. In the final step, the 10-nm/300-nm-thick, Ti/Au CPS lines were fabricated on top of the switch, resulting in the structure shown in the inset in Fig. 90.36. The final two steps could be easily reversed, i.e., in many fabrication runs the Ti/Au CPS lines were fabricated first, and the switch was placed on top of them, again attached by molecular forces.

The femtosecond response of our LT-GaAs photoconductive switches was measured with an electro-optic (EO) sampling system,[12] using a $LiTaO_3$ total-internal-reflection (TIR) probe,[4,13,14] as shown in Fig. 90.36. The TIR configuration allowed us to position the excitation and sampling spots only ~10 μm away, eliminating the signal distortion caused by propagation effects and enabling the measurement of close-to-intrinsic electrical transients. A commercial Ti:sapphire laser with a repetition rate of 82 MHz was used to generate 110-fs-wide, 810-nm-wavelength optical pulses. Both the excitation and sampling beams were focused to ~5-μm spots with a single 10×, long-focal-length microscope objective. The same objective also collected the sampling beam reflected by the TIR probe.[4,13,14]

The time-resolved photoresponse signals of our freestanding LT-GaAs photoconductive switch, dc biased at 30 V and illuminated by the average optical excitation power P_{ex} of 2.7 mW, 3.2 mW, 3.9 mW, and 4.6 mW, respectively, are shown in Fig. 90.37. The transient amplitudes were normalized to demonstrate that although measurements for each P_{ex} were optimized separately, the response was very reproducible, with a 470-fs full-width-at-half-maximum (FWHM) pulse width, a rise time (10% to 90%) of 340 fs, and a fall time (90% to 10%) of 460 fs. Small ripples on top of the ~5-ps-long shoulder after the main peak were also present in each measurement.

Following Ref. 14, we believe that these ripples were caused by electrical signal reflections of the interfaces of our >50-μm-thick $LiTaO_3$ crystal at the bottom of the TIR probe. The latter was confirmed by measuring the transients when the sampling spot was moved ~100 μm. In this case, the measured pulse was broadened to a FWHM of 1.1 ps (due to the CPS dispersion), and post-pulse ripples were shifted in time with the respect of main pulse.

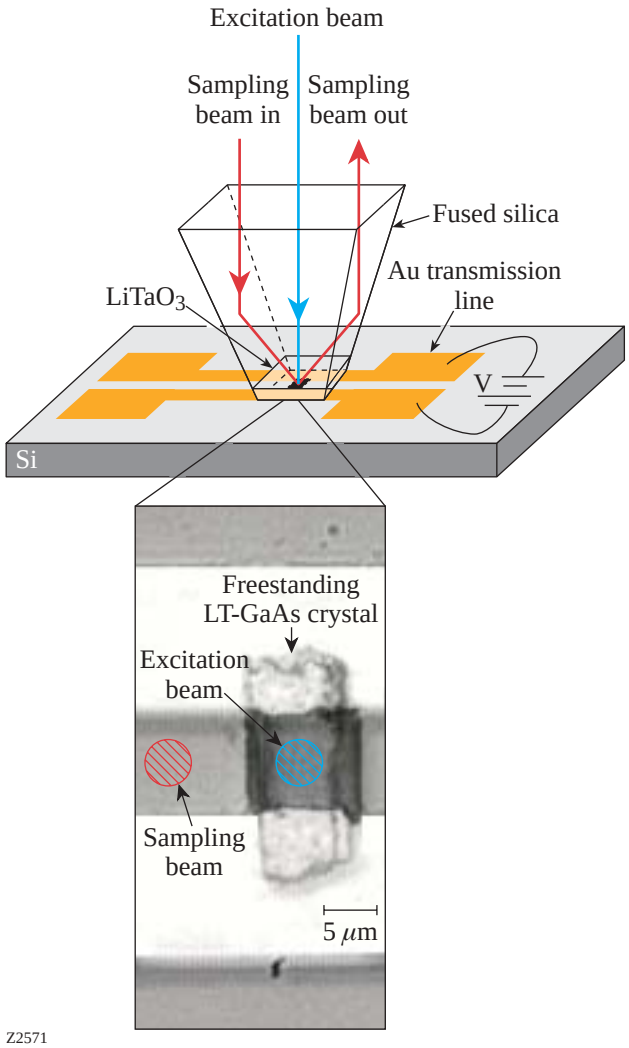

Figure 90.36
Schematics of the electro-optic TIR probe placed on top of the Au CPS line fabricated on a Si wafer (the figure is not to scale). The inset shows the micrograph of an actual LT-GaAs freestanding switch and the positions of the excitation and sampling beams.

The electrical transient generated by the photoconductive device results from the temporary increase of conductivity due to photogenerated free carriers in the illuminated region of the semiconductor. The signal's intrinsic rise time is limited by how fast the optical energy is delivered, which corresponds to the integral of the laser pulse (in our case, ~120 fs). Our measured, 340-fs rise time is broadened by the EO system time response τ_s, which includes such factors as the finite spot size of the sampling beam, the thickness of the $LiTaO_3$ crystal, and the equivalent lumped-element circuit parameters.[7] The value of τ_s can be estimated as

$$\tau_s = \sqrt{340^2 - 120^2} \approx 320 \text{ fs}.$$

Owing to the existence of a very large concentration of deep-level traps in LT-GaAs, which originated in the fabrication procedure, the signal's fall time is limited by the free-carrier lifetime. Knowing that the measured fall time is 460 fs and taking into account τ_s, we can derive the carrier lifetime as

$$\tau = \sqrt{460^2 - 320^2} \approx 330 \text{ fs}.$$

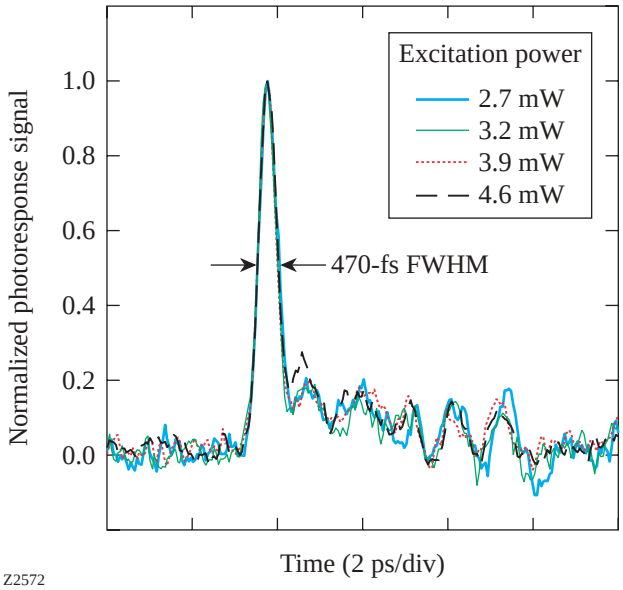

Figure 90.37
A 470-fs FWHM electrical photoresponse of our freestanding LT-GaAs photoconductive switch biased at 30 V and excited by 810-nm radiation, for several values of the optical excitation power. The optical power was measured at the sample plane, including all the optics and the TIR probe.

This latter value fits very well with the literature data on LT-GaAs, measured using the EO systems, e.g., $\tau < 400$ fs reported by Gupta *et al.*[6] We note that the all-optical, pump/probe experiments tend to give much shorter, $\tau \approx 150$ fs, values.[15] We must remember, however, that for all-optical experiments, the probe beam tests dynamics of very hot carriers, at much higher optical frequencies, as compared to the voltage response, measured by the EO sampling.

Figure 90.38 shows the dependence of the photoresponse amplitude on P_{ex} when the bias voltage V_b was set at 30 V. We observe a linear dependence for moderate P_{ex} values with a slope of ~23 V/W, which can be interpreted as the voltage responsivity of our photoconductive device. For $P_{ex} > 4.5$ mW, the signal amplitude saturates. The photoresponse amplitude versus V_b, measured at P_{ex} = 4.6 mW, is also linear (inset in Fig. 90.38), with a few volts offset at low biases, apparently, due to nonohmic contacts at the Au/LT–GaAs interface.

The photoswitch behavior presented in Fig. 90.38 is expected. With no light incident on the device, the resistance of the LT-GaAs bar is above 40 MΩ; thus, we can safely assume

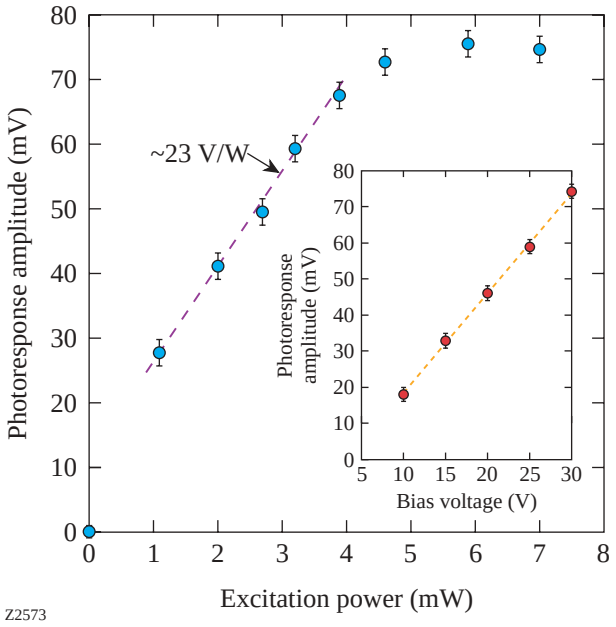

Figure 90.38
The amplitude of the photoresponse signal as a function of P_{ex} for the fixed, 30-V switch bias. The inset shows the signal amplitude versus the bias voltage for P_{ex} = 4.6 mW.

that the measured signal is entirely due to photogenerated carriers inside our 1-μm-thick sample (optical penetration depth of 810-nm photons is 0.86 μm). The background signal recovered to 0 V after each pulse, which indicated that the underlying Si substrate with its long recombination time was not being excited. With the gradual increase of P_{ex}, more and more electron-hole pairs are generated, increasing conductivity and leading to the proportional increase of the electrical response. Above a certain excitation level, however, all available carriers (for a given photon energy) are excited, so the further increase in P_{ex} does not produce more carriers and the signal reaches saturation. Similarly, for a given P_{ex}, the increase of the switch V_b leads to the linear (due to the Ohm's law) increase of the amplitude of the photocurrent.

To provide more quantitative interpretation and to check if our experimental data are consistent with theoretical predictions, we calculated the amplitude of the photocurrent pulse generated in our experiment as $I_s = V_s/Z_0$, where V_s is the voltage pulse amplitude and $Z_0 = 30\,\Omega$ is the CPS characteristic impedance. For P_{ex} = 3.9 mW, the measured V_s is 70 mW, leading to I_s = 2.33 mA. Taking into account that the signal FWHM is 470 fs, the total number of carriers involved in the transient photocurrent pulse is $N \approx 7 \times 10^3$. This value can be inserted into the theoretical formula,[7] which returns the number of carriers generated in a semiconductor by a laser pulse and collected by the photoswitch electrodes, to see if the measured data is consistent with reasonable values of the quantum efficiency:

$$N = \eta(1-R)E_0[1-\exp(-\alpha d)]\frac{1}{\hbar\omega}\mu\tau\frac{V_b}{l^2}, \qquad (1)$$

where η is the quantum efficiency, R is the reflectivity, E_0 is the laser energy per pulse of $\hbar\omega$ photons impinging on the LT-GaAs layer, α is the optical absorption coefficient at the excitation wavelength, d is the thickness, μ is the mobility of the LT-GaAs layer, and l is the spacing between the CPS electrodes. Substituting into Eq. (1) parameters relevant for our experimental situation, namely, E_0 = 68 pJ (corresponding to P_{ex} = 3.9 mV), V_b = 30 V, l = 10 μm, α (810 nm) = 1.16 μm^{-1}, d = 1 μm, τ = 330 fs, and estimating $R \approx 0.4$ and $\mu \approx 100$ cm^2/V-s, we finally obtain $\eta \approx 0.1$. We also note that Eq. (1) predicts experimentally observed (Fig. 90.38) linear dependences for both P_{ex} ($P_{ex} \sim E_0$) and V_b. For P_{ex} = 4.6 mW, the number of photogenerated carriers corresponds to a total carrier density of ~10^{18} cm^{-3}, which is a reasonable value for LT-GaAs near the saturation (see Fig. 90.38).

Conclusion

In conclusion, a freestanding LT-GaAs photoconductive device has been successfully fabricated and demonstrated to have a femtosecond time resolution, voltage responsivity of ~23V/W, and a quantum efficiency of the order of 10%. The time-resolved, 470-fs FWHM of our pulses corresponds to ~640-GHz, 3-dB bandwidth for the photodetector. For moderate P_{ex} and V_b, the photoresponse signal was found to increase linearly, in very good agreement with theoretical predictions. The LT-GaAs excess carrier lifetime was measured to be 330 fs, in agreement with the literature data. The freestanding photoswitch is best suited for hybrid optoelectronic and ultrafast electronic systems since it can be placed at virtually any point on the test circuit.

ACKNOWLEDGMENT

We thank Jianliang Li, Carlo Williams, and Guillaume Sabouret for stimulating discussions and Brandon Jasionowski for his technical assistance. This work was supported by the NSF grant INT-0078949, the ONR grant N00014-02-1-0026 and by Corning Inc.

REFERENCES

1. A. G. Foyt, F. J. Loeonberger, and R. C. Williamson, Appl. Phys. Lett. **40**, 447 (1982).
2. P. M. Downey and B. Schwartz, Appl. Phys. Lett. **44**, 207 (1984).
3. M. B. Ketchen *et al.*, Appl. Phys. Lett. **48**, 751 (1986).
4. U. D. Keil and D. R. Dykaar, Appl. Phys. Lett. **61**, 1504 (1992); D. H. Auston, in *Picosecond Optoelectronic Devices*, edited by C. H. Lee (Academic Press, Orlando, 1984), pp. 73–117.
5. F. W. Smith *et al.*, Appl. Phys. Lett. **54**, 890 (1989).
6. S. Gupta *et al.*, Appl. Phys. Lett. **59**, 3276 (1991).
7. S. Gupta, J. F. Whitaker, and G. A. Mourou, IEEE J. Quantum Electron. **28**, 2464 (1992).
8. M. Y. Liu, S. Y. Chou, T. Y. Hsiang, S. Alexandrou, and R. Sobolewski, J. Vac. Sci. Technol. B **10**, 2932 (1992); C.-C. Wang, S. Alexandrou, D. Jacobs-Perkins, and T. Y. Hsiang, Appl. Phys. Lett. **64**, 3578 (1994).
9. R. Adam, M. Mikulics, M. Siegel, P. Kordos, X. Zheng, Y. Xu, and R. Sobolewski, "Fabrication and Optical Response of LT-GaAs Freestanding Photoconductive Devices," in preparation.
10. P. Kordos *et al.*, Appl. Phys. Lett. **71**, 1118 (1997); P. Kordos *et al.*, Electron. Lett. **34**, 119 (1998).
11. A. Sasaki *et al.*, J. Electrochem. Soc. **146**, 710 (1999).
12. J. A. Valdmanis and G. Mourou, IEEE J. Quantum Electron. **QE-22**, 69 (1986).
13. S. Alexandrou, R. Sobolewski, and T. Y. Hsiang, IEEE J. Quantum Electron. **28**, 2325 (1992).
14. M. Y. Frankel *et al.*, IEEE Microw. Guid. Wave Lett. **1**, 60 (1991).
15. M. Mikulics, M. Marso, R. Adam, A. Fox, D. Buca, A. Förster, P. Kordos, Y. Xu, and R. Sobolewski, in *2001 International Symposium on Electron Devices for Microwave and Optoelectronic Applications* (IEEE, Piscataway, NJ, 2001), pp. 155–159.

Publications and Conference Presentations

Publications

H.-M. P. Chen, S. W. Culligan, Y. H. Geng, D. Katsis, and S. H. Chen, "Photoresponsive Glassy Liquid Crystals for Tunable Reflective Coloration," Polymer Preprints **43**, 145 (2002).

T. J. B. Collins and S. Skupsky, "Imprint Reduction Using an Intensity Spike in OMEGA Cryogenic Targets," Phys. Plasmas **9**, 275 (2002).

W. R. Donaldson, J. H. Kelly, R. L. Keck, and R. Boni, "Predicting and Measuring Optical Pulse Shapes on the OMEGA Laser System," in OSA *Trends in Optics and Photonics (TOPS) Vol. 56, Conference on Lasers and Electro-Optics (CLEO 2001)* (Optical Society of America, Washington, DC, 2001), pp. 158–159.

Y. Geng, D. Katsis, S. W. Culligan, J. J. Ou, S. H. Chen, and L. J. Rothberg, "Fully Spiro-Configured Terfluorenes as Novel Amorphous Materials Emitting Blue Light," Chem. Mater. **14**, 463 (2002).

G. Gol'tsman, O. Okunev, G. Chulkova, A. Lipatov, A. Dzardanov, K. Smirnov, A. Semenov, B. Voronov, C. Williams, and R. Sobolewski, "Fabrication and Properties of an Ultrafast NbN Hot-Electron Single-Photon Detector," IEEE Trans. Appl. Supercond. **11**, 574 (2001).

V. N. Goncharov, "Analytical Model of Nonlinear, Single-Mode, Classical Rayleigh–Taylor Instability at Arbitrary Atwood Numbers," Phys. Rev. Lett. **88**, 134502 (2002).

M. J. Guardalben, A. Babushkin, R. S. Craxton, R. L. Keck, W. R. Donaldson, and K. A. Thorp, "Obtaining UV Energy Balance with 1-THz Spectral Bandwidth on the 60-Beam OMEGA Laser," in OSA *Trends in Optics and Photonics (TOPS) Vol. 56, Conference on Lasers and Electro-Optics (CLEO 2001)* (Optical Society of America, Washington, DC, 2001), p. 157.

M. J. Guardalben, L. Ning, N. Jain, D. J. Battaglia, and K. L. Marshall, "Experimental Comparison of a Liquid-Crystal Point-Diffraction Interferometer (LCPDI) and a Commercial Phase-Shifting Interferometer and Methods to Improve LCPDI Accuracy," Appl. Opt. **41**, 1353 (2002).

D. Katsis, Y. H. Geng, J. J. Ou, S. W. Culligan, A. Trajkovska, S. H. Chen, and L. J. Rothberg, "Spiro-Linked Ter-, Penta-, and Heptafluorenes as Novel Amorphous Materials for Blue Light Emission," Chem. Mater. **14**, 1332 (2002).

D. Katsis, Y. H. Geng, J. J. Ou, S. W. Culligan, A. Trajkovska, S. H. Chen, and L. J. Rothberg, "Spiro-Linked Ter- and Pentafluorenes for Stable and Efficient Blue Emission," Polymer Preprints **43**, 118 (2002).

J. M. Larkin, W. R. Donaldson, R. S. Knox, and T. H. Foster, "Reverse Intersystem Crossing in Rose Bengal. II. Fluence Dependence of Fluorescence Following 532-nm Laser Excitation," Photobiochem. Photobiophys. **75**, 221 (2002).

J. A. Marozas, "Self- and Cross-Phase Modulation of High-Intensity Laser Beams Emerging from a Diamond-Turned KDP Wedge," J. Opt. Soc. Am. B **19**, 75 (2002).

J. A. Marozas, S. P. Regan, J. H. Kelly, D. D. Meyerhofer, W. Seka, and S. Skupsky, "Laser Beam Smoothing Caused by the Small-Spatial-Scale *B*-Integral," J. Opt. Soc. Am. B **19**, 7 (2002).

R. Sobolewski, Y. Xu, X. Zheng, C. Williams, J. Zhang, A. Verevkin, G. Chulkova, A. Korneev, A. Lipatov, O. Okunev, K. Smirnov, and G. N. Gol'tsman, "Spectral Sensitivity of the NbN Single-Photon Superconducting Detector," IEICE Trans. Electron. **E85-C**, 797 (2002).

C. Williams, G. Sabouret, and R. Sobolewski, "Experiments and Simulations of Electrical Pulse Modulation of Y-Ba-Cu-O Thin Films," IEICE Trans. Electron. **E85-C**, 733 (2002).

C. Williams, Y. Xu, R. Adam, M. Darula, O. Harnack, J. Scherbel, M. Siegel, F. A. Hegmann, and R. Sobolewski, "Ultrafast YBCO Photodetector Based on the Kinetic-Inductive Process," IEEE Trans. Appl. Supercond. **11**, 578 (2001).

Forthcoming Publications

A. Babushkin, M. J. Harvey, and M. D. Skeldon, "The Output Signal-to-Noise Ratio of a Nd:YLF Regenerative Amplifier," to be published in Applied Optics.

R. Betti, K. Anderson, V. N. Goncharov, R. L. McCrory, D. D. Meyerhofer, S. Skupsky, and R. P. J. Town, "Deceleration Phase of Inertial Confinement Fusion Implosions" to be published in Physics of Plasmas.

T. R. Boehly, T. J. B. Collins, O. Gotchev, T. J. Kessler, J. P. Knauer, T. C. Sangster, and D. D. Meyerhofer, "Observations of Modulated Shock Waves in Solid Targets Driven by Spatially Modulated Laser Beams," to be published in the Journal of Applied Physics.

H. Brunnader, W. T. Shmayda, D. R. Harding, L. D. Lund, and R. Janezic, "Advanced Tritium Recovery System," to be published in Fusion Science and Technology.

Y. Cao, H. Li, J. A. Szpunur, and W. T. Shmayda, "Effects of Textures on Hydrogen Diffusion in Nickel," to be published in Materials Science Forum.

W. R. Donaldson, R. Boni, R. L. Keck, and P. A. Jaanimagi, "A Self-Calibrating, Multichannel Streak Camera for Inertial Confinement Fusion Applications," to be published in the Review of Scientific Instruments.

R. Epstein, J. A. Delettrez, V. Yu. Glebov, V. N. Goncharov, P. W. McKenty, P. B. Radha, S. Skupsky, V. A. Smalyuk, and C. Stoeckl, "One-Dimensional Simulation of the Effects of Unstable Mix on Neutron and Charged-Particle Yield from Laser-Driven Implosion Experiments," to be published in Lasers and Particle Beams.

Y. Geng, A. Trajkovska, D. Katsis, J. J. Ou, S. W. Culligan, and S. H. Chen, "Synthesis, Characterization, and Optical Properties of Monodisperse Chiral Oligofluorenes," to be published in the Journal of the American Chemical Society.

T. Z. Kosc, K. L. Marshall, S. D. Jacobs, J. C. Lambropoulos, and S. Faris, "Electric-Field-Induced Motion of Polymer Cholesteric Liquid Crystal Flakes in a Moderately Conductive Fluid," to be published in Applied Optics.

M. V. Kozlov and C. J. McKinstrie, "Sound Waves in One-Ion Plasmas," to be published in Physics of Plasmas.

M. V. Kozlov and C. J. McKinstrie, "Sound Waves in Two-Ion Plasmas," to be published in Physics of Plasmas.

J. A. Marozas and J. D. Zuegel, "The Smoothing Performance of Ultrafast Pickets on the NIF," to be published in the Journal of the Optical Society of America B.

A. V. Okishev, D. Battaglia, I. Begishev, and J. D. Zuegel, "All-Solid-State, Diode-Pumped Regenerative Amplifier for the OMEGA Laser System," to be published in OSA Trends in Optics and Photonics (TOPS), Conference on Lasers and Electro-Optics, OSA Technical Digest.

P. B. Radha, J. A. Delettrez, R. Epstein, V. Yu. Glebov, R. L. Keck, R. L. McCrory, P. W. McKenty, F. J. Marshall, S. P. Regan, S. Roberts, T. C. Sangster, W. Seka, S. Skupsky, V. A. Smalyuk, C. Sorce, C. Stoeckl, J. M. Soures, R. P. J. Town, B. Yaakobi, J. A. Frenje, C. K. Li, R. D. Petrasso, F. H. Séguin, K. Fletcher, S. Padalino, C. Freeman, N. Izumi. R. Lerche, and T. W. Phillips, "Inference of Mix in Direct-Drive Implosions on OMEGA," to be published in Physics of Plasmas.

S. P. Regan, J. A. Delettrez, P. A. Jaanimagi, B. Yaakobi, V. A. Smalyuk, F. J. Marshall, D. D. Meyerhofer, W. Seka, D. A. Haynes, Jr., and C. F. Hooper, Jr., "Characterization of Direct-Drive-Implosion Core Conditions on OMEGA with Time-Resolved Ar *K*-Shell Spectroscopy," to be published in Physics of Plasmas.

F. H. Séguin, C. K. Li, D. G. Hicks, J. A. Frenje, R. D. Petrasso, J. M. Soures, V. Yu. Glebov, C. Stoeckl, P. B. Radha, D. D. Meyerhofer, S. Roberts, C. Sorce, T. C. Sangster, and M. D. Cable, "Diagnostic Use of Secondary D^3He Proton Spectra for DD OMEGA Targets," to be published in Physics of Plasmas.

W. Seka, H. A. Baldis, J. Fuchs, S. P. Regan, D. D. Meyerhofer, C. Stoeckl, B. Yaakobi, R. S. Craxton, and R. W. Short, "Multibeam Stimulated Brillouin Scattering from Hot Solid-Target Plasmas," to be published in Physical Review Letters.

A. D. Semenov, G. N. Gol'tsman, and R. Sobolewski, "Hot-Electron Effect in Superconductors and Its Applications for Radiation Sensors," to be published in Superconductor Science & Technology.

C. R. Shmayda, W. T. Shmayda, and N. P. Kherani, "Monitoring Tritium Activity on Surfaces: Recent Developments," to be published in Fusion Science and Technology.

W. T. Shmayda, A. Bruggeman, J. Braet, and S. Vanderbiesen, "Treatment of Tritiated Solvents," to be published in Fusion Science and Technology.

W. T. Shmayda and R. D. Gallagher, "Recovery of Tritium from Pharmaceutical Mixed Waste Liquids," to be published in Fusion Science and Technology.

W. T. Shmayda, S. Zukotynski, D. Yeghikyan, and F. Gaspari, "Properties of Amorphous Carbon Films," to be published in Fusion Science and Technology.

R. W. Short and A. Simon, "Damping of Perturbations in Weakly Collisional Plasmas," to be published in Physics of Plasmas.

M. D. Skeldon, "An Optical-Pulse-Shaping System Based on an Electro-Optic Modulator Driven by an Aperture-Coupled-Stripline Electrical-Waveform Generator," to be published in the Journal of the Optical Society of America B.

V. A. Smalyuk, J. A. Delettrez, V. N. Goncharov, F. J. Marshall, D. D. Meyerhofer, S. P. Regan, T. C. Sangster, and B. Yaakobi, "Rayleigh–Taylor Instability in the Deceleration Phase of Spherical Implosion Experiments," to be published in Physics of Plasmas.

C. Stoeckl, C. Chiritescu, J. A. Delettrez, R. Epstein, V. Yu. Glebov, D. R. Harding, R. L. Keck, S. J. Loucks, L. D. Lund, R. L. McCrory, P. W. McKenty, F. J. Marshall, D. D. Meyerhofer, S. F. B. Morse, S. P. Regan, P. B. Radha, S. Roberts, T. C. Sangster, W. Seka, S. Skupsky, V. A. Smalyuk, C. Sorce, J. M. Soures, R. P. J. Town, J. A. Frenje, C. K. Li, R. D. Petrasso, F. H. Séguin, K. Fletcher, S. Padalino, C. Freeman, N. Izumi, R. Lerche, and T. W. Phillips, "First Results from Cryogenic Target Implosions on OMEGA," to be published in Physics of Plasmas.

A. Sunahara, J. A. Delettrez, C. Stoeckl, R. W. Short, and S. Skupsky, "Time-Dependent Electron-Thermal-Flux Inhibition in Direct-Drive Laser Implosions," to be published in Physical Review Letters.

R. P. J. Town, V. N. Goncharov, P. W. McKenty, J. A. Delettrez, R. Epstein, R. L. McCrory, P. B. Radha, S. Skupsky, V. Yu. Glebov, D. R. Harding, D. D. Meyerhofer, F. J. Marshall, S. P. Regan, W. Seka, V. A. Smalyuk, C. Stoeckl, J. M. Soures, B. Yaakobi, and J. D. Zuegel, "OMEGA Direct-Drive Cryogenic Target Physics," to be published in the proceedings of the 2nd International Conference on Inertial Fusion Sciences and Applications.

F.-Y. Tsai, E. L. Alfonso, S. H. Chen, D. R. Harding, and T. N. Blanton, "Effects of Processing Conditions on the Quality and Properties of Vapor-Deposited Polyimide Shells," to be published in Fusion Science and Technology.

A. Verevkin, J. Zhang, R. Sobolewski, A. Lipatov, O. Okunev, G. Chulkova, A. Korneev, K. Smirnov, and G. N. Gol'tsman, "Detection Efficiency of Large-Active-Area NbN Single-Photon Superconducting Detectors in the Ultraviolet in Near-Infrared Range," to be published in Applied Physics Letters.

L. J. Waxer, J. H. Kelly, J. Rothenberg, A. Babushkin, C. Bibeau, A. Bayramian, and S. Payne, "Precision Spectral Sculpting for Narrowband Amplification of Broadband FM Pulses," to be published in Optics Letters.

B. Yaakobi, F. J. Marshall, T. R. Boehly, R. P. J. Town, and D. D. Meyerhofer, "EXAFS Experiments Using a Laser-Imploded Target as a Radiation Source," to be published in the Journal of the Optical Society of America B.

J. D. Zuegel and S. A. Letzring, "Bulk Microwave Phase Modulators for Smoothing by Spectral Dispersion," to be published in Applied Optics.

Conference Presentations

D. D. Meyerhofer, B. Yaakobi, T. R. Boehly, F. J. Marshall, and R. P. J. Town, "EXAFS Detection of Heating of Metals by Shocks and Radiation," JOWOG 37, Lawrence Livermore National Laboratory, 28 January–1 February 2002.

A. V. Okishev, D. Battaglia, I. Begishev, and J. D. Zuegel, "Highly Stable, Diode-Pumped, Cavity-Dumped Nd:YLF Regenerative Amplifier for the OMEGA Laser Fusion Facility," OSA Advanced Solid-State Lasers, Quebec City, Canada, 3–6 February 2002.

W. Seka, "Laser–Plasma Interaction Studies on OMEGA Relevant to Direct-Drive NIF Ignition Targets," LULI Seminar, St. Lary, France, 4 March 2002.

W. T. Shmayda and R. D. Gallagher, "Recovery of Tritium from Pharmaceutical Mixed Waste Liquids and Solid Absorbents," 4th International Conference on Isotopes, Cape Town, South Africa, 10–14 March 2002.